THE UNIVERSITY OF CHICAGO

INTERACTIONS AND EXCITATIONS IN QUANTUM DEGENERATE ^{133}CS-^{6}LI BOSE-FERMI MIXTURES

A DISSERTATION SUBMITTED TO
THE FACULTY OF THE DIVISION OF THE PHYSICAL SCIENCES
IN CANDIDACY FOR THE DEGREE OF
DOCTOR OF PHILOSOPHY

DEPARTMENT OF PHYSICS

BY
KRUTIK PATEL

CHICAGO, ILLINOIS
DECEMBER 2022

To my loving family, wonderful friends, and amazing girlfriend.

“Quiet dignity? Have you met us?” - Louise Belcher

TABLE OF CONTENTS

LIST OF FIGURES

ACKNOWLEDGMENTS

I'd first like to thank my advisor Prof. Cheng Chin who gave me the amazing opportunity to work in his lab and benefit from his immense experience. I have learned so much from him about not only about physics but also how to be a better experimentalist and scientist. He is always quick to give advice and somehow manages to be generous with the remarkably little extra time he can find on any given day. It is easy to see that he genuinely cares very much about his students and their development and I sincerely appreciate his mentorship.

I would like to thank various members of the Li-Cs lab, starting with Jacob Johansen and Brian DeSalvo, who were working on Li-Cs when I joined. Jacob brought me up to speed on Li-Cs while we were sitting in lab during the data-taking phase of the Efimov Universality paper. Brian served as my mentor for several years after Jacob left, and he taught me so much that it felt like I was in the lucky position of having two advisors. He has a nearly supernatural sense for locating hardware issues in the maze of equipment in Li-Cs and he was a blast to work with so closely.

I'd like to thank Geyue (Frank) Cai, who I have worked with closely for the majority of my PhD, for his friendship and solidarity during the many hours we have spent together in lab. He is at least 5x better at math than me, and has much steadier hands. I also really enjoyed the discussions outside of science, as he is someone with a very different perspective than my own on things cultural and political. I'd also like to thank the undergrads who have worked in Li-Cs over the years: Allen, who helped us with the initial microscope bench tests, Xinyu, who helped develop numerical simulations, and Nick, who helped run simulations for the sound paper. Also, Bertrand, who joined us only for a small time during the pandemic and helped us investigate some of the theory of Bose-Fermi mixtures. Thank you to our newest Li-Cs member Henry Ando, who was vital to preparing our recent sound propagation manuscript and is learning very fast.

Thank you to the members of Cs lab that I have overlapped with, from Lei Feng and

Logan Clark to Kaixuan (Kevin) Yao, Zhendong Zhang, and Shu Nagata. Lei gave me quite a few tips in lab when I was new, and he is hilarious. Logan guided me through my initial 335 project in the lab, and he is so happy and helpful and taught me how to actually set up optics on a breadboard. I'd like to thank Kevin and Zhendong for their good company, and their occasional sanity checks on my theoretical questions.

Next, I'd like to thank the QMS lab members. Thanks to Mickey McDonald, for his lovely musical performances and hosting of small singer-songwriter shows in his apartment. Thank you to Jon Trisnadi for being so helpful and allowing me to ask lots of silly experimental questions. His calm and laid back demeanor is an asset to the lab, and you can always count on him. Thank you to Jiamei Zhang for your help throughout the years and for taking over as Safety Officer.

I'd also like aknowledge the tsunami of young graduate students breathing new life into the Chin Lab, specifically Lauren Weiss, Aditi Goyal, Jay Jachinowski, and Evan Yamaguchi. I look forward to reading your future papers!

Thanks to Maria Jimenez, for all of her help with administrative issues and event planning. Thanks to Lilith Swygert and Kapila Navaratne for their help navigating University requirements regarding procurement of equipment that we often needed desperately. Thank you to Luigi Mazzenga for the great conversations, machine shop training, and freely given advice on how to actually machine things properly. I'd also like to thank John Phillips and his successor Bentley Wall for all they do, both behind the scenes and in our labs early in the morning, to help keep our experiments running. They have been so helpful throughout the years through building and climate issues that are so stressful.

Thank you to those who served on my committee: Kathy Levin, Philippe Guyot-Sionnest, Jon Simon, and Dave DeMille, for taking time out of their unbelievably busy schedules to help oversee my academic progress.

Outside of the University of Chicago, I'd like to thank my friends for being supportive and a ton of fun. Thanks to David Alspaugh, for the exchange of musical ideas and graduate school experiences. Thank you Kevin Crapo, for the late nights and tropical swims. Thank you to Zachary Hall, for being my best friend and unquestionable ride-or-die. Thank you to my family, for their unconditional love and support throughout graduate school and my life in general. Finally, thank you to my girlfriend of 11 (has it really been 11?) years, Brittany Edmunds, for everything.

ABSTRACT

The study of quantum many-body systems remains a topic at the forefront of both theoretical and experimental physics research. These systems can exhibit a wealth of interesting phenomena and phases, and their understanding is important for progress towards new quantum technologies. Ultracold atomic gases are a powerful experimental platform for studying quantum many-body physics due to the flexibility and control that they afford.

From the perspective of quantum simulation, mixtures of bosonic and fermionic neutral atoms offer a unique experimental system which permits tunable interactions between both types of fundamental particles. In solid-state materials, the interplay between the bosonic and fermionic components can be very important, with the most famous example being phonon-induced electron pairing in conventional superconductors.

This thesis describes experiments on quantum degenerate mixtures of bosonic ^{133}Cs and fermionic ^{6}Li with tunable interspecies interactions. We have created the first degenerate mixtures of Li and Cs atoms and performed several experiments studying the role of interactions in their ground state and dynamics. The central question investigated is this: "What happens to a Bose-Einstein condensate when it is immersed in a degenerate Fermi gas?" Throughout the work presented in this thesis, we have discovered several answers: the fermionic environment changes the effective confinement, the effective 2- and 3- body interactions, the phase diagram, and the excitations of the condensate.

Our work represents significant progress in understanding the quantum behavior of Bose-Fermi mixtures, establishing the Li-Cs system as a valuable experimental platform in this direction. We lay groundwork for future studies of strongly interacting bosons and fermions, for which there are numerous fascinating theoretical proposals suggesting new quantum phases and phenomena.

CHAPTER 1

INTRODUCTION

1.1 Ultracold Gases and Quantum Simulation

There are two types of particles, those with integer spin (bosons) and half-integer spin (fermions). The fundamental particles that make up matter, such as protons, neutrons, and electrons, are all fermions. Fundamental force carriers, such as photons, gluons, and pions are bosons. Composite objects, such as atoms, which are made out of fundamental fermions, can end up as either bosonic or fermionic due to the addition of the spin of their constituents. In this way, the quantum statistics of a neutral atom are determined by its neutron number, and different isotopes of the same atom can be bosonic or fermionic.

The fundamental difference between these types of particles is the way that they behave under particle exchange. The wave function of bosons must always be symmetric with respect to particle exchange, while for fermions it must be antisymmetric. This rule, obtained from the spin-statistics theorem of relativistic quantum theory, dictates an enormous amount of physical phenomena, and is even explicit in many technological applications familiar to the reader's personal experience. For example, lasing is an effect driven by boson statistics, and semiconductor technology is fundamentally based on the fermion statistics of electrons.

In the context of ultracold atomic physics, both bosons and fermions have been used extensively for various scientific applications. These quantum gases provide a valuable experimental platform due to the level of control they offer through the generation of optical potentials and interaction tuning (see Section 2.1). They are well isolated from their environment and can be created with very few defects compared to their solid state counterparts. They operate on length and time scales that are amenable to optical microscopy and straightforward electronics. Their rich internal structure and long-lived internal states are also valuable tools for obtaining experimental information with very high precision.

Ultracold bosonic atoms were the first to be used for quantum many-body physics, initially igniting the field of quantum gases with the observation of Bose-Einstein condensation in ^{87}Rb by E. A. Cornell's group in 1995 [1], which was awarded the Nobel Prize in Physics in 2001 (along with C. Wieman and W. Ketterle). These types of systems were initially used to study the basic theories of weakly interacting bosons, as they were the first alternative to liquid He, a system which remains a theoretical challenge to this day. Soon afterwards, the study of atoms in optical lattices formed by the interference of laser beams became a major focus in the ultracold gas community, permitting the study of analog materials to aid condensed matter physics in the study of strongly correlated materials. Ultracold bosons in optical lattices have been used for an enormous number exciting experimental studies, such as the the superfluid-Mott insulator transition, scaling near quantum critical points, supersolids, time crystals, and many more (for reviews see Refs. [2–4]).

Meanwhile, a significant goal for the field of quantum gases became the study of fermionic atoms in optical lattices, since these systems are a more faithful analog of electrons in solid-state materials. The first degenerate atomic Fermi gases were experimentally created in 1999 by B. DeMarco and D. Jin in Colorado [5]. Soon after, fermionic pairing was observed in R. Grimm's [6] and D. Jin's lab [7]. Bardeen-Cooper-Schrieffer (BCS) superfluidity was demonstrated through quantized vortices in the Ketterle group the following year [8]. Since then, studies of the famous BEC-BCS crossover have been a major topic of scientific interest. Another major direction is the study of the Fermi-Hubbard model (see Ref. [9] for a review), often nowadays in quantum gas microscopes, which intend to shed light on basic features of high temperature superconductivity.

1.2 Bose-Fermi Mixtures

Combinations of bosonic and fermionic gases are considerably less well-studied than each individually. The first quantum degenerate gas Bose-Fermi (BF) mixtures were made in

2001 out of different isotopes of Li, specifically ^{6}Li/^{7}Li at LKB [10] and Rice University [11]. In the next year, the first heteronuclear mixtures were made, using fermionic ^{40}K/ bosonic ^{87}Rb at LENS [12] and JILA, and fermionic ^{6}Li / bosonic ^{23}Na at MIT [13]. A thorough overview of which groups have successfully cooled various combinations of bosons and fermions to degeneracy since those first experiments can be found in Table 1 of Ref. [14].

Generally speaking, multi-species experiments are harder to work with than single species experiments, but offer a variety of new experimental opportunities for the trouble. Below, we will briefly describe some of the research directions being pursued by groups around the world with Bose-Fermi mixtures.

- *Bose-Fermi mixtures in optical lattices.* A few years after the initial heteronuclear mixtures, several groups began to experimentally study the behavior of Bose-Fermi mixtures in optical lattices. They have observed localization of bosons as a consequence of fermionic atoms [15, 16], interspecies interaction corrections to the Superfluid-Mott Insulator transition [17], and realized interacting Mott insulators of each type [18]. Much of the initial interest revolved around sympathetic cooling of fermions, but there are still many untested theoretical proposals concerning BF mixtures in lattices.

- *Heteronuclear molecules.* There is enormous interest in the study of ultracold molecules for many applications [19, 20], including precision tests of fundamental physics, quantum computation, ultracold chemistry, and many-body physics with long-ranged interactions. One important feature is their rich internal structure, which can offer particularly useful states for precision measurement and quantum computation. Another is that heteronuclear molecules can exhibit large dipole moments that are absent in homonuclear molecules by symmetry, which makes them useful for many-body physics with long-ranged interactions. If the two components of the heteronuclear molecule are of different quantum statistics, then the result is a rich system of fermions with long-ranged interactions. The Weidemueller group has measured the dipole moment of deeply bound Li-Cs molecules [21] and obtained a large value of > 5 Debye. These molecules are currently being pursued for quantum science in optical tweezers at Purdue University by J. Hood.

- *Polarons.* Polarons are impurities which are dressed by their medium. Due to the tunability of interactions in ultracold atomic gases, they have been used to perform many interesting experiments in both Fermi and Bose polaron systems (the objects are labelled by the medium). In the impurity limit, the statistics of the impurities do not matter, but Bose-Fermi (BF) mixture systems have nonetheless proved useful due to their particular interaction spectra [22–27]. In recent times, the full crossover from Fermi to Bose polarons has been studied in the group of R. Grimm [28], which is an experiment that leverages the flexibility of ultracold Bose-Fermi mixtures in a very striking way. There are also interesting connections between polarons and three-body physics, see Section 7.2.

- *Superfluid mixtures.* One of the most recent developments in this field has been the creation of BCS-BEC superfluid mixtures, which have been reported in several groups around the world. There have been reports of such systems created in ^{6}Li/^{7}Li [29], ^{174}Yb/^{6}Li [30], and ^{41}K/^{6}Li.[31]. This is a rare type of quantum system, which may be promising for a number of theoretical proposals. It may be possible to create Li-Cs BCS-BEC mixtures as well, see Section 7.5.

1.3 Mediated Interactions

The fundamental particles of nature interact via forces, and those interactions are said to be mediated by gauge bosons. For example, the electromagnetic force is mediated by photons, and the weak force is mediated by W and Z bosons. Consider the classic example of Møller scattering, depicted in Fig. 1.1. This is the simplest example of a process where

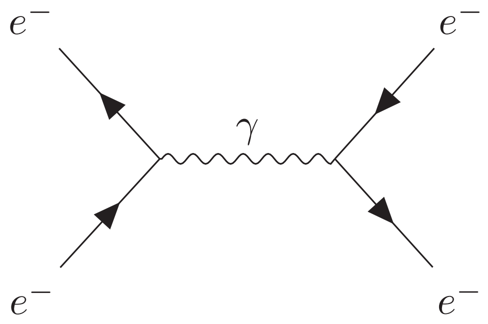

Figure 1.1: Møller scattering. Shown is the (s-channel) diagram for Møller scattering, in which two electrons scatter off each other, exchanging a photon. The interaction is said to mediated by photons, and the process is second order in the coupling constant between photons and electrons, which is the fine structure constant α.

the electromagnetic force is said to be mediated by a photon. The photon is a necessary ingredient when evaluating the matrix elements and cross-section for this process.

The idea of mediated interactions, however, is much broader than this fundamental context. There are a wide variety of systems which exhibit such interactions in materials and even in Atomic/Molecular/Optical (AMO) physics at different levels. In the context of materials, a very famous example is conventional (BCS) superconductivity, which is observed at low single-Kelvin temperatures in many metals such as, for example, tin and indium. There is also the Ruderman-Kittel-Kasuya-Yosida (RKKY) interaction, which is closely related to much of the science in this thesis and is mediated by fermions within a material. The most studied example in AMO physics is the mediation of interactions by photons populating an optical cavity [32, 33].

From the perspective of quantum science and simulation using neutral atoms, mediated interactions add a level of complexity and control that can support novel quantum phases and enable new types of Hamiltonian engineering. A major reason for this is that in typical ultracold atomic gases, scattering can be treated as a contact interaction (see Section 2.1). This simplification is a double-edged sword: it can permit more successful theoretical predictions, but also limits the ability to realize a variety of quantum systems that involve long-ranged interactions.

There are a number of ways to engineer long-ranged potentials in ultracold gases; popular choices include the use of molecules with dipole moments, Rydberg atoms, optical cavities, and permanently magnetic atoms. The type of fermion-mediated interactions discussed in this thesis are theoretically predicted to be long-ranged as well. They are weaker in strength but many-body in origin. This makes them, in the opinion of the author, a ripe topic for study, both in terms of fundamental science and quantum simulation.

1.4 Overview of the Thesis

The thesis is organized as follows:

- Chapter 2 presents a theoretical introduction that broadly covers the necessary knowledge to understand the work in this thesis. It is aimed to provide a sufficient primer for a graduate student.

- Chapter 3 presents an overview of the experimental apparatus. More complete descriptions of most aspects are found in Ref. [34], however the recently added high resolution imaging set up is discussed in more detail.

- Chapter 4 discusses our creation of the first degenerate Li-Cs mixtures and initial scientific studies. In this chapter, we confirm degeneracy and create degenerate Fermi gases entirely trapped by a BEC through interactions. By studying these trapped Fermi gases, we gain insight into the processes which prevent the onset of mechanical instability in our mixture at strong interspecies attraction. It is reproduced from Ref. [35].

- Chapter 5 discusses our observation of fermion-mediated interactions between bosonic atoms. We experimentally study the dipole mode of condensates immersed in a Fermi gas, quantify the effect of fermion-mediated interactions based off the size of the BEC, and observe Bose-Fermi solitons in the quasi-1D regime. This chapter is reproduced from Ref. [36].

- Chapter 6 discusses our most recent work studying excitations of the condensate in our mixtures. We perform the first direct measurements of sound propagation, and extract information about effective 3-body boson-boson interactions and the critical scattering length for collapse. Intriguingly, we also observe stable sound propagation at resonant interspecies interactions. This chapter is reproduced from work which is currently under submission.
- Chapter 7 discusses some ideas and future experiments that are of interest in our lab, hopefully giving a sense of interesting work that lies just on the horizon.

CHAPTER 2

THEORETICAL BACKGROUND

In this chapter, we will briefly discuss the theoretical background necessary to make sense of the work in this thesis. It will not be a very deep dive, and the reader is encouraged to pursue further reading in the references. It will, however, be presented in a simple way that will hopefully help newer graduate students get their bearings. Much of the first few sections follow portions of Refs. [37–41].

2.1 Ultracold Interactions

In this section, we will present a simple summary of ultracold atomic scattering and the concept of Feshbach resonances, which allow the tuning of interactions between atoms using an external magnetic field. This will provide a framework to understand the interactions that are important in all of the experiments presented in this thesis.

The approach to describe ultracold two-body scattering is to solve the quantum mechanical scattering problem at long wavelengths. We consider the Hamiltonian for the relative motion of two particles

$$H = \frac{\hbar^2 k^2}{2m_r} + V(r), \tag{2.1}$$

where $\hbar$ is the reduced Planck's constant, r is the relative position of the two atoms, k is the relative momentum, and m_r is the reduced mass. We consider scattering solutions of the form

$$\psi = e^{ikz} + f(\theta)\frac{e^{ikr}}{r}, \tag{2.2}$$

where z is taken as the arbitrary direction of the incoming wave and the second term is the outgoing scattered wave. The outgoing wave can rewritten in terms of its angular momentum components according to a partial wave decomposition using the spherical harmonics. At large separation, each component is characterized by a phase shift. For potentials $V(r)$ that fall off sufficiently quickly with distance, at very low energies ($k \rightarrow 0$) the contributions for components with angular momentum $l > 0$ vanish, leaving only an s-wave contribution. The typical Van der Waals potential (approximated $V_{vdw}(r) = \frac{C_{12}}{r^{12}} - \frac{C_6}{r^6}$) between neutral atoms satisfies this criterion. At very low energies, the wavefunction approaches $\psi = 1 - \frac{a}{r}$, which defines the scattering length a. For positive a, the extrapolated wave function to small separations is pushed out of the scattering region, and for negative a it is pulled in. These two cases correspond to effective repulsion or attraction, respectively.

If all of these simplifications hold, then the scattering potential can be replaced with simpler pseudopotential which reproduces the scattering length a, given by

$$V = \frac{2\pi\hbar^2 a}{m_r}\delta(r) \equiv g\delta(r), \tag{2.3}$$

where the reduced mass $m_r = \frac{m}{2}$ for intraspecies scattering, $\delta(r)$ is the Dirac delta function, and g is the coupling strength for scattering between the atoms.

For distinguishable particles, the resulting scattering cross-section corresponds to only the s-wave cross section $\sigma = 4\pi a^2$. Due to symmetrization requirements, in the case of identical bosons the cross section is doubled to $8\pi a^2$ and for identical fermions it vanishes. This is a striking consequence of quantum scattering theory, which states that fermions in the same internal state do not interact in the s-wave channel. The lowest partial wave that can contribute is the p-wave channel, which is extremely suppressed at the typical energy scale for degeneracy in these systems.

One of the major advantages of cold atoms as an experimental platform is the tunability of the interactions between atoms using Feshbach resonances [42]. For multi-level atoms, scattering can take place in different "channels," which are sets of incoming and outgoing states. If different internal states have different magnetic moments, then their relative energy

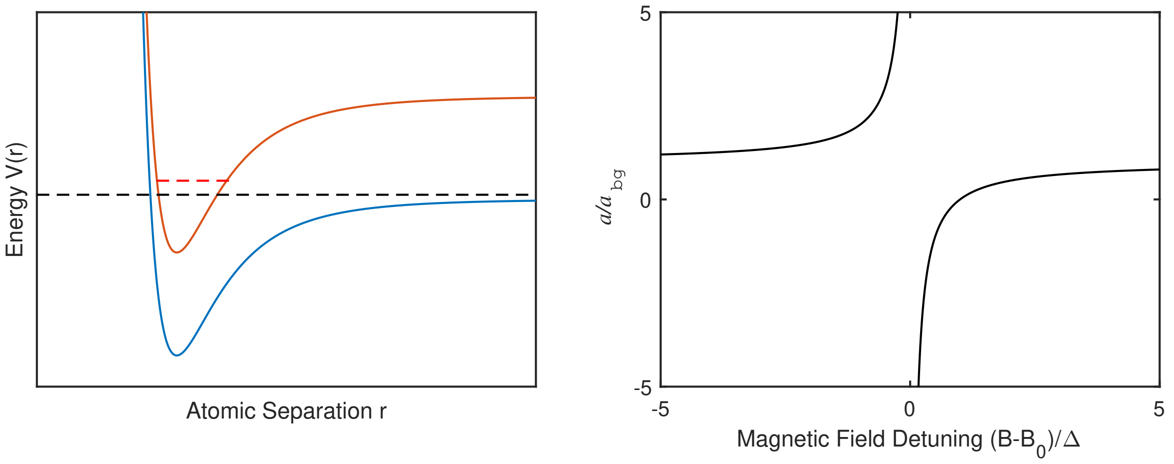

Figure 2.1: Schematic of a Feshbach resonance. Left panel: Two scattering channels are shown, the "open" channel (blue solid line) and the "closed" channel (red solid line). The collision energy of two atoms in the open channel (black dashed line) is near the energy of a bound state in the closed chanel (red dashed line). In general, each potential has many bound states and there are many channels, but this is a simplified schematic illustrating one resonance. Right panel: Scattering length near a Feshbach resonance at magnetic field B_0. At positive scattering lengths, the bound state is accessible to the atom pair.

can be tuned using a magnetic field, allowing control over the sign and strength of the atomic interactions. This is referred to as a magnetically tunable Feshbach resonance.

For a schematic of how Feshbach resonances work, refer to Fig. 2.1. When the energy of a bound state in a "closed" channel (not energetically permitted) becomes equal to the collision energy, a scattering resonance can occur, called a Feshbach resonance. The scattering length diverges in a characteristic way near the resonance

$$a = a_{\rm bg}\left(1 - \frac{\Delta}{B - B_0}\right), \tag{2.4}$$

where $a_{\rm bg}$ is the background scattering length, Δ is the change in field between the resonance and zero crossing, and B_0 is the pole of the resonance. This interaction tuning is one of the most important features of ultracold atom systems. In addition to the control over the atomic interactions, they can be used to create molecules.

2.2 Bose-Einstein Condensates

Condensation

A system of non-interacting bosons in 3D undergoes a phase transition (condensation) at sufficiently low temperatures. This phase transition is characterized by macroscopic occupation of the ground state due to Bose statistics. We will not discuss this process in great detail, we refer the reader to textbooks such as Refs. [37, 43]. Consider a system of bosons in the grand canonical ensemble. The expected occupation of state i is given by

$$\langle n_i \rangle = \frac{1}{e^{\beta(\epsilon_i - \mu)} - 1} \tag{2.5}$$

where $\beta = \frac{1}{k_B T}$ with k_B the Boltzmann constant and T the temperature, ϵ_i is the energy of state i and μ is the chemical potential. At a critical temperature T_c, the fraction of the sample in the ground state begins to grow as $1 - (T_c/T)^\alpha$, where $\alpha = 3/2$ for uniform gases and $\alpha = 3$ for harmonically trapped gases. In the latter case, the transition temperature for a non-interacting gas is given by $k_B T_C \approx 0.94 \hbar \bar{\omega} N^{1/3}$ where $\bar{\omega} = (\omega_x \omega_y \omega_z)^{1/3}$, N is the total particle number and ω_i are the trap frequencies in each direction. Practically, it is nearly impossible to bring a sample to sufficiently low temperatures without permitting it to thermalize during cooling, which requires atomic interactions. The presence of interactions complicates the picture of condensation, but the process still takes place at a modified critical temperature.

Gross-Pitaevskii Equation

For a BEC with typical Van der Waals interactions it is appropriate to write the Hamiltonian [37]:

$$H = \sum_{i=1}^{N} \left[\frac{p_i^2}{2m} + V(r_i) \right] + g_{\mathrm{BB}} \sum_{i<j} \delta(r_i - r_j) \tag{2.6}$$

where p_i is the momentum of particle i, $V(r)$ is the external potential, and g_{BB} is the coupling constant discussed in the previous section. This Hamiltonian sums the kinetic and potential energy of each particle, then add an pair-wise contact interaction with strength g_{BB} without double-counting.

For a product state of the form

$$\Psi(r_1, r_2, ..., r_N) = \prod_{i=1}^{N} \phi(r_i), \tag{2.7}$$

where ϕ is the single particle wave function, the energy is given by

$$E = N \int dr \left[\frac{\hbar^2}{2m_B} |\nabla \phi(r)|^2 + V(r)|\phi(r)|^2 + \frac{N-1}{2} g_{\mathrm{BB}} |\phi(r)|^4 \right]. \tag{2.8}$$

The interaction energy is then $N^2/2$ times the interaction energy for a pair of particles for sizeable particle numbers. The condensate wave function, $\psi(r) \equiv \sqrt{N}\phi(r)$ is the single particle wave function normalized to return the total particle number instead of unit probability, so that $n(r) = |\psi(r)|^2$. For non-interacting gases ($g_{\mathrm{BB}} = 0$), this would correspond to the the ground state of the external confinement $V(r)$. Inserting this condensate wave function $\psi(r)$ into the energy and minimizing it with respect to independent variations gives the celebrated (time-independent) Gross-Pitaevskii equation (GPE)

$$\frac{-\hbar^2}{2m_B} \nabla^2 \psi(r) + V(r)\psi(r) + g_{\mathrm{BB}} |\psi(r)|^2 \psi(r) = \mu \psi(r) \tag{2.9}$$

In many cases, the kinetic energy term in the GPE can be ignored for calculating the ground state because the interaction term dominates over the kinetic energy. This approximation is referred to as the Thomas-Fermi (TF) approximation. For the typical case of harmonic confinement $V(r) = \sum_i^3 \frac{1}{2} m \omega_i^2 x_i^2$, the resulting TF ground state density profile is parabolic, giving the 3-D condensate density n_0 as

$$n_0 = \frac{\mu}{g_{\mathrm{BB}}} \left[1 - \sum_i \left(\frac{x_i^2}{R_i^2} \right)^2 \right], \tag{2.10}$$

where the R_i are the i-direction Thomas-Fermi radii of the condensate. These are given in terms of the boson-boson scattering length a_{BB} and trapping frequencies ω_i as

$$R_i = \sqrt{\frac{2\mu}{m\omega_i^2}} = a_{\mathrm{ho}} \left(\frac{15 N_B a_{\mathrm{BB}}}{a_{\mathrm{ho}}} \right)^{1/5} \tag{2.11}$$

where $a_{ho} = \sqrt{\frac{\hbar}{m\bar{\omega}}}$ is the oscillator length for the geometric mean of the trap frequencies $\bar{\omega} = (\omega_x \omega_y \omega_z)^{1/3}$. The chemical potential is fixed by the particle number $N = \int d^3r \, n_0(r)$ as $\mu = \frac{\hbar\bar{\omega}}{2} \left(\frac{15 N_B a_{\mathrm{BB}}}{a_{\mathrm{ho}}} \right)^{2/5}$.

Outside of the TF approximation, for more accurate density profiles and to include dynamics, it is necessary to take into account the kinetic energy. There are few analytical results for full solutions, see Appendix C for discussions of simple numerical methods.

The GPE is a very effective tool to simulate trapped Bose-Einstein condensates, and has been shown to be very useful for a wide variety of experiments. It does not always work, however, as it assumes that all particles are in the ground state. At strong interactions, the fraction which does not remain in the condensate (quantum depletion) can be large. Additionally, atoms can be excited out of the condensate, for example by time-dependent drives. For long-ranged interactions, the GPE in this form is no longer appropriate, although it can be approximated (see Section C). Despite its limitations, it is invaluable to experimentalists working with condensed systems.

Bogoliubov treatment

The Hamiltonian can be re-written in terms of the annihilation and creation operators $\hat{\psi}$ and $\hat{\psi}^\dagger$ for bosons as

$$\hat{H} = \int dr \left[-\hat{\psi}^{\dagger}(r)\frac{\hbar^2}{2m_B}\nabla^2\hat{\psi}(r) + V(r)\hat{\psi}^{\dagger}(r)\hat{\psi}(r) + \frac{g_{BB}}{2}\hat{\psi}^{\dagger}(r)\hat{\psi}^{\dagger}(r)\hat{\psi}(r)\hat{\psi}(r) \right]. \tag{2.12}$$

For a homogenous gas, the position space operators can be written in momentum space as:

$$\begin{aligned} a_p &= \frac{1}{\sqrt{V}}\int dre^{-ipr/\hbar}\hat{\psi}(r) \\ a_p^{\dagger} &= \frac{1}{\sqrt{V}}\int dre^{ipr/\hbar}\hat{\psi}^{\dagger}(r) \end{aligned} \tag{2.13}$$

where V is the system volume and p is the momentum $\hbar k$. They are the Fourier transform of the position space operators. Then the Hamiltonian can be rewritten in terms of these operators as

$$H = \sum_p \epsilon_p^0 \hat{a}_p^{\dagger}\hat{a}_p + \frac{g_{BB}}{2V}\sum_{p,p',q}\hat{a}_{p+q}^{\dagger}\hat{a}_{p'-q}^{\dagger}\hat{a}_{p'}\hat{a}_p, \tag{2.14}$$

where $\epsilon_p^0 = \frac{\hbar^2 k^2}{2m_B}$ is the bare kinetic energy of a boson. In the Bogoliubov treatment, one replaces the operators $\hat{a}_0$ and $\hat{a}_0^{\dagger}$ with $\sqrt{N_0}$, since for large particle numbers $N \approx N+1 \approx N-1$. Rather than ignoring quantum fluctuations, as in the GPE approach which yields a classical field theory, they are only taken to be small. So, we keep only the largest orders which allows the Hamiltonian to be approximated as

$$\hat{H} \approx \frac{N_0^2 g_{\mathrm{BB}}}{2V} + \sum_{p\neq 0}(\epsilon_p^0 + 2n_0 g_{\mathrm{BB}})\hat{a}_p^{\dagger}\hat{a}_p + \frac{n_0 g_{BB}}{2}\sum_{p\neq 0}(\hat{a}_p^{\dagger}\hat{a}_{-p}^{\dagger} + \hat{a}_p\hat{a}_{-p}). \tag{2.15}$$

This Hamiltonian can be written in terms of the new annihilation and creation operators of non-interacting elementary excitations, rather than the bosonic atoms themselves. The Hamiltonian becomes

$$H = \frac{N^2 g_{\mathrm{BB}}}{2V} + \sum_{p\neq 0} \epsilon_p \hat{\alpha}_p^\dagger \alpha_p - \frac{1}{2}\sum_{p\neq 0}(\epsilon_p^0 + n_0 g_{\mathrm{BB}} - \epsilon_p). \tag{2.16}$$

The annihilation and creation operators α_k and $\alpha_k^\dagger$ for the phonons are related to the corresponding operators for the bosonic atoms a_k and $a_k^\dagger$ through the Bogoliubov transformation

$$\begin{aligned} a_k &= u_k \alpha_k + v_k \alpha_{-k}^\dagger \\ a_k^\dagger &= u_k \alpha_k^\dagger + v_k \alpha_{-k}, \end{aligned} \tag{2.17}$$

with coefficients defined by

$$\begin{aligned} u_k^2 &= \frac{1}{2}\left(\frac{\epsilon_k^{\mathrm{B}} + g_{\mathrm{BB}} n_{\mathrm{B}}}{\hbar\omega_k} + 1\right) \\ v_k^2 &= \frac{1}{2}\left(\frac{\epsilon_k^{\mathrm{B}} + g_{\mathrm{BB}} n_{\mathrm{B}}}{\hbar\omega_k} - 1\right), \end{aligned} \tag{2.18}$$

where $\hbar\omega_k = \sqrt{\left(\epsilon_k^{\mathrm{B}}\right)^2 + 2 g_{\mathrm{BB}} n_{\mathrm{B}} \epsilon_k^{\mathrm{B}}}$ is the Bogliubov dispersion and $\epsilon_k^{\mathrm{B}} = \frac{\hbar^2 k^2}{2 m_{\mathrm{B}}}$ is the kinetic energy of a boson.

The third term in the transformed Hamiltonian gives the Lee-Huang-Yang (LHY) correction to the ground state energy, which is typically weak. However, LHY corrections have certainly been measured, and in some cases can be fundamentally important to the behavior of the system, for example in the case of Bose-Bose liquid droplets [44, 45].

2.3 Single Component Degenerate Fermi Gases

Degenerate Fermi gases are very different from Bose-Einstein condensates. In this section, we will discuss the behavior of single-component zero temperature Fermi gases which to very good approximation do not interact at ultracold temperatures, as discussed in Section 2.1.

The particles in a degenerate Fermi gas follow Fermi-Dirac statistics, in which the occupation of state i is given by:

$$< n_i >= \frac{1}{e^{\beta(\epsilon_i - \mu)} + 1} \tag{2.19}$$

with a very important change in sign in the denominator compared to the case of Bose statistics discussed in the previous section. This sign change is a result of enforcing the Pauli exclusion principle, and permits only one fermion per state. At zero temperature, a single component degenerate Fermi gas will not macroscopically occupy the ground state or undergo a phase transition, but will instead form a so-called "Fermi sea," in which each state is filled by one fermion up to the zero-temperature chemical potential, called the Fermi energy E_F.

In a harmonic trap, the particles thus occupy trap levels up to the energy E_F. It is then possible to calculate the density profile by summing up the appropriate number of harmonic oscillator wave functions. The resulting density profile will not be "smooth," but will rather have small, Fermi energy scale ripples due to the eigenfunctions, which will lose contrast as the particle number becomes large.

For large particle numbers and low momenta $k \ll k_F$ where $\frac{\hbar^2 k_F}{2m_F} = E_F$ defines the Fermi momentum k_F for fermions of mass m_F, instead of using the eigenfunctions one can employ the Thomas-Fermi approximation. Here, one treats the system semiclassically under a local density approximation. Specifically, the system is taken to locally behave according to the results of the uniform Fermi gas with a local Fermi $E_F - V_F$, where V_F is the external potential. For a uniform Fermi gas, the density is related to the Fermi energy as $E_F = \frac{\hbar}{2m_F}(6\pi^2 n_F)^{2/3}$. In the Thomas-Fermi approximation for fermions of mass m_F, we relate the Fermi energy to the local fermion density n_F and external potential V_F as

$$E_F = \frac{\hbar}{2m_F}(6\pi^2 n_F)^{2/3} + V_F, \tag{2.20}$$

where the Fermi energy is fixed by the normalization. In this picture, the extent of the gas is set by the Thomas-Fermi radii R_i defined by $E_F = \frac{1}{2}m\omega_i^2 R_i^2$. The resulting 3-D fermion density n_F is

$$n_F = N\frac{8}{\pi^2}\frac{1}{R_x R_y R_z}\left(1 - \sum_i \frac{x_i^2}{R_i^2}\right)^{3/2} . \tag{2.21}$$

This density distribution is useful for modelling low temperature systems, but it clearly does not contain many important details. In particular, the density ripples that this smooth profile are missing are the origin of the characteristic potential form for interactions mediated by the Fermi gas (see Section 2.5.)

2.4 Thermometry

The most straightforward method of thermometry for these atomic gas samples is time-of-flight imaging. The atoms are released from their optical confinement and allowed to freely evolve, ballistically expanding outward as they fall under the influence of gravity. The expansion is due to the kinetic energy of the atoms in the gas, and therefore can be used to measure the temperature. For free time-of-flight expansion times which are long compared to the trap period, the position distribution maps onto the momentum distribution.

Thermometry of Bose-Einstein condensates is relatively straightforward, because for temperatures below the T_c for condensation there is typically a thermal fraction which can be resolved in the absorption images. The condensate is only pure for zero temperature, and the macroscopic occupation of the ground state leads to a clear high density peak which distinguishes condensate atoms from thermal atoms.

Interactions between the condensate and surrounding atoms can lead to complications, but fitting the expansion of the thermal fraction works as a thermometer as long as it is resolvable in the imaging. Depending on the trapping geometry, directly fitting the thermal fraction in situ can be sufficient. The boson density n_B is bimodal below T_c and is a combination of two parts:

$$n_B = n_0 + n_{th} \tag{2.22}$$

where n_0 is the 3D condensate density and n_{th} is the thermal part. The thermal fraction profile can be fit to a Gaussian given by:

$$n_{th} = n_{p,th} \prod_i e^{\frac{-m\omega_i^2 x_i^2}{2k_B T}}, \tag{2.23}$$

where $n_{p,th}$ is the peak thermal density, T is the temperature, and ω_i are the trapping frequencies. Note that the actual profile of the thermal fraction is not quite Gaussian. At low temperatures, the distribution is modified by Bose statistics and is given in terms of a polylogarithm. However, since the temperature is determined from the extent of the thermal wings, rather than the overall shape of the distribution, this is not typically an important correction.

As discussed in Section 2.2, the 3D condensate density is a parabola. In an absorption image, the measured density is a 2D column density $n_{0,2}$ after integration in the third direction. Performing the integration results in the column density profile

$$n_{0,2} = \frac{4}{3}\frac{\mu}{g_{\mathrm{BB}}} R_z \left(1 - \frac{y^2}{R_y^2} - \frac{z^2}{R_z^2}\right)^{3/2}. \tag{2.24}$$

Often, we integrate again to perform a 1D bimodal fit, for example the x direction yields

$$n_{0,1x} = \frac{\pi}{2}\frac{\mu}{g_{\mathrm{BB}}} R_z R_y \left(1 - \frac{x^2}{R_x^2}\right)^2. \tag{2.25}$$

In the more specific case of our experiment, when performing time-of-flight measurements for the Cs atoms we first allow the gas to freely expand for a few ms while at high magnetic field, then switch off the field and allow further expansion. This is done to allow the density of the gas to reduce somewhat before dropping the field and causing the Cs atoms to travel

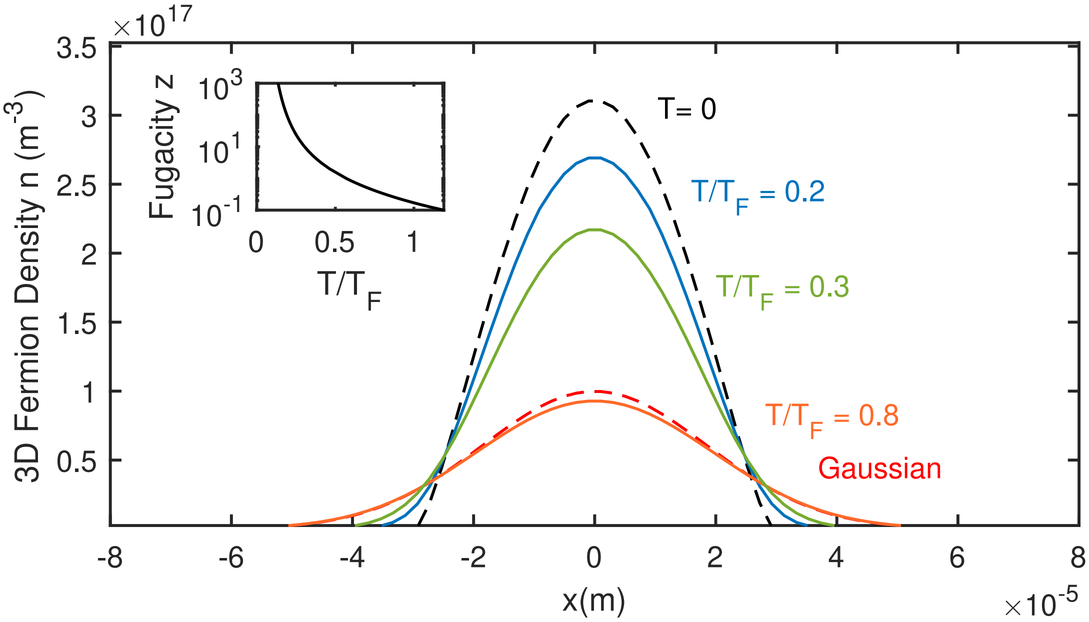

Figure 2.2: Effect of degeneracy on fermion density distribution. Inset: The fugacity z is a sharp function of T/T_F, and large values of the fugacity correspond to a higher degree of degeneracy and further departure from Gaussian density profiles. 3D density profiles are shown for a symmetric trap with $\omega/2\pi = 150$ Hz and 1×10^4 particles for different temperatures. The black dashed line is the $T = 0$ prediction (see text) and the red dashed line is a thermal prediction for $T = 0.8T_F$ for comparison. The various other curves are calculated for the labelled temperatures.

through many scattering resonances along the way which cause atom loss and heating. This process must be modelled for the thermal fraction to obtain accurate temperatures from the cloud size at a particular time of flight time.

For degenerate Fermi gases, however, performing thermometry is trickier. A single component Fermi gas does not undergo any phase transition as it reaches low temperatures, instead there is a smooth crossover. The overall kinetic energy in time-of-flight at zero temperature is set by the Fermi energy, so you cannot use the expansion rate alone to tell you the temperature as you approach the Fermi temperature T_F. Instead, the shape of the gas must be analyzed, and it is the departure from a thermal (Gaussian) profile which indicates degeneracy. A tell-tale sign that $T/T_F < 1$ is that the low momentum portion of the gas is lower than for a thermal gas, so fitting only the wings and comparing the result is a good qualitative indicator of degeneracy. We will discuss this in a bit more detail now, with much of the discussion following Refs. [46] and [38].

Thermometry of cold Fermi gases relies on the use of the polylogarithm function, which frequently appears in the statistical mechanics treatment of Bose and Fermi distributions. This function interpolates between the classical Gaussian profile and the zero-temperature Thomas-Fermi profile. The polylogarithm of order n is defined by the series

$$\mathrm{Li}_n(x) = \sum_k^{\infty} (-x)^k / k^n. \tag{2.26}$$

We measure the temperature by performing 2D fits to the column density of the Li. We use the Thomas-Fermi fit function

$$OD = A \frac{\mathrm{Li}_2 \left[-z e^{\frac{(x-x_0)^2}{2\sigma_x}} e^{\frac{(y-y_0)^2}{2\sigma_y}} \right]}{\mathrm{Li}_2 \left[-z \right]} + c \tag{2.27}$$

where A, x_0, y_0, σ_x, σ_y, c, and z are fit parameters representing an overall peak OD, the x center, the y center, the x and y widths, an offset caused by noise, and the fugacity, respectively. From the fugacity, the degeneracy parameter T/T_F is then obtained via

$$\frac{T}{T_F} = \left(\frac{-1}{6\mathrm{Li}_3(-z)} \right)^{1/3}. \tag{2.28}$$

This degeneracy parameter characterizes the discrepancy from a Gaussian thermal distribution, but does not itself tell the temperature of the sample. The 3D density n is calculated according to

$$n = \frac{-1}{\lambda_{dB}^3} \mathrm{Li}_{3/2} \left[-e^{\beta(\mu - V_F(r))} \right] \tag{2.29}$$

where $\lambda_{dB} = \sqrt{\frac{2\pi\hbar^2}{m_F k_B T}}$ is the thermal de Broglie wavelength. Sample calculated density profiles are shown in Fig. 2.2 that illustrate the crossover from Gaussian to Thomas-Fermi profiles as the temperature is lowered at constant particle number (fixed by μ).

The discrepancy from a Gaussian in experimental data can be seen qualitatively by fitting the wings or looking at the residuals of a full fit, which show clear structure at the center and edges that disappears when the profile is fit to a polylogarithm. The expansion of the widths σ_i, which grow as $\sigma_i = \left[\frac{k_b T}{m\omega_i^2}(1+(\omega_i t)^2)\right]^{1/2}$ for a gas released from harmonic confinement, is combined with the fugacity fit to obtain T and T_F.

2.5 Response Functions and Mediated Interactions

In a quantum degenerate Bose-Fermi mixture, the bosons are capable of mediating an interaction between the fermions and vice versa. The simplest picture for understanding this is to consider the system in terms of response functions. Atoms of the opposite species create perturbations as they move around in the gas, and other atoms feel those perturbations leading to an effective interaction. Since response functions have length scales set by the properties of the gas, they can be long-ranged, even though they originate from contact interactions defined by the scattering lengths involved.

First, let us discuss the case for impurities immersed in a BEC. The response function χ_B for a homogenous zero-temperature condensate is [37]:

$$\chi_B(q,\omega) = \frac{n_B q^2}{m_B(\omega^2 - \omega_q^2)} \tag{2.30}$$

where n_B is the boson density, q and ω are the momentum and frequency of the perturbation and ω_q is the Bogoliubov dispersion:

$$\hbar\omega_q = \sqrt{\left[\epsilon_q^0(\epsilon_q^0 + 2n_B g_{BB})\right]} \tag{2.31}$$

where $\epsilon_q^0 = \frac{\hbar^2 q^2}{2m_B}$ is the kinetic energy of a boson and $g_{BB} = \frac{4\pi\hbar^2 a_{BB}}{m_B}$ is the interaction strength between bosons. The response function χ_B features divergences for the condition

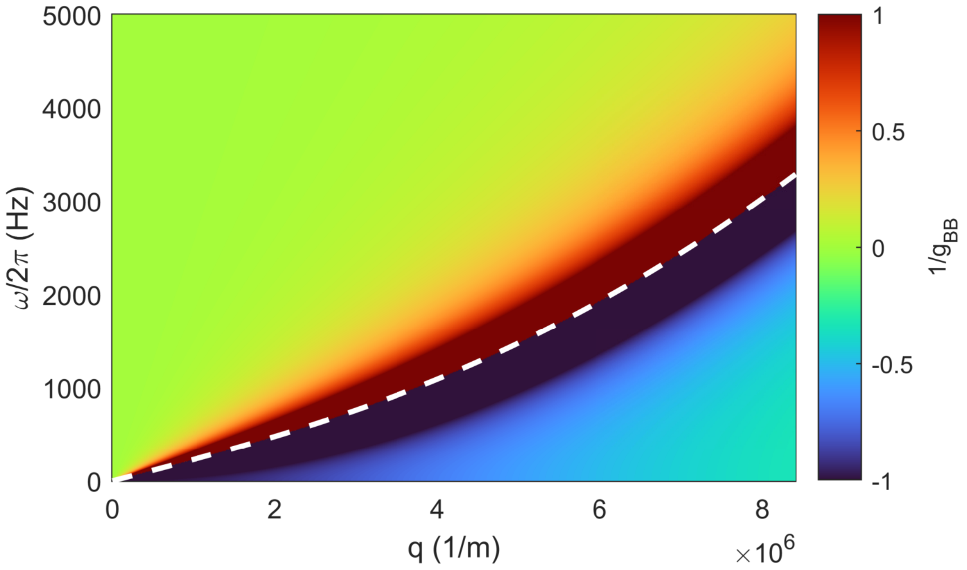

Figure 2.3: Density response function of a BEC. The dispersion and response function are shown for a BEC calculated from Eq. (2.30) for realistic experimental parameters and a scattering length $a_{BB} = 260a_0$. The white dashed line indicates the Bogoliubov dispersion. The colormap indicates the value of $\chi_B(q,\omega)$, which shows a dispersive lineshape about the divergence at the dispersion. The long wavelength, static limit gives $\chi_B(0,0) = -1/g_{BB}$.

$\omega = \omega_q$, which indicates that the system is resonantly excited if the excitation matches the dispersion, see Fig. 2.3. This is an intuitive result, and the unphysical divergence is a result of the omission of any damping mechanisms for the phonons in the simplest models of a BEC.

Let us consider now the static limit, where the impurities are stationary (or moving very slowly compared to the energy scale of the condensate.) Then,

$$\chi_B(q,\omega) \approx \chi_B(q,0) = \frac{n_B}{g_{BB}n_B + \hbar^2 q^2/4m_B}. \tag{2.32}$$

If we perform a Fourier transform, we see that this is a Yukawa potential (recall that $\int d^3k e^{ikr} \frac{1}{m^2+k^2} \propto e^{-kmr}/r$):

$$\chi_B(r,0) = \frac{-m_B n_B}{\pi\hbar^2}\frac{e^{-\sqrt{2}r/\xi}}{r} \tag{2.33}$$

where $\xi = \sqrt{\frac{\hbar^2}{2m_B n_B g_{BB}}}$ is the healing length of the condensate.

The mediated interaction, then, results from a coupling of density fluctuations. To see this, consider the following. A fluctuation in the impurity density δn_I leads to a potential felt by the bosons given by $\delta V_b = g_{BI}\delta n_I$, resulting in a density fluctuation $\delta n_b = \chi_b(q, w) g_{BI}\delta n_I$. Similarly, $\delta V_I = g_{BI}\delta n_I$ resulting in an effective second order energy shift in the impurities of $\delta V_I = g_{BI}^2 \chi_b \delta n_I$, defining the induced interaction $U_{ind} = g_{ba}^2 \chi_b$.

The range of the potential ξ is extended as the chemical potential $g_{BB}n_B$ is reduced, indicating that less massive atoms lead to longer range mediated interactions, similar to the case of fundamental particles. The boson-mediated interaction between fermions is closely analogous to BCS pairing in conventional superconductors, see Section 7.4 for further discussion.

The overall approach is similar for fermion mediated interactions, with the induced interaction between impurities now dictated by the fermion response function $\chi_F(q, w)$ instead. However, the calculation of the response function for the Fermi gas is is more complicated. This is not surprising, because the dynamics are not captured in something as straight forward as the Gross-Pitaevskii equation. This is ultimately a consequence of their much more complicated wave function.

Under the random phase approximation (RPA), the density response of a non-interacting Fermi gas is the so-called Lindhard function [47, 48]. For a 3-D system, the real part can be written

$$\mathrm{Re}[\chi_F(\bar{q}, \bar{\omega})] = \frac{k_F^3}{4\pi^2 E_F}\left[-1 + \frac{4\bar{q}^2 - \bar{q}_-^4}{8\bar{q}^3}\log\left|\frac{1 + \bar{q}_-^2/2\bar{q}}{1 - \bar{q}_-^2/2\bar{q}}\right| - \frac{4\bar{q}^2 - \bar{q}_+^4}{8\bar{q}^3}\log\left|\frac{1 + \bar{q}_+^2/2\bar{q}}{1 - \bar{q}_+^2/2\bar{q}}\right|\right] \tag{2.34}$$

where $\bar{\omega} = \frac{\hbar\omega}{E_F}$, $\bar{q} = q/k_F$, and $q_\pm^2 = \bar{\omega} \pm \bar{q}^2$. See Fig. 2.4. In the static limit, when $\omega \rightarrow 0$, the function reads

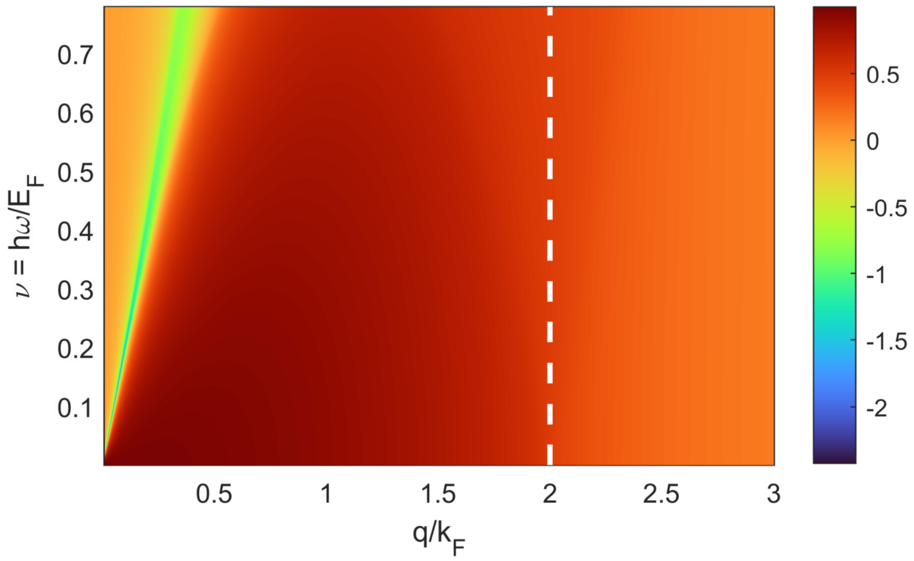

Figure 2.4: Density response function of a non-interacting Fermi gas. The RPA response function for a non-interacting Fermi gas is shown in terms of dimensionless energies and momenta. The white dashed line indicates the momentum $2k_F$, where the function exhibits a slope discontinuity in the static limit. The colormap indicates the value of $\chi_F(q,\omega)$ which is normalized to the long wavelength, static limit $\chi_F(0,0) = \frac{m_F k_F}{2\pi^2\hbar^2}$.

$$F(\bar{q}) = -\chi_F(\bar{q},0) = \frac{k_F^3}{4\pi^2 E_F}\left[1 + \frac{1-(\bar{q}/2)^2}{\bar{q}}\right]\log\left|\frac{1+\frac{\bar{q}}{2}}{1-\frac{\bar{q}}{2}}\right|, \tag{2.35}$$

where as usual k_F and E_F are the Fermi momentum and energy respectively. This function is plotted in Fig. 2.5.

The bosons which are present in the Fermi gas are coupled to the density through the interspecies scattering length, and this effect can be calculated using the above response function. In the case of our Li-Cs system, the low energy scale of the Cs gas as well as the large mass imbalance motivates the static approximation that $\omega = 0$.

The effective interaction potential between point-like Cs atom impurities is given by taking the fourier transform of $F(q)$, which gives the so-called RKKY potential form

$$V_{RKKY}(r) = -g_{BF}^2 \frac{m_F}{8\pi^3\hbar^2}\frac{\sin(2k_F r) - 2k_F r\cos(2k_F r)}{r^4}. \tag{2.36}$$

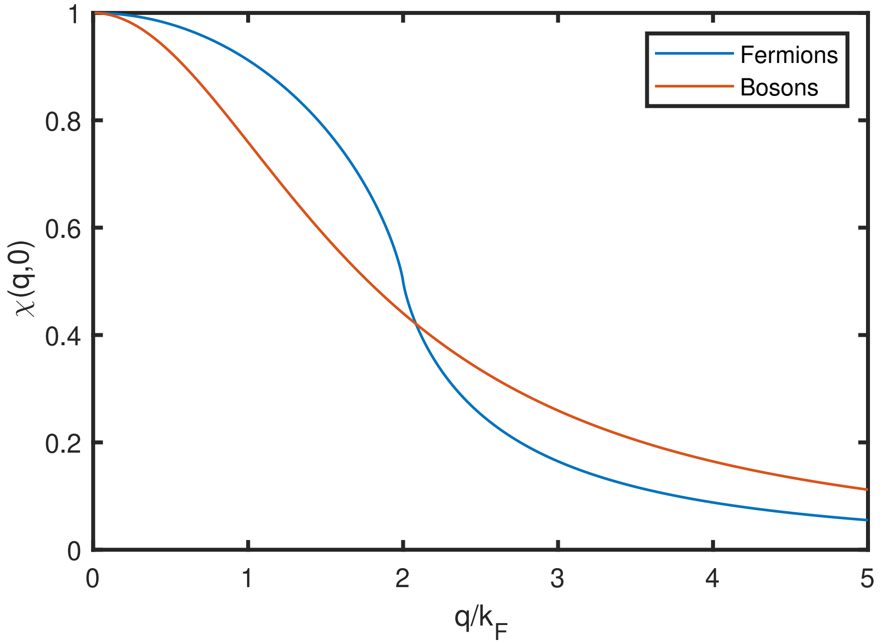

Figure 2.5: Static response functions of a BEC (red) and non-interacting Fermi gas (blue). The two response functions are calculated for homogenous gases with accessible peak densities in typical experiments near the $|a>$-Cs Feshbach resonance. The boson density is set to 5.1 $\times 10^{13}$ cm^{-3} and the fermion density is set to 4.7×10^{11} cm^{-3}. Each curve has been normalized by its zero momentum, zero energy transfer limit $\chi(0,0)$.

The potential exhibits ripples, called Friedel oscillations, at a length scale $\frac{\pi}{k_F}$ associated with a discontinuity in the slope of $F(q)$ at the momentum $q = 2k_F$. Note that this response function has no divergences analogous to the boson case, because there are no long lived excitations associated with the single component Fermi gas. Instead, there is just a broad spectrum of available excitations.

In the low momentum limit, the static Lindhard function becomes:

$$F_0 \equiv F(q=0) = \frac{m_F k_F}{2\pi^2\hbar^2} \tag{2.37}$$

This value F_0 is the density of states at the Fermi surface for a homogenous Fermi gas. This is an intuitive result, because for long wavelengths the system can be treated in the Thomas-Fermi approximation as a uniform system.

2.6 The Mean-Field Phase Diagram

The overall phase diagram of a Bose-Fermi mixture is an interesting topic which has been studied theoretically under various assumptions and approximations. The earliest works studying this in a spin polarized Fermi gas mixed with a BEC are Refs. [49] and [50]. This section outlines the basic picture referred to in the literature as the mean-field phase diagram. At weak interactions, the system is in a miscible phase. At strong repulsion, the system may enter an immiscible phase ("phase-separates") into two components with zero overlap if kinetic energy is neglected. At strong attraction, the mixture is mechanically unstable towards "mean-field collapse," a process by which the density of both components diverge. This phase diagram is the simplest model for the overall behavior of the mixture, but additional complications such as thermalization time scales, particle loss, inhomogeneity, and beyond mean field effects can all modify the observed phase boundaries and even the phases themselves. In this section, we present the overall picture following closely several of these references.

To understand the overall stability of the mixture, the relevant criterion is the change in energy for fluctuations of the particle densities. The total energy of the mixture E_{tot} in terms of the densities n_B and n_F is given by

$$E_{\text{tot}} = \int dr E(n_B, n_F). \tag{2.38}$$

We expand the total energy to second order in small fluctuations of the densities of each component, δn_B and δn_F. Then, we have:

$$\begin{aligned} E(n_B + \delta n_B, n_F + \delta n_F) \approx E(n_B, n_F) &+ \frac{\partial E}{\partial n_B}\delta n_B + \frac{\partial E}{\partial n_F}\delta n_F \\ &+ \frac{1}{2}\left(\frac{\partial^2 E}{\partial n_B^2}\delta n_B^2 + \frac{\partial^2 E}{\partial n_F^2}\delta n_F^2\right) + \frac{\partial^2 E}{\partial n_B \partial n_F}\delta n_B \delta n_F \end{aligned} \tag{2.39}$$

The linear contributions in the expansion of the total energy are then just $\int dr \mu_B n_B$ and $\int dr \mu_F n_F$. Since the individual particle numbers of the bosonic and fermionic component are fixed, these both indepedantly must vanish. To assess stability, one must now check at second order if the configuration is a minimum, a maximum, or a saddle point by looking at the Hessian matrix $H_{f,ij} = \frac{\partial^2 f}{\partial x_i \partial x_j}$. Since $\mu = \frac{\partial E}{\partial n}$, we have

$$H_E = \begin{pmatrix} \frac{\partial \mu}{\partial n_B} & \frac{\partial \mu_B}{\partial n_F} \\ \frac{\partial \mu_F}{\partial n_B} & \frac{\partial \mu_F}{\partial n_F} \end{pmatrix}. \tag{2.40}$$

The determinant of the Hessian and the sign of its diagonal entries are sufficient to indicate the local curvature. If the determinant is positive, this indicates either a minimum or maximum, and the sign of a diagonal element indicates the curvature. If the determinant is negative, it indicates a saddle point. Therefore, the system is stable for a global minimum under the condition:

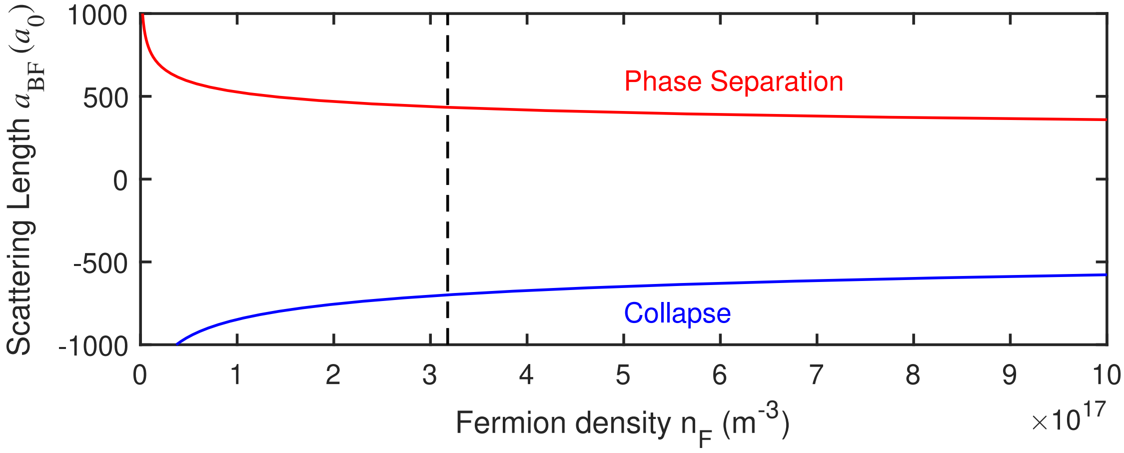

Figure 2.6: Mean-field phase diagram for a homogenous mixture. Theoretical results are shown according to the predictions for a uniform system. The blue line indicates the boundary for collapse, and the red line indicates the boundary for phase separation. The black dashed line indicates a typical peak fermion density in our (inhomogenous) experiments. The boson-boson scattering length is taken to be $a_{BB} = 265a_0$, and the result is independent of the boson density.

$$\frac{\partial \mu_B}{\partial n_B}\frac{\partial \mu_F}{\partial n_F} - \frac{\partial \mu_B}{\partial n_F}\frac{\partial \mu_F}{\partial n_B} \geq 0, \tag{2.41}$$

with the additional constraint that for both species independently $\frac{\partial \mu}{\partial n} \geq 0$.

First, let us consider a homogenous BF mixture, where our desired results can be obtained analytically. We start from the chemical potentials of each species in the Thomas-Fermi approximation and at zero temperature. The chemical potential of the bosons μ_B is given by

$$\mu_B = n_B g_{BB} + g_{BF} n_F, \tag{2.42}$$

where n_B is the (condensed) boson density, g_{BF} is the interspecies interaction coupling constant, and n_F is the fermion density. The fermion chemical potential is

$$\mu_F = E_F + g_{BF} n_B = \frac{\hbar}{2m_F}(6\pi^2 n_F)^{2/3} + g_{BF} n_B. \tag{2.43}$$

The elements of the matrix H_E are then

$$H_E = \begin{pmatrix} g_{BB} & g_{BF} \\ g_{BF} & \frac{2\hbar}{6m_F}(6\pi^2)^{2/3} n_F^{-1/3} \end{pmatrix}, \tag{2.44}$$

resulting in the stability condition,

$$\frac{2g_{BB}}{3}\frac{\hbar}{2m_F}(6\pi^2)^{2/3} n_F^{-1/3} - g_{BF}^2 \geq 0 \tag{2.45}$$

which can be re-arranged to give

$$g_{BB} \geq \frac{3}{2} g_{BF}^2 \frac{n_F}{E_F} = F_0 g_{BF}^2. \tag{2.46}$$

This is equivalent to the statement that the system becomes unstable towards collapse when the bare boson-boson repulsion g_{BB} is overcome by mediated attraction as described in the previous section.

A more complicated argument that does not originate from an expansion in small density fluctuations predicts the condition for a saddle point, as described in Ref. [50]. This occurs at a critical fermion density $n_{f,c} = \frac{3}{4\pi a_{BF}^3}\left[\frac{a_{BB}/a_{BF}}{(1+m_F/m_B)(1+m_B/m_F)}\right]^3$. This condition, as well as the condition for collapse are shown in Fig. 2.6. The regime of phase-separation corresponds to the spontaneous formation of a separated pure bosonic phase and pure fermionic phase.

In a nonuniform system, we can model the phase diagram by adding an additional potential energy for each species V_B and V_F that contains the trapping potential and allowing n_B and n_F to be functions of space. Then, we can assign the instabilities based on the central densities, which will be the first to both collapse and phase separate. We start from the zero-temperature Thomas-Fermi expressions for the chemical potential of each species:

$$\mu = g_{\mathrm{BB}} n_{\mathrm{B}} + V_{\mathrm{B}} + g_{\mathrm{BF}} n_{\mathrm{F}} \tag{2.47}$$

$$E_{\mathrm{F}} = \frac{\hbar^2}{2m_{\mathrm{F}}}(6\pi^2 n_{\mathrm{F}})^{2/3} + g_{\mathrm{BF}} n_{\mathrm{B}} + V_{\mathrm{F}}, \tag{2.48}$$

There is no simple analytical form to solve for the resulting density profiles as a function of interspecies scattering length a_{BF}. However, they can be found numerically. The simplest way to calculate the density profiles and phase diagram is to self consistently evaluate the chemical potential of each species by iteration until the simulation converges, see Appendix C. When it converges, it will converge to the ground state density distribution, and if it fails to converge that can be understood as an instability towards collapse. We define phase separation as zero density overlap in the center of the trap, but it is not a well defined phase transition for an inhomogenous gas.

While there is no analytic solution, we can consider the central densities approximately and make reasonable estimates for the phase boundaries in our system. Due to to the significant density mismatch in our mixture, only a small fraction of the total fermions are displaced or trapped by the condensate even for sizeable scattering lengths. Typical peak densities with no interactions are 5×10^{13} cm^{-3} for bosons and 3×10^{11} cm^{-3} for fermions, and typical condensate Thomas-Fermi radii are about 50 microns in the long axis and 2 microns in the short axis. The fraction of fermions occupying this volume is then roughly $\frac{n_F}{N_F} R_x R_y R_z \sim< 1\%$. Even accounting for the effect of mean field attraction only a few percent at most can be confined. Therefore, we can approximate the Fermi energy in the mixture as the bare Fermi energy for the trapped Fermi gas. Furthermore, the interaction energy $g_{BF} n_F$ tends to be quite small compared to the boson chemical potential even for large scattering lengths. These reasons motivate the approximate expression at the trap center:

$$\mu = g_{BB} n_B + g_{BF} n_{F0} \left(1 - \frac{g_{BF} n_B}{E_F}\right)^{3/2} \tag{2.49}$$

where n_{F0} and n_B are the densities of each species with no interspecies interactions. This

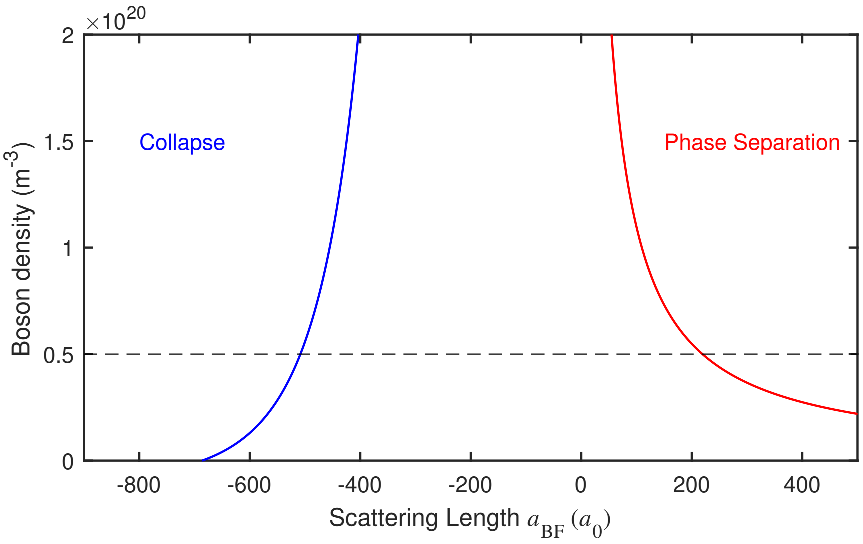

Figure 2.7: Mean-field phase diagram for a inhomogenous mixture. Theoretical results are shown according to the predictions for the nonuniform system with simplifying approximations (see text). The blue line indicates the boundary for collapse, and the red line indicates the boundary for phase separation. The black dashed line indicates a typical peak boson density in our (inhomogenous) experiments. The boson-boson scattering length is taken to be $a_{BB} = 265a_0$, and the peak fermion density is taken to be an experimentally reasonable 3.5×10^{17} cm^{-3}.

permits the calculation of the collapse boundary according to vanishing compressibility $\frac{\partial\mu}{\partial n_B} = 0$ and the phase separation boundary as $g_{BF}n_B = E_F$. The critical collapse condition can be evaluated as

$$n_{B,c} = \frac{E_F}{g_{BF}}\left(1 - \frac{4E_{F,0}^2 g_{BB}^2}{9g_{BF}^4 n_{F0}^2}\right) \tag{2.50}$$

where $n_{B,c}$ is the critical boson density for collapse. See Fig. 2.7 for the resulting phase diagram.

The system can be more accurately modelled by including a kinetic energy term for each species. For the bosons this is very straightforward, and just looks like a standard Gross-Pitaveskii equation. For the fermions, going beyond the Thomas-Fermi approximation can be tricky, and we typically do so in a hydrodynamic approximation. Again, we refer the reader to Appendix C for more details. We note that ground state results in our system do not depend significantly on the inclusion of fermion kinetic energy. However, as demonstrated in experiments by R. Grimm's group [51, 52], corrections beyond the Thomas-Fermi approximation can be very important in the regime of strong repulsion and phase separation, where they play a role in the properties of the interface between species.

2.7 Excitations

In the previous section, we discussed the response functions of the Fermi gas and Bose-Einstein condensate. The quasiparticle excitations of the BEC follow the Bogoliubov dispersion, and that is reflected in the divergence of the response function. However, if the BEC is immersed in a Fermi gas, as in our experiments, the density profiles are coupled to each other through the interaction term $g_{BF} n_{\mathrm{B}} n_{\mathrm{F}}$. Through this coupling, the Fermi gas responds to phonons which are travelling through the BEC according to the Lindhard function, and the resulting energy shift leads to a change in the BEC dispersion. This argument is laid out in a microscopic calculation in Ref. [53] and a more transparent form in Ref. [54]. Following Ref. [54], we can write the coupling between the density fluctuations δn_B and δn_F of the two species as a matrix:

$$\begin{pmatrix} 1 & g_{BF}\chi_B \\ g_{BF}\chi_F & 1 \end{pmatrix} \begin{pmatrix} \delta n_B \\ \delta n_F \end{pmatrix} = - \begin{pmatrix} \chi_B V_B \\ \chi_F V_F \end{pmatrix}. \tag{2.51}$$

Inverting the matrix on the left yields $\frac{1}{1-g_{BF}^2\chi_B\chi_F}\begin{pmatrix} 1 & -g_{BF}\chi_B \\ -g_{BF}\chi_F & 1 \end{pmatrix}$ giving the relation:

$$\delta n_b = \frac{1}{1-g_{BF}^2\chi_B\chi_F}(\chi_B V_B + g_{BF}\chi_B\chi_F V_F). \tag{2.52}$$

This expression tells us how external potentials on each component of the gas create perturbations to the boson density. The boson dispersion corresponds to excitations only through the boson potential V_B. Therefore, the response function of the condensate χ_B is modified to the new effective response

$$\chi_B' = \frac{\chi_B}{1 - g_{BF}^2 \chi_B \chi_F} \tag{2.53}$$

and the collective modes correspond to the divergence of this modified response function, as they did to the original χ_B discussed in Section 2.5. Inserting χ_B, we see that this corresponds to

$$\frac{n_b q^2}{m_B(\omega^2 - \omega_k^2)} = \frac{1}{g_{BF}^2 \chi_F}. \tag{2.54}$$

Re-arranging gives

$$\omega = \omega_k \sqrt{1 + g_{BF}^2 \chi_F n_B \frac{q^2}{\omega_k m_B}}. \tag{2.55}$$

This is actually a rather intuitive result. It says that the Lindhard function is excited at the ω and k determined by the bare boson Bogoliubov distribution, and this results in a small energy correction. At small q, the result is that the modified sound speed is the sound speed expected for a condensate with effective interaction strength $g_{BB} - g_{BF}^2 F_0$.

We take a moment to comment on the more first principles, microscopic calculation from Ref. [53] which starts from the Hamiltonian in terms of the Bogoliubov phonons. It arrives at the expression

$$\hbar\omega = \omega_k + g_{BF}^2 n_{\mathrm{B}} \frac{\epsilon_k^B}{\omega_k} \chi_F(k, \omega_k/\hbar). \tag{2.56}$$

The result obtained in this way actually agrees to second order in g_{BF}, which can be seen by expanding Eq. (2.55) for small changes in the dispersion.

We evaluate Eq. (2.56) for various system parameters and show the resulting dispersions in Fig. 2.8. For $k \ll k_F$ the effect of the Lindhard function is to simply reduce the sound speed. In the experimental work presented in Chapter 6 , we are still at wavelengths long compared to both the healing length ξ and $1/k_F$, meaning that we excite only this low momentum region of the Lindhard function and expect only sound speed shifts. Information

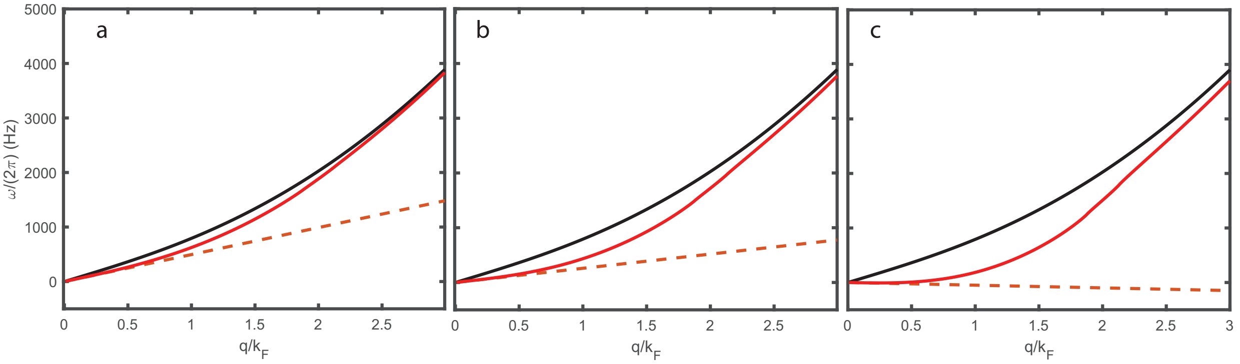

Figure 2.8: BEC dispersion modified by fermions. The bare BEC dispersion (black solid line) and the modified BEC dispersion (red solid line) are shown for realistic system parameters. The red dashed line is the limit calculated for the sound speed in Ref. [53]. Note that this line is tangent to the full calculation for low momenta. The calculation is performed for 30,000 bosons and 20,000 fermions in reasonable trap frequencies for our experiment. The results are shown for three different magnetic field values on the attractive side of the Li-Cs Feshbach resonance at 892.65 G which correspond to interspecies scattering lengths (a) $-500a_0$, (b) $-725a_0$, and (c) $-950a_0$.

can be learned about the higher momentum portion for example using Bragg spectroscopy (see Section 7.1) or by carefully studying the propagation of density perturbations.

As a note of interest, the presence of the Bose-Einstein condensate also induces a sound mode in the single component fermion gas which is otherwise non-interacting and does not support such excitations [55].

2.8 Solitons

The GPE is a nonlinear wave equation, and such equations are capable of supporting "solitary wave" solutions, or "solitons" when the profile of the excitation can balance out the dispersion. There are a variety of types of solitons that can form in Bose-Einstein condensates. In general, solitons are either dark and correspond to density depletions, or bright and correspond to enhancements. Dark solitons can be created optically [56], and bright solitons can be formed by collapse and modulational instability [57, 58]. Dark solitons travel with a velocity determined by their density amplitude δn, according to $v = c_B\sqrt{1-\delta n/n_0}$ where

c_B is the Bogoliubov sound speed and n is the peak condensate density. These are closely related to the propagating density excitations described in Chapter 6, and hence travel with the same speed, but those do not exactly correspond to solitonic solutions.

There has been several theoretical investigations into Bose-Fermi solitons as well [59–62]. These solitons are stabilized by the interspecies interactions, and can form for both attractive and repulsive scattering length a_{BF}. Bright solitons in the condensate can either look bright ($a_{BF} < 0$) or dark ($a_{BF} > 0$) in the Fermi gas. We believe that the solitons we observed in Chapter 5 correspond to the bright-bright case, but did not have in-situ Fermi gas imaging in place to confirm at the time of that work. Note that the presence of the bosons can create solitons in the non-interacting spin polarized Fermi gas, even though they cannot be supported by the fermions alone.

CHAPTER 3

EXPERIMENTAL APPARATUS

In this section, we describe the apparatus which was used to perform the science in this thesis. J. Johansen's thesis (Ref. [34]) contains an in-depth discussion of the systems details. Presented here is a less thorough overview. There are some very significant apparatus upgrades, however, which are the capability for *in situ* imaging and potential projection using a high-resolution objective. These are discussed in considerably more detail in Section 3.7.

3.1 General Set-Up

To study ultracold atomic gases, it is necessary to create an environment which is free from (comparably) hot air molecules which would kick atoms out of their trapping potential upon collision. A room temperature (~ 300K) atom is of enormous energy compared to the typical energy scales accessed by optical trapping. This leads to a finite lifetime (called vacuum or 1-body lifetime) that limits the time over which a particular atomic sample can be studied.

Sufficient vacuum lifetimes are achieved by performing experiments at ultra high vacuum (UHV) inside of a steel vacuum system which has been carefully designed and assembled. Components must be thoroughly cleaned prior to assembly, and once assembled must be heated to hundreds of degrees C for long periods of time ("baked") in order to allow the material to outgas. Our vacuum system has several major components. It contains a set of ovens, in which our Li and Cs source material is stored and heated, a small chamber with viewports for creating a 2D MOT of Cs, a long tube which provides differential pumping and also forms part of the Zeeman slower, 2 ion pumps, a Ti sublimation pump, and a main science chamber. The vacuum system must of course be sealed to maintain low pressure, but it has various windows which allow the passage of laser light which is used to cool, trap, and probe the atomic samples inside. See Fig 3.1 for a schematic depicting the main science

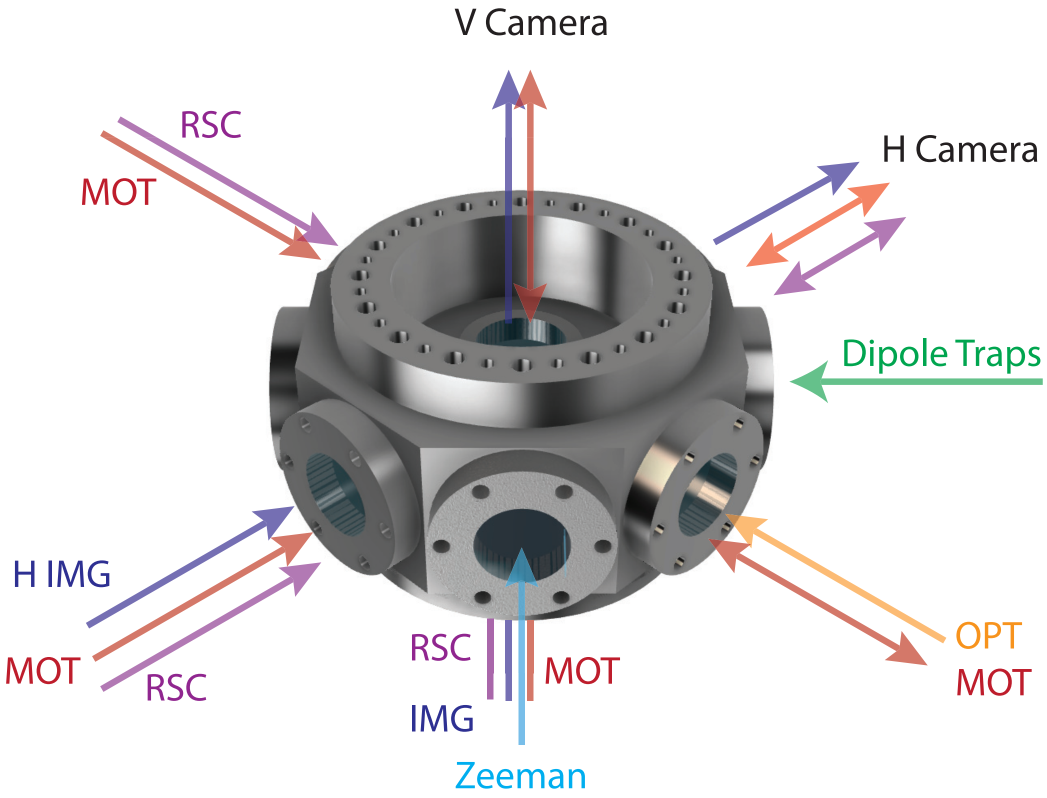

Figure 3.1: Schematic of vacuum chamber and laser light. The atomic samples are at the center of the vacuum chamber, and are exposed to various laser beams from different beam paths and laser sources throughout the experimental sequence. The magneto-optical trapping (MOT) beams come in along three perpendicular directions and are retro-reflected. The horizontal and vertical imaging beams travel along with the MOT beams but are transmitted by the same optics which reflect the MOT, see Fig. 3.9. The Raman sideband cooling (RSC) lattice beams form a lattice using 3 beams and a single retro-reflection.. The Zeeman beam is aimed through the Zeeman slower and hits the back of the ovens (not shown.) The dipole traps all enter through the same window and are dumped on the other side of the chamber. Images can either be taken vertically or horizontally, with the horizontal camera placed at a 45 degree angle with respect to the long axis of the trapped clouds.

chamber and beam paths through the viewports.

The top and bottom of the vacuum chamber have recessed viewports, which allow objects to be brought close to the atomic sample. It is important for these experiments to be able to control the magnetic field that the atoms experience, which is generated primarily by two water cooled copper coils which are mounted to these recessed viewports, see Refs. [34, 63] for further details. To summarize, the magnetic field coils consist of many stacked copper discs with water channels carrying water in the direction parallel to the axis of the coil, rather than in series as with typical hollow conductor coils. These coils carry about 300 A of current during the high field portions of a typical experimental sequence, and are capable of generating fields from 0-1000 G.

The recessed viewport on the top of the vacuum chamber is additionally used since recent hardware upgrades to bring a high-resolution microscope objective near the atoms and obtain high numerical aperture (NA), see Section 3.7. The lower recessed viewport will additionally be used in the near future to bring a small, much faster coil very close to the atoms to perform fast modulation of the magnetic field and therefore the atomic interactions.

Throughout the experimental sequence, it is necessary to control a variety of signals, such as various optical powers, shutters, and coil currents. This control is performed using a computer running LabView and National Instruments PCI/PCIe cards. The LabView program intakes a series of voltage and timing instructions on various channels, which are then uploaded to the cards and executed according to an external clock. For more details about the computer control, see Appendix A.

3.2 A Small Amount of Atomic Physics

In the work presented in this thesis, atoms are tools which we are using to study many-body physics, rather than the primary focus of study themselves. It is nonetheless very important to have a working knowledge of the basic behavior of atoms and their interaction with electric

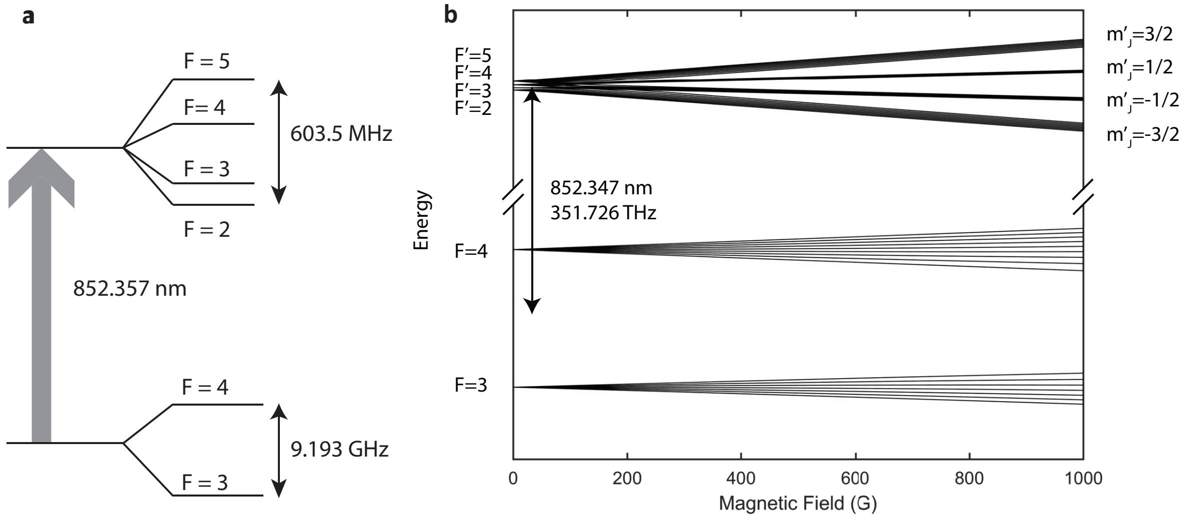

Figure 3.2: Level structure of the D2 transition in Cs over the accessible magnetic field range of the experiment. (a) Cs D2 transition structure at zero field. (b) As a function of magnetic field, the various magnetic sublevels split. The ground state of Cs is in the intermediate regime at 1000 G, but the excited state has already entered the Paschenbach regime by ∼200 G. We perform laser cooling near zero field, then evaporation and science near 900 G. See Ref. [64] for the various constants necessary to calculate these levels.

and magnetic fields.

The atoms discussed in this thesis are alkali atoms, so their outer shell contains one unpaired electron. This means that they are very similar in structure to hydrogen, although they have in general more internal states. Various excited internal states have lifetimes (or equivalently, linewidths Γ) which are due to transition probabilities to lower lying states. Atoms can be transferred between states by any perturbation of their Hamiltonian which couples the relevant states together, but the most common method for controlling these transfers is using light.

For both of our atomic species, we work on the D2 transition, which is the electronic transition from the $S_{1/2}$ ground state to the $P_{3/2}$ excited state. The structure of the relevant internal states for Cs is shown in Fig. 3.2 and for Li in Fig. 3.3. Due to unfavorable two-body relaxation rates in Cs, it is only possible to create stable BECs of the absolute lowest internal ground state. Li, however, being fermionic, can be stably created in a variety of internal

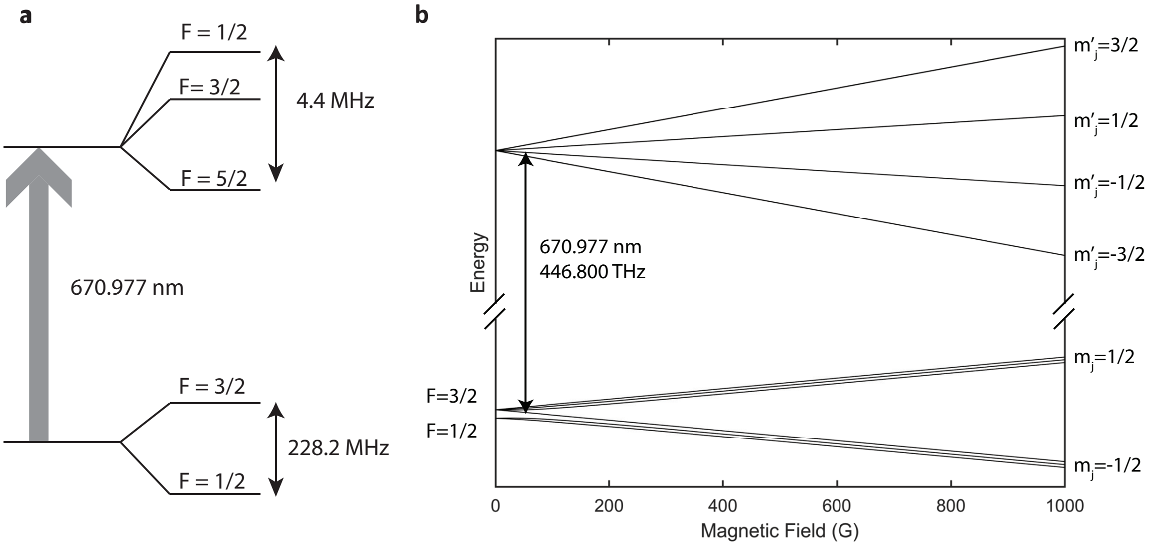

Figure 3.3: Level structure of the D2 transition in Li over the accessible magnetic field range of the experiment. (a) Li D2 transition structure at zero field. (b) As a function of magnetic field, the various magnetic sublevels split. Both the ground and excited states are in the Paschenbach regime at 900 G. Note that the four m_j' levels in the excited state each contain a set of $m_I' = \{-1, 0, 1\}$ states, but their splittings are only a few MHZ and unresolvable on this graph. We perform laser cooling near zero field, then evaporation and science near 900 G. See Ref. [65] for the constants necessary to calculate these levels.

states due to Pauli blocking of collisions. Conventionally, the Li ground states are labelled from the bottom up, either by the numbers 1-6 or the letters $a - f$. We will use the letters $a - f$, and for all of the science data in this thesis we are working with the absolute lowest internal state, $|a\rangle$.

The states are labelled at zero field according to the quantum number F which is the total angular momentum $F = I + L + S$, where I is the nuclear spin, L is the electron orbital angular momentum, and S is the electron spin. This is referred to as the Zeeman regime, where the states shift in a magnetic field according to their magnetic quantum number m_F as $\Delta B = \mu_B g_F m_F B$, where g_F is the hyperfine Lande g-factor. Both the lowest internal state of Cs and states $a - c$ in Li are "high-field seeking," meaning that they can be trapped (for 2 directions) by a magnetic quadrupole trap. This type of confinement provides the primary weak confinement along one direction in our degenerate samples.

At high fields, the interaction between the nucleus and electron is weak compared to their interaction with the external field, and they decouple. This is referred to as the Paschenbach regime, and the appropriate quantum numbers are no longer F but instead $J = L + S$ and I. The resulting field shift is $\Delta B = \mu_B(g_J m_J + g_I m_I)B$ where g_J and g_I are the appropriate g-factors.

Although there are many states in each diagram shown in Figs. 3.2 and 3.3, often the drive is tuned to frequencies near resonance and the system can be reduced to approximately two levels. For times short compared to the linewidth of the transition Γ, the system undergoes Rabi oscillations between the ground and excited state at the Rabi frequency $\sqrt{\Omega^2 + \delta^2}$ with contrast $\frac{\Omega^2}{\Omega^2+\delta^2}$, where δ is the detuning. For times long compared to the linewidth, the photon scattering rate is $R_{\mathrm{sc}} = \frac{\Gamma}{2}\frac{\Omega^2/2}{\delta^2+\Omega^2+\Gamma^2/4}$. We are in the latter limit for all of the interaction between atoms and light described throughout the thesis except for microwave transitions in the ground state manifold of Cs. The Rabi frequency can be connected to the intensity of light and saturation of the transition through $I/I_s = \frac{2\Omega^2}{\Gamma^2}$, which connects this

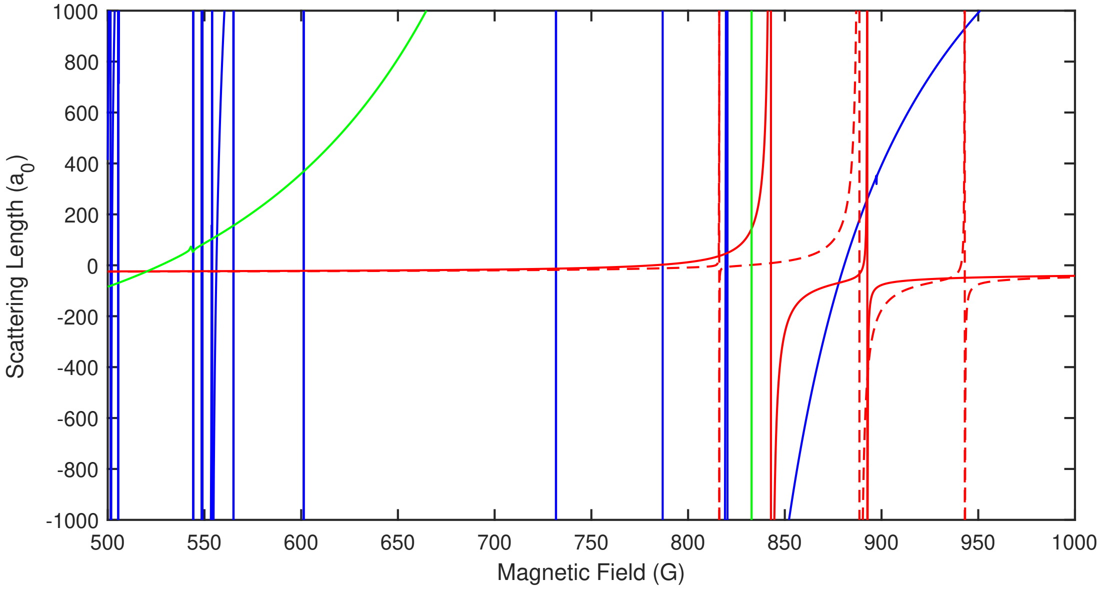

Figure 3.4: Atomic interaction strengths. Scattering lengths of all relevant species combinations are plotted from 500 - 1000G. Shown are the Cs-Cs (in $|3,3\rangle$) (blue solid line), Cs-Li$_\mathrm{a}$ (red solid line), Cs-Li$_\mathrm{b}$ (red dashed line), and Li$_\mathrm{a}$-Li$_\mathrm{b}$ (green solid line) scattering lengths. Note that the behavior of the Cs scattering length is only favorable for evaporation near 900 G on this plot. The curves are from the Refs. [66–68]

scattering rate to the cross-section expressions given in Section 3.7.

3.3 Feshbach and Efimov Resonances in Li-Cs

The Feshbach resonances for the lowest two spin states of Li colliding with the ground state of Cs have been characterized experimentally both by the Weidemüller group and earlier members of the Chin group. These Feshbach resonances are very powerful experimental tuning knobs, both for attaining ultracold gas samples in the first place and further science once they have been created. Tuning the interactions permits efficient evaporative cooling, and also allows systematic investigation of ultracold gas systems from weak to strong interactions.

Our experiment involves the two lowest hyperfine states of Li ($|a\rangle$ and $|b\rangle$) and the absolute hyperfine ground state of Cs ($|3,3\rangle$). Their scattering lengths are plotted in Fig.

3.4. For science beyond system preparation, the experiments in this thesis all take advatange of the $|a\rangle$-Cs Feshbach resonance at 892.648 G, which has a width of $\Delta = 2$G and strength $s_{\text{res}} = 0.02$ [68].

There are additionally very well studied Efimov resonances. The one most likely to be relevant for the work in this thesis is for Cs-Cs-$|a\rangle$ at 892.689 G, which corresponds to $a_{\text{BF}} = -3300a_0$. The three-body interactions near this resonance may play a role in physics near the Feshbach resonance pole. The behavior of degenerate Bose-Fermi mixtures near such an Efimov resonance is an interesting avenue of future study, see Section 7.2.

In order to successfully perform evaporative cooling, it is important to have sufficient interaction strength for good thermalization rates (which depend on the elastic cross section $\sim a^2$), but not too high so as to lose too many atoms to three-body loss ($\sim a^4$), which is the dominant atomic loss process (in a good vacuum). Roughly speaking, values of about $\sim 100a_0$ are good for bosons, but the scattering length for Cs-Cs collisions in the lowest hyperfine state is about -2500 a_0 at zero field. In this sense, working with Cs beyond the single particle limit requires some tuning of the interactions, and in fact condensates have only been reported near the zero-crossings near 20 G and 900 G.

It is therefore extremely fortunate that there is an interspecies Feshbach resonance near 892 G, where we are able to create BECs of Cs and also control the interactions between the Cs and Li atoms. This is the core feature of the Li-Cs mixture which enables the science presented in the rest of this thesis and establishes it as a valuable platform for studying the many-body physics of Bose-Fermi mixtures.

3.4 Laser Cooling

Each of our atomic species must be brought from above room temperature ($\sim$ 330C for Li, $\sim 50C$ for Cs) down to temperature scales low enough that their de Broglie wavelengths are comparable to their inter-particle spacing. This is done using a combination of laser cooling, which transfers the thermal energy of atoms into scattered photons, and evaporative cooling in optical traps.

Laser cooling schemes are broadly separated into "Doppler" and "sub-Doppler" techniques, named for their lowest theoretically achievable temperatures $T_D = \frac{\hbar\Gamma}{2k_B}$ and $T_R = \frac{\hbar^2 k_L}{mk_B}$. The Doppler limit is defined by the decay rate of the cooling transition, while the limit of sub-Doppler cooling, the recoil limit, is limited by the wavelength of the light. For us, these correspond to $T_D \approx 120\,\mu\text{K}$ and $T_R \approx 200$ nK for Cs and $T_D \approx 140\,\mu\text{K}$ and $T_R \approx 3.5\,\mu\text{K}$ for Li.

Cooling schemes are most straightforward to enact using atomic species which have "closed" or "cycling" transitions, which allow many scattering events to occur before the atom leaks into a state which is no longer resonant. These are determined by the available internal states and transition selection rules. In alkali atoms, the structure of the D2 transitions allows for such transitions between the "stretched" states ($|m_F| = F$) in the ground and excited manifolds. This fact, combined with their relatively simple electronic structure resulting from only a single valence electron, has led to them being the historical workhorses of ultracold atomic physics. We live in exciting times, however, and this is rapidly changing with the cooling of many different types of elements (such as the lanthanides and alkaline-earths) with various advantages and drawbacks for quantum simulation and computation.

The overall process of laser cooling works essentially the same for both Cs and Li atoms down to the Doppler limit, but below that they are not amenable to the same techniques. This is because the hyperfine splitting is unresolved for ^{6}Li, meaning that the separations are smaller than the linewidths (see Fig. 3.3). For this reason, we employ the sub-Doppler technique of degenerate Raman Sideband Cooling (dRSC) [69] on Cs, but not Li. There are, however, other techniques which have been very successful for efficient sub-Doppler cooling of Li, in particular grey molasses on the D1 line [70]. This capability is not possible for us at the time of this thesis, but it is a potential upgrade which can be implemented if we wish to reach significantly larger atom numbers in our degenerate Fermi gas .

For each of our atomic species, we have a set of < 1 W lasers near resonant with the D2 line to perform laser cooling as well as absorption imaging. For an in-depth discussion of these laser systems, I refer the reader to Ref. [34]. Essentially, each set has a "Reference" laser, which is locked to a vapor cell which provides an absolute frequency reference, then a "MOT" and "Repump" laser which are locked to the reference using the optical interference (a beat-note) on a photodiode. The MOT and Repump lasers play the roles of providing the cooling light for laser-cooling, and preventing the sample from "going dark" by accumulating in internal states which are not resonant with the cooling light. In the case of Cs, there are an additional two lasers used to create the dRSC lattice. A combination of shutters, acousto- and electro- optical modulators (AOMs/EOMs), and laser current/piezo control determine the frequencies and intensities of light to which the atomic sample is exposed throughout the experiments.

The typical laser cooling sequence to produce degenerate Cs and Li $|a\rangle$ mixtures is summarized below. For more information about each dipole trap, see Section 3.5.

1. *Li MOT loading.* We begin the sequence by performing a 10 second load of Li atoms by setting the Zeeman coil and main coil currents to the Li configuration and turning on the Li Zeeman and MOT beams.

2. *Li CMOT.* We ramp the beam powers, detunings, and field gradient to create a higher density atomic gas sample for loading into the BFL dipole trap. At this stage, we typically image about 11 million atoms at < 500 µK.

3. *BFL loading / pre-evaporation.* We ramp up the BFL power and switch off the laser cooling light, then perform some initial fast cooling of the resulting Li $|a\rangle - |b\rangle$ spin mixture at resonant interactions using the appropriate Feshbach resonance near 850 G [66]. Note from Fig. 3.3 that these are the two states are adiabatically connected to the

absolute internal ground state at zero field. Once they have been initially somewhat cooled, we translate them away from the MOT loading region using a motorized stage. The evaporation process can be done quickly at strong interactions because three-body loss is suppressed for two-component fermion mixtures.

4. *Cs MOT loading.* We load a Cs MOT for 3.7 seconds by switching the Zeeman current and main current configurations to be appropriate for Cs and turning on the Cs Zeeman and MOT beams. This is done while the Li sample is not present in the MOT region to avoid near resonant light induced loss.

5. *Cs CMOT.* We ramp the beam powers, detunings, and field gradient to increase the atomic density in preparation for loading into the RSC lattice.

6. *Cs Molasses.* We release the atoms from the field gradient and perform 5 ms of optical molasses / polarization-gradient cooling. During this time, the gas slowly expands since it is no longer confined. We typically image $\sim$ 80 million atoms at $\sim$ 10 µK at this stage.

7. *Cs RSC.* We load the Cs gas into the RSC lattice, and perform cooling using the optical pumping beam as cooling light and the MOT beam as a repumper. In this process, atoms are cooled through transitions that remove vibrational quanta from the motional states of the trapped atoms in the wells of the lattice. At this stage, we typically image $\sim$ 15 million atoms at $\sim$ 3 µK.

8. *State purification / OTOP Loading.* RSC pumps most of the atoms into the lowest internal state of Cs. We perform levitation using a field gradient (31.1 G/cm) to allow only those atoms to remain and purify the sample. After the spin state is purified, we ramp down the levitation gradient while loading into the OTOP which is being modulated to increase trapping volume out of the RSC. Finally, we ramp up to high magnetic field where the Cs scattering length is appropriate for evaporation, and reduce

the modulation on the OTOP to zero. After this stage, we typically image ∼ 3 million atoms at ∼ 6 µK.

9. *Evaporation.* We then cool the Cs atoms to ∼ 1 µK via forced evaporation for about 10 seconds by reducing the power in the OTOP beam according to an optimized trajectory and keep ∼ 1.2 million Cs atoms. At the same time, we evaporate Li in the BFL to a point where we typically image ∼ 90 k Li atoms at ∼ 5 µK. The exact number and temperature we measure here is prone to significant drift month to month. We think this is due to drifts in the exact trap depth near the very bottom of the BFL intensity control voltage.

10. *State purification / Li transfer to dual color.* We transfer the atoms from the BFL into the dual color trap by translating the stage back to the science region and lowering the BFL intensity while ramping up the dual color beam powers. We typically image ∼ 15k Li atoms at this stage. We bring the Li atoms to about 300 nK in the dual color trap, then perform a resonant light pulse to eject $|b\rangle$ atoms out of the trap. It is important to keep $|b\rangle$ up until this point, so that the fermions can thermalize during evaporation (otherwise they would be non interacting.)

11. *Cs transfer to dual color.* We load the Cs into the dual color trap by manipulating the OTOP position, power, and the power in each of the dual color beams. See Section 3.6 for more detail.

12. *Sympathetic cooling.* We perform a final round of forced evaporation where the Li and Cs are cooled together and thermalizing. This can be done on either side of the Feshbach resonance, and works best for interspecies scattering lengths $|a_{BF}|$ between 100-200 a_0.

After all of the above steps, which take about 27 seconds, we end up with dual degenerate mixtures of Li $|a\rangle$ and Cs [35]. We consider this the initial preparation phase of an experiment.

3.5 Dipole Trapping

Throughout the experimental stages outlined in the previous section, the samples are loaded into off-resonant dipole traps which function as external potentials. The strength and sign of this potential are determined by the wavelength λ and intensity I of the light according to [71]:

$$U_{\text{dip}}(\vec{r}) = -\sum_i \frac{3\pi c^2}{2\omega_{0i}^3}\left(\frac{\Gamma_i}{\omega_{0i}-\omega} + \frac{\Gamma_i}{\omega_{0i}+\omega}\right) I(\vec{r}), \tag{3.1}$$

where c is the speed of light, ω_{0i} are atomic resonance frequencies and Γ_i are their linewidths. The dipole force falls off more slowly with large detunings from atomic resonance than the scattering rate, which permits long lifetimes in optical traps if sufficiently off resonant light is used. The strength of the potential for various wavelengths is shown in Fig. 3.5 for both Li and Cs. The scale of the off-resonant trapping force necessitates high power lasers with outputs > 1 W. These traps are often characterized by the trap depth (peak potential felt by the atoms), and the (easily measured) trap frequency, given by the Taylor expansion of the trapping potential about its minimum.

There are four dipole trapping beams, which we denote the BFL, the OTOP, the 1064, and the 780, the latter two of which share an optical fiber and are dubbed the dual color. The BFL is a crossed dipole trap with a maximum ~ 80 W per arm that can be translated using a motorized stage. Note that this laser is quite powerful, and is required due to our lack of sub-Doppler cooling for Li. Even with this very bright light source, we only manage to load a small fraction of the coldest Li atoms out of the Li CMOT and into the trap. The OTOP is a max ~ 15 W beam path which has a ~ 1 m path length after being diffracted by an AOM with tunable drive frequency. By modulating the drive frequency at 100 kHz, the beam is dynamically expanded in order to increase loading volume out of the RSC, and by

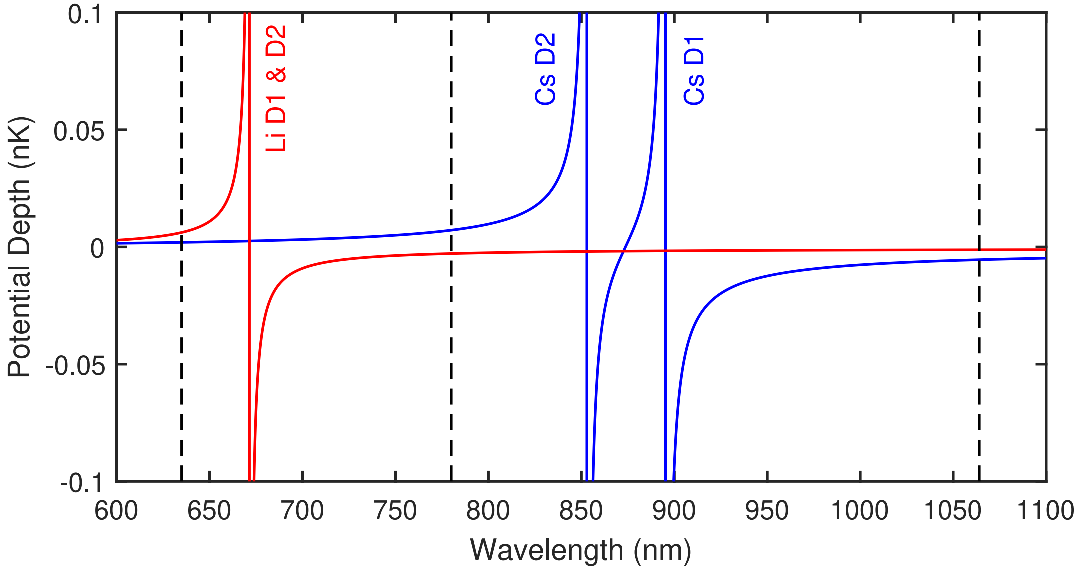

Figure 3.5: Optical dipole force on Li and Cs atoms. Trap depth experienced by Li (red solid line) and Cs (blue solid line) exposed to light of intensity 1 mW/cm^2. Black dashed lines indicate wavelengths of off-resonant light used on the atoms in our experiment. They correspond to the DMD at 635 nm, the dual color beam at 780 nm, and the two dipole traps at 1064 nm.

tuning the average value of the drive frequency the position along the gravity direction can be controlled. The dual color trap creates two foci displaced vertically by $\sim$ 10 µm at the location of the atoms, with the 780 nm lower than the 1064 nm beam. This allows for the compensation of gravitational sag between the two species, because 780 is blue-detuned and repulsive for Cs but red-detuned and attractive for Li. It also provides an additonal useful degree of freedom to control the separation of the gases when mixing them together.

Some small additional notes for future graduate students: two of the laser sources that were in use at the time of Ref. [34] have been replaced in the experiment. The Mephisto MOPA and the small IPG fiber laser (SFL) have been replaced with a single 30 W system from Precilasers. Also, the dual color 780 nm intensity lock pick off path has been changed to minimize some observed contamination from the 1064nm beam. The ZDT path currently has no input light, but much of the beam path still exists and could be used in the future if picked off from the remaining Precilasers power.

3.6 Trap-Mixing

As a general strategy, we perform laser cooling and initial evaporative cooling separately on the two species, only mixing them together once they have reached temperatures of about 300 nK. This allows the cooling of each species to be, for the most part, troubleshot and optimized separately. Many details of the laser cooling process can be found in earlier sections of this thesis and Ref. [34]. At the time of that thesis, the experimental procedure was developed to create cold (but still thermal) gases in the hundreds of nK with tunable overlap for the purposes of doing careful three-body-loss measurements. After that work was completed, we optimized the later stages of the experiment to achieve degeneracy.

We began by optimizing the evaporation of Cs in the OTOP, and were able to create BEC's in the trap as evidenced by a bimodal distribution in time of flight. Due to the slow dynamics in the trap, which has a trap frequency $(\omega_x, \omega_y, \omega_z)/(2\pi) \approx (6.6, 20, 150)$ Hz, we ended up doing forced evaporation for about 10 seconds to reach degeneracy. However, we found that creating the BEC in the OTOP and then attempting to transfer it into the final trap tended to cause too much heating, due to the low energy scale. The stability of the process also left something to be desired. We were also not interested in loading the Li into this trap, because we did not want the final science trap to have the long free-space path length necessary to permit modulation of the OTOP, which is a useful tool during preparation but a pain for stability.

We observed that about 300 nK was a reasonable energy scale where we could move the atoms between the traps without causing too much heating and the system was less sensitive to instability in the optical potentials. The most robust scheme, which we have continued to implement, is summarized in Fig. 3.6. First, while the OTOP is well separated from the other beams, we load a roughly even $|a\rangle - |b\rangle$ Li spin mixture from the BFL into the combined 780 nm and 1064 nm trap, which are both trapping for Li. We do this by ramping up the powers in both beams while the BFL is overlapped with them using the translation

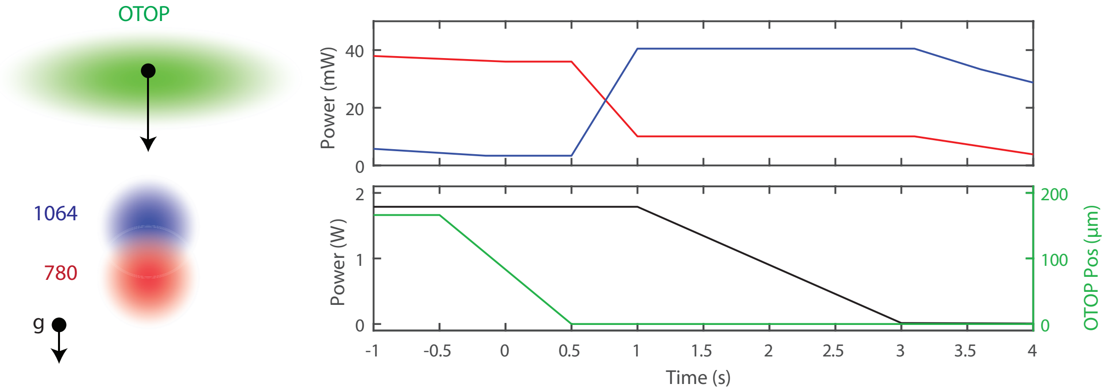

Figure 3.6: Dipole trap powers during final trap mixing. Diagrams showing the optimized beam powers for mixing the Li and Cs together. The upper plot shows the powers in the two dual color trap beams, with the 1064 nm trap shown in blue and the 780 nm trap shown in red. The lower trap shows the behavior of the OTOP beam, with the black line being the power and the green line being the position dictated by the modulation frequency of an AOM. The position 0 is the approximate position of the atomic cloud.

stage. After the BFL is ramped to zero using an AOM, we additionally translate the trap away to maximize extinction of the light at the atom position.

We then ramp the 1064 nm beam power close to zero, leaving the Li trapped almost entirely in the 780 nm beam. In this trap, the trap depth is lower than a D2 photon recoil, and we perform a “killing” pulse which cleanly eliminates the (usually) undesired $|b\rangle$ atoms from the trap. Once the Li is loaded into the 780 nm trap, we begin the process of adding Cs to the trap. We do this by moving the OTOP towards the dual color trap from above at a rate of about 190 μm/s over 1s. We stop the beam at a position where it is overlapped with the top edge of the 1064 nm focus, but separate from the 780 nm beam focus. This allows us bring in the OTOP beam for the trap transfer without significantly disturbing the Li already in the trap. We then lower the 780 nm and OTOP trap powers to mix both gases into primarily the 1064 nm beam. The final sympathetic cooling is then done by lowering the trap depth of the 780 nm beam to zero while lowering the trap depth of the 1064 nm beam to a target value to serve as our single beam science trap.

3.7 Microscopy and Potential Projection

By implementing a high resolution microscope objective, it is possible to image and probe the atomic samples at smaller length scales than previously possible. Additionally, the flexibility afforded by configurable optical potentials generated using a DMD is a valuable asset to future experiments. The majority of the initial testing and focusing of the microscope was done by G. Cai, and more technical details such as the alignment procedure, detailed optical set-up, and imaging scheme optimizations will be available in his thesis.

To perform high resolution microscopy, it is fundamentally important to collect a large fraction of the solid angle of light emitted from the object to be imaged. This is defined by the numerical aperture $\mathrm{NA} = \sin\theta$ where θ is the maximum half angle at which light can enter the objective. The attainable resolution is directly improved for larger NA. There are multiple ways to characterize resolution, but a commonly used metric is the Rayleigh criterion which is given by $r = 0.61\lambda/\mathrm{NA}$ where λ is the wavelength of the imaging light, either 852 nm for Cs or 671 nm for Li in our case.

Our objective is custom made by Special Optics, and is designed to give a magnification of 16.75 and a working distance of about 30 mm. It fits inside of the inner radius of the top coil. The accompanying tube lens creates an image on an Andor Ikon-M CCD, which is then read-out to an imaging computer for analysis. Additionally, in front of the CCD there is a filter to allow 670 nm and 852 nm light to transmit but block out room light and 1064 nm dipole trap scatter. The camera is capable of taking multiple images in a Fast-Kinetics configuration, which we are planning to use to take images of both Li and Cs *in situ* in a single experimental shot. For now we are operating it the standard full-frame read out mode.

The DMD is an evaluation board DMD (DLP3000) from Texas Instruments, which is connected via USB to our control computer. A 635 nm free-running diode laser is reflected off the micromirror face and demagnified before being projected down onto the atoms. The effective size of the DMD projection in the atom plane was chosen to permit the generation

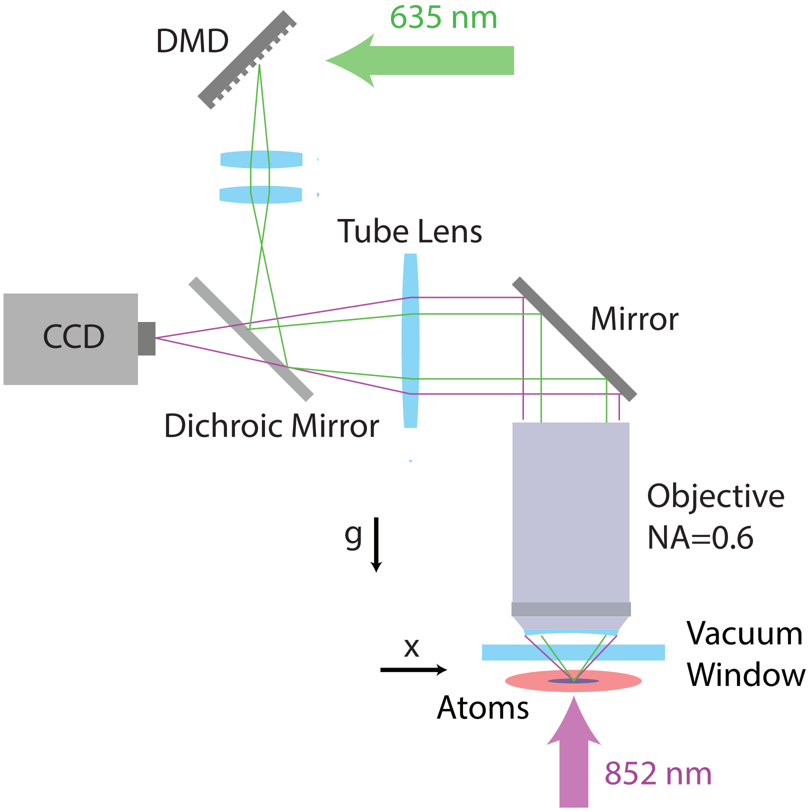

Figure 3.7: Overall schematic of optical potential projection and Cs BEC imaging. A high resolution microscope objective with numerical aperture NA=0.6 is positioned close to the atomic sample. Imaging light near 852 nm (purple arrow) is sent upwards through the objective, and is transmitted through a dichroic mirror and imaged onto a CCD. Light which is blue-detuned at 635 nm (green arrow) is reflected off a configurable digital micromirror device (DMD) before being reflected from the same dichroic and projected onto the atomic sample.

of optical potentials which can surround the typical degenerate Fermi gases we create.

We control the DMD by uploading images into its onboard memory, which can then be controlled via a computer over USB. This dictates which mirrors are on or off, while the overall brightness and therefore potential depth on the atoms is determined by the 635 nm laser power. Time dependent potentials can be generated using a trigger input on the DMD which allows the patterns to be changed, but at the time of this thesis this functionality has not yet been used on the atomic samples.

For Cs, at high field we often use the horizontal imaging to perform single-shot calibrations of the magnetic field based off microwave spectroscopy [34, 72]. In this type of measurement, we use microwaves to excite atoms from $|3,3\rangle \rightarrow |4,4\rangle$, which only excites atoms at two particular locations along the length of the cloud due to the curvature of the field. Then, we image the sample using the σ^+ transition from the side (with reduced cross section) and use the separation of the excitation peaks, the trap frequency, and the Breit-Rabi formula to extract the magnetic field. This type of spectroscopy can also be used to calibrate the effective pixels in the horizontal and vertical imaging, because the trap frequency and resonant microwave frequency fix the distance in terms of well known atomic properties.

Vertically, we can use this same excitation scheme to perform *in situ* imaging, without taking the cross section hit since we can properly address the σ^+ transition with a vertical beam. There are, however, two major draw-backs. The first is that the same sensitivity to magnetic field that makes the microwave transition useful for calibration can often be a nuisance when averaging experimental data, because field drifts of a few mG lead to significant number noise. Secondly, it is difficult to effectively couple $\sim$ 10 GHz radiation into our chamber with a conventional microwave horn, leading to a rather slow excitation. This is problematic both due to inelastic $|3,3\rangle - |4,4\rangle$ collisions and the large repulsive Cs $|4,4\rangle - |4,4\rangle$ interaction which excites the cloud [73]. Nonetheless, this scheme was used successfully for the work presented in Chapter 4 and 5, before we improved the imaging.

With the new and improved *in situ* imaging, to fully take advantage of the microscope it is important not to be limited by effects such as those mentioned above. So, we optically pump into state $|4,4\rangle$ instead of using microwaves. We use a 2 µs pulse generated from our Cs Repump laser to pump atoms from absolute ground state $|3,3\rangle$ into the stretched state $|4,4\rangle$ by addressing the $|3,3\rangle \rightarrow |3',3'\rangle$, where they mostly decay into $|4,4\rangle$. This transition is only MHz away from the low-field repump transition and is accessible just by tuning the diode laser current.

Additionally, to reach better resolution we enter the regime of high intensity absorption imaging. This has several advantages for imaging atomic clouds *in situ*, the most important being that it permits better signal at high densities and reduces unwanted effects from atomic motion induced by photon scattering. See Fig. 3.8 for a direct comparison of the old imaging performance to the upgraded system.

The column density n_2 is determined from the images according to the following equation:

$$n_2(x,y)\sigma = -\ln\frac{I_t(x,y)}{I_0(x,y)} + \frac{I_0(x,y) - I_t(x,y)}{I_s} \tag{3.2}$$

where σ and I_s do not exactly correspond to the calculated atomic values, and must be calibrated in the experiment. To be more concrete, an absorption image is taken by imaging an initial laser pulse which blows away the atoms (I_t) and a second image after they are gone (I_0). Finally, the electronic background is imaged with the light turned off, and subtracted from each of the previous two images. Comparing the images yields the column density as described in the equation above. In the limit of a weak imaging beam, as we typically employ for lower resolution imaging, the second term in Eq. (3.2) vanishes and the imaged density is independent of imaging intensity.

It is ideal to take the two images as close together as possible, as motion in the imaging beam can result in fringes in the atomic density image. For now, we actually take our images

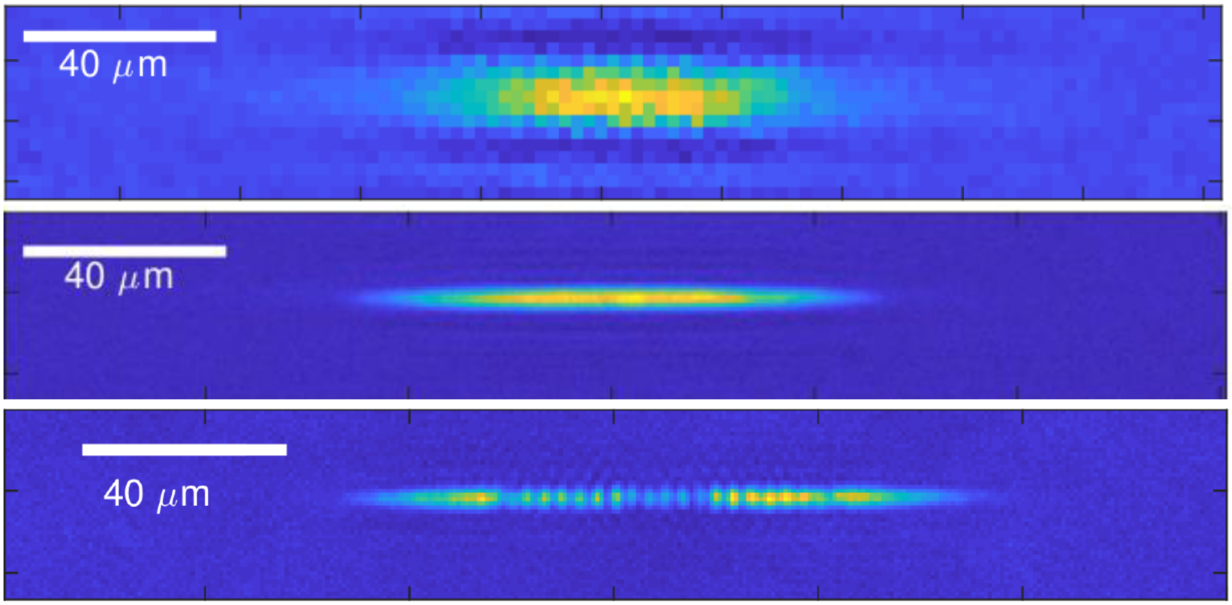

Figure 3.8: BEC imaging and potential projection sample images. Top: Old *in situ* image of a BEC at $a_{BB} \approx 200a_0$, with the imaging system used for the work described in Chapters 4 and 5. Middle: Image of the same system taken using the high resolution microscope (see text). Bottom: Sample image of same condensate after a projected stripe DMD pattern with 3.3 µm spacing has been turned on adiabatially.

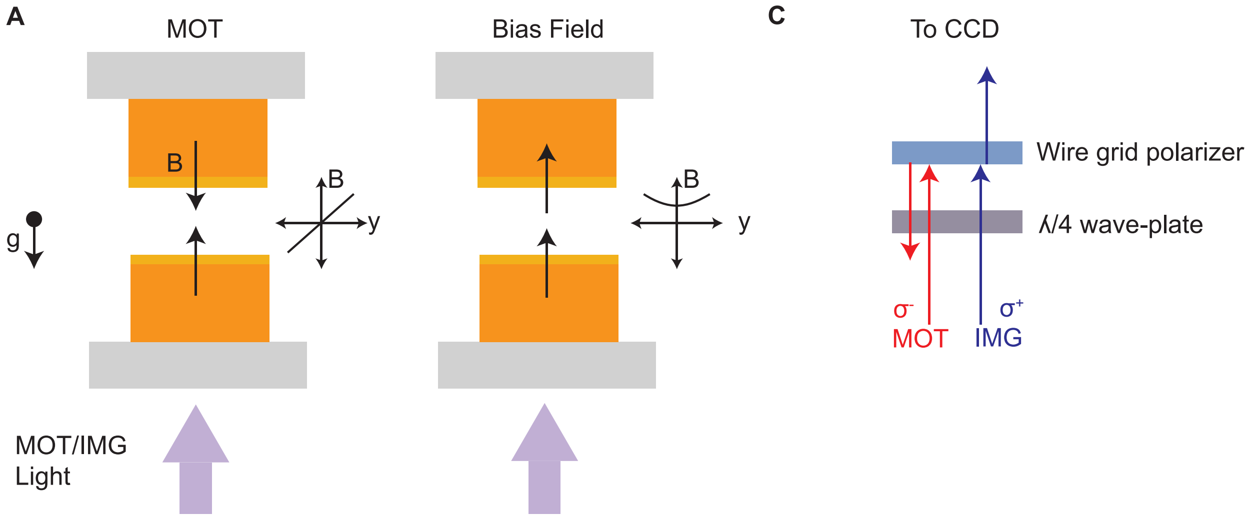

Figure 3.9: A) Cartoon showing the configuration of the main magnetic field coils during the MOT and during the high magnetic field portions of the experiment. Durinig the MOT phase, the currents point in opposite directions and the atoms are trapped at the magnetic field zero. At high field, the top coil current direction is flipped so that they are pointed in the same direction. The resulting field is much more uniform, with residual curvature that leads to a weak anti-trapping effect in y and trapping in x and z (<10 Hz for Cs). C) Just above the upper recessed viewport, a quarter wave plate and reflective polarizer in combination allow the MOT light to be reflected and the imaging light to pass through to a camera.

spaced 500 ms apart, which is quite long, but we find that there are actually very few fringes as long as we do not attempt to switch off the magnetic field during this time (which gives a significant and audible mechanical kick to the system). The largest source of fringes in our images originates from water-cooling of the main coils, which vibrates the experimental chamber.

The vertical imaging beam and the vertical MOT beam both enter the chamber from the bottom view port. However, it is necessary for the MOT light to be reflected with the correct handedness to provide confinement, while the imaging light must make it out of the chamber to a camera. This is done using two polarization optics which are placed on top of the top viewport, see Fig. 3.9. Note that these optics were taken into account in the custom design of the objective to ensure the desired performance.

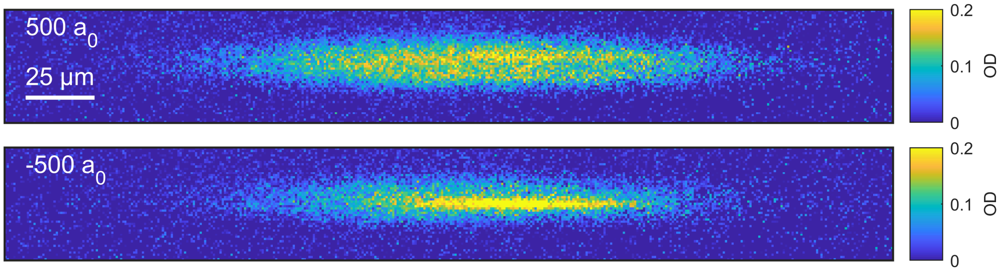

Figure 3.10: Sample Li *in situ* images. Shown are averaged images taken according to the imaging scheme described in the text. The upper image shows a depletion of the density due to repulsive interactions localized on the BEC, and the lower image shows an enhancement due to attraction.

The confinement in the MOT is obtained by keeping the polarization σ^- as defined by the local magnetic field direction. To understand this, consider that we are cooling using the 4→5' transition, so the excited stretched states exhibit larger Zeeman shifts than the ground stretched states. This means that, relatively, the σ^+ (σ^-) transitions are blue- (red-) detuned as the local field grows stronger. During the MOT, the laser light is red-detuned, so atoms moving away from the center will preferentially scatter light meeting them head on and be pushed back towards the center.

The imaging light is then σ^+ compared to the final bias field direction. For this type of scheme to work, the top coil must be switched so that it creates a field along the same direction as the bottom coil during the MOT, which in our case is opposite to gravity. The same structure with polarization optics exists along one of the horizontal MOT beam directions. We can image along the vertical direction, using our microscope, or with about 10x lower resolution at a 45 degree angle horizontally to the dipole traps.

In situ Li imaging

At high field, when the atoms are quantized along the direction opposite to gravity, the horizontal and vertical imaging behave differently due to atomic transition selection rules. For Li, we have historically imaged the gas horizontally on the σ^- transition using circularly polarized light. This leads to a factor of 4 reduction in the effective atomic cross section, since half the projection is along the quantization axis, and then another half is projected along σ^+. Before the work presented in Chapter 3, we modified the Li horizontal imaging beam path so that the light is linearly polarized, gaining a factor of 2 in signal. This additional SNR was very helpful for performing thermometry of the fermions, which relies on more careful analysis of the density profiles than boson thermometry (see Section 2.4).

Due to the polarization optics, this σ^- imaging transition would yield poor SNR along the vertical direction, because most of the light is reflected for the MOT. Instead, we want to target a σ^+ transition to maximize signal at the vertical CCD. We do so using a two-step process. First, we optically pump the atoms into $|f\rangle$ by allowing population to decay from the excited state manifold. Then, we image on the available σ^+ cycling transition out of $|f\rangle$.

To understand this pumping process, it is important to note that at 900 G the Li atoms are well into the Paschenbach regime, where the nuclear spin and electron spin are basically uncoupled and the appropriate quantum numbers are m_J and m_I, rather than F and m_F. In this regime, dipole transitions which couple to the motion of the electron do not flip the nuclear spin. In this notation, our typical Li state $|a\rangle = |m_J = -1/2, m_I = 1\rangle$ and $|f\rangle = |m_J = 1/2, m_I = 1\rangle$. To pump from $|a\rangle$ to $|f\rangle$, we excite the transition $|a\rangle \leftrightarrow |m'_J = 1/2, m'_I = 1\rangle$, which can only decay back down to $|a\rangle$ or $|f\rangle$, leading to pumping into $|f\rangle$, because these are the two states in the ground manifold with $m_I = 1$. We excite this transition using a sideband on the horizontal Li imaging path generated by passing the beam through an EOM before fiber coupling it to the experimental table. Then, the σ^+ transition that we cycle on to perform absorption imaging is $|f\rangle \leftrightarrow |m'_J = 3/2, m'_I = 1\rangle$, which belongs to the highest energy branch of the excited state. A similar scheme permits imaging atoms in $|b\rangle$, by instead driving $|b\rangle \leftrightarrow |m'_J = 3/2, m'_I = 0\rangle$ which pumps the sample into $|e\rangle$ permitting cycling on the σ^+ transition $|e\rangle \leftrightarrow |m'_J = 3/2, m'_I = 0\rangle$.

Work to optimize the resolution of the *in situ* vertical imaging of Li is currently ongoing at the time of this thesis, but the imaging is functioning. See Fig. 3.10 for images of Li overlapped with Cs which display modification of the density profile due to interspecies interactions.

Calibration of pixel sizes, cross-section, and saturation intensity

In this section, we discuss some of the experiments and analysis that we performed to calibrate aspects of the *in situ* imaging. We follow the overall strategy of Ref. [74]. We calibrated our pixels first, using microwave spectroscopy, then used the size of a Bose-Einstein condensate to calibrate the atom number. To calibrate the saturation intensity, we perform imaging pulses at varying intensities and compare the scattered photon number to the observed optical density (OD). The resulting slope can be used to extract the saturation intensity P_{sat} [74], according to

$$\text{OD} + \frac{\delta P}{P_{\text{sat}}} = n\sigma_0 = \text{const.}, \tag{3.3}$$

where δP is the CCD count difference between the atom and no atom shots. This allows the calibration of the saturation intensity in terms of CCD counts P_{sat} entirely from the behavior of the atoms.

The current calibration being used on the experiment is based off data shown in Fig. 3.11 which establishes that for a 5 µs imaging pulse, the saturation intensity corresponds to 355(21) counts at our CCD. This must be adjusted depending on the imaging pulse length. Typically we use 10 us pulse for science data, which we find only very slightly decreases our imaging resolution while yielding a large benefit in SNR.

To calibrate the pixel sizes for both horizontal and vertical images, we take advantage of

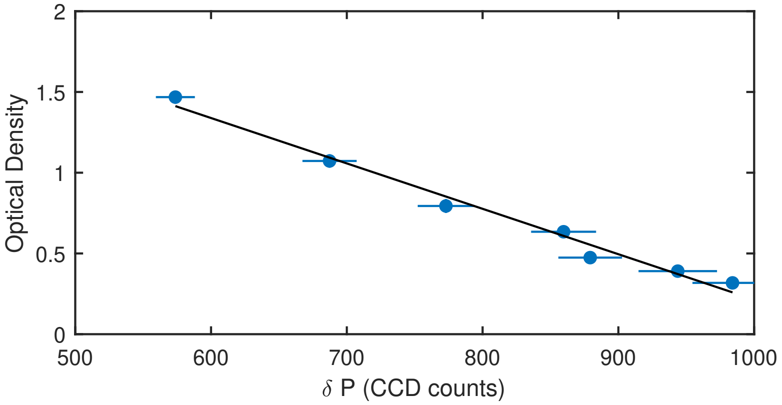

Figure 3.11: Calibration of saturation intensity. The optical density is compared to the number of missing counts that correspond to photons scattered by the atoms at different imaging powers. This permits calibration of P_{sat} (see text and Eq. (3.3)) and gives $P_{\text{sat}} = 355(21)$ for a 5 µs imaging pulse.

our single shot field calibration [34] and our high quality long axis dipole oscillations [36]. By measuring the separation between resonance peaks as a function of microwave frequency in terms of pixels, then comparing the result to the field curvature which produces the observed 6.65 Hz trapping frequency we are able to calibrate our pixel sizes.

We perform this calibration in a few hundred nK Cs thermal gas in the final science trap. It is necessary for the cloud to have sufficient extent to resolve multiple sets of resonance peaks at different microwave frequencies. We use the final trap so that it is in focus for the microscope, and we can directly perform this calibration looking at both the horizontal and vertical imaging, which will see the same excitation peaks. To be more specific, this calibration relies on the splittings of the $|3,3\rangle$ and $|4,4\rangle$ states in the ground manifold of Cs, which can be evaluated directly using the Breit-Rabi formula [64].

The Cs feels a potential energy $V(x) = \mu_{\text{Cs}} B(x)$ where μ_{Cs} is the magnetic moment of Cs in the absolute ground state, which near 900 G is a little bit different than the value in the Zeeman regime. The Breit-Rabi formula gives $\mu_{Cs}(900\text{G}) \approx 0.85\mu_B$, compared to $0.75\mu_B$ in the Zeeman limit, where μ_B is the Bohr magneton. Then, from the trap frequency we have that $6.65\,\text{Hz} = \frac{\omega_{B,x}}{2\pi} = \frac{1}{2\pi}\sqrt{\frac{2\mu_{\text{Cs}}}{m_B}(B(x) - B_c)}$ where B_c is the peak field value in the

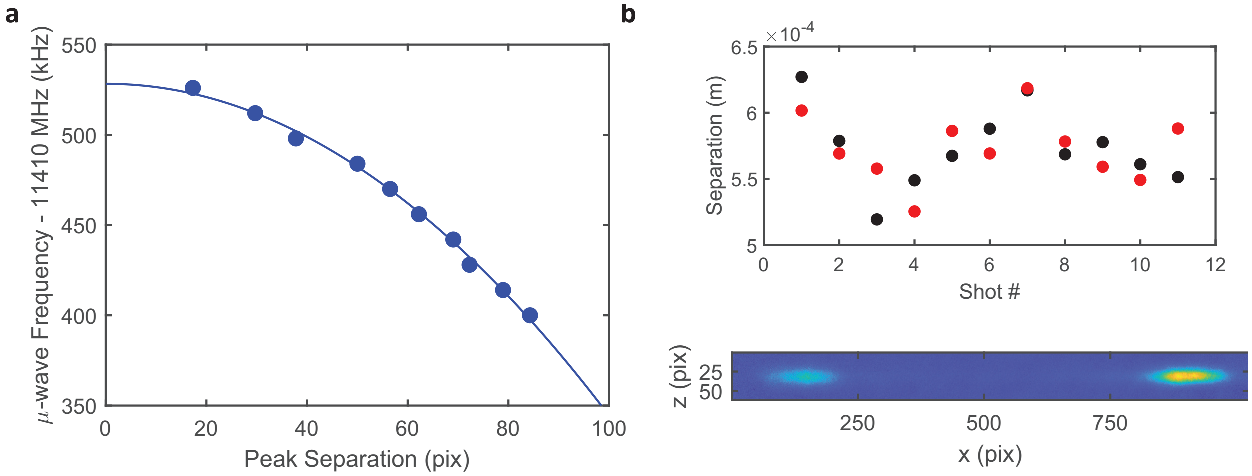

Figure 3.12: Camera pixel calibration. (a) Separation between the resonant portions of the cloud as the microwave frequency is changed (blue circles). A fit (blue line) is used to extract the pixel calibration 7.60(8) µm. This is consistent with the calibration obtained from measuring the center of mass in free fall under gravity. (b) Separation between resonant portions of the cloud as measured by alternating between horizontal (black circles) and vertical (red circles) imaging. The vertical separation has been scaled to match the horizontal separation. The shown image is a sample optical density image taken vertically from this type of data set. The vertical calibration obtained is 0.78(1) µm.

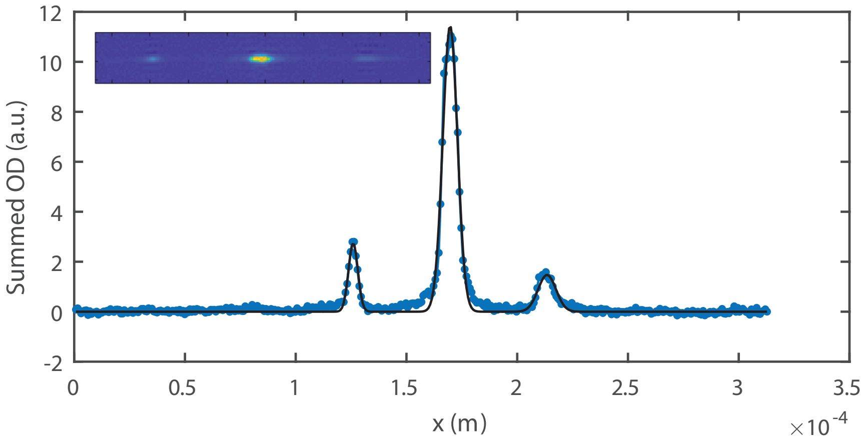

Figure 3.13: Calibration of DMD pixels. Column density (inset) and 1D density after diffraction from a 6 pixel on / 6 pixel off stripe pattern DMD illumination and a quarter period hold time in the weak axis confinement. The distance between the diffraction peaks is measured to be 87.5(2) µm using a fit containing three gaussian peaks (black solid line), which corresponds to a pixel size of 0.135 µm along the long direction (see text).

center of the trap. A fit to the peak separation as a function of microwave frequency then yields the pixel calibration, see Fig. 3.12. Once the horizontal pixels have been calibrated (7.60(8) µm, consistent with calibration from free-fall under gravity), the vertical pixels can be calibrated by creating the same density distribution and comparing them. We chose to use the same type of microwave excitation, fix the frequency, and alternate between horizontal and vertical shots. Then, the separation between the resonant peaks was scaled to be equal in the two cases, yielding the pixel calibration. The expected value based off the microscope and camera was 0.8 µm, and we measured 0.78(1) µm.

To calibrate the pixels of the DMD, we used the DMD to place a 50% duty cycle stripe pattern onto the condensate along the long axis, then turned it off and waited a quarter trap period to observe the position of the diffraction peaks. The momentum imparted is defined by $k_{\mathrm{DMD}} = \frac{2\pi}{\lambda}$ which allows us to calibrate λ based off our known trap frequency and therefore the DMD pixel size, see Fig. 3.13.

Finally, to calibrate the atomic cross-section, we used the size of the condensate in our *in situ* images. Due to the strong anisotropy of our trap, the kinetic energy can play a role in the

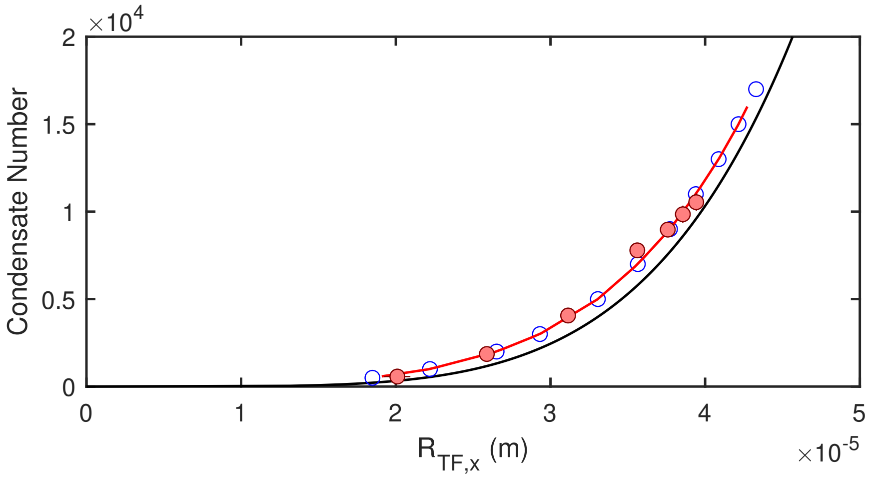

Figure 3.14: Cross-section calibration. To calibrate the atomic cross-section, we prepare condensates of varying number and measure their size. To calibrate the atomic cross section, we scale the number such that the sizes agree with ground state GPE calculations for the trap frequencies in the experiment. The black solid line is the Thomas-Fermi prediction, and the blue circles are the output of the GPE simulation. The red line is an interpolation of the simulated values, and the solid red circles are scaled experimental data. The atomic cross section $\sigma = 0.17(2)\sigma_0$, where $\sigma_0 = \frac{3\lambda^2}{2\pi}$ is the theoretical cross-section for the cycling transition.

observed size even for fairly large interaction energies. Therefore, to perform our calibration, we took a set of images of condensates prepared with different atom number at equilibrium in the same confinement at sufficiently low peak optical densities to permit accurate number counting. These atomic numbers were chosen by comparing the estimated atomic numbers for *in situ* data to samples that had undergone time of flight, and confirming that there was no discrepancy. Then, we performed imaginary time propagation to numerically simulate the ground state BEC density distrbution in our trap (see Appendix C) and scaled the measured atomic numbers to fit this prediction, see Fig. 3.14. After the calibration, we identify that our atom number counting appears accurate for peak densities below about 3×10^{13} cm^{-3}, but typical samples in our experiment have higher peak density. As a safe choice, 4 ms time of flight expansion is typically sufficient to accurately count the number for samples prepared near the Cs=$|a\rangle$ Feshbach resonance ($a_{\mathrm{BB}} \sim 250 - 290 a_0$).

CHAPTER 4

LI-CS AT QUANTUM DEGENERACY

Much fascinating science has been done studying few-body physics using this apparatus in the thermal regime, where the atoms are ultracold but their behavior was not yet dominated by quantum mechanical effects, their temperature $T \gg T_c$ for condensation. This chapter outlines the first scientific step taken in the Li-Cs lab from the few-body towards the many-body. We have created the first dual degenerate mixtures of Li and Cs atoms in our lab, and in this chapter we will describe our method to obtain degenerate samples, verify their degeneracy, and an initial study of their interactions. This chapter is reproduced from the following publication:

Brian DeSalvo, **Krutik Patel**, Jacob Johansen, and Cheng Chin. Observation of a degenerate fermi gas trapped by a bose-einstein condensate. Phys. Rev. Lett., 119:233401, 2017

Abstract: We report on the formation of a stable quantum degenerate mixture of fermionic ^{6}Li and bosonic ^{133}Cs in an optical trap by sympathetic cooling near an interspecies Feshbach resonance. New regimes of quantum degenerate Bose-Fermi mixtures are identified. With moderate attractive interspecies interactions, we show that a degenerate Fermi gas of Li can be fully confined in a Cs Bose-Einstein condensate without external potentials. For stronger attraction where mean-field collapse is expected, no such instability is observed. Potential mechanisms to explain this phenomenon are discussed.

4.1 Introduction

Mixtures of atomic quantum gases are an exciting platform to study a rich variety of physics, such as the observation of heteronuclear molecules [75–81], Bose and Fermi polarons [22–27], and superfluid mixtures[29–31]. Novel quantum phases have been suggested theoretically [16, 49, 82, 83] and probed experimentally [15, 17, 84, 85]. Intriguing quantum excitations [59–62], mediated long-range interactions [86, 87], and pairing behavior [88–90] are proposed based on degenerate Bose-Fermi mixtures.

An extensive review of previous work and specific mixtures used is found in Ref. [14]. To date, many experiments exploring quantum degenerate Bose-Fermi mixtures exhibit small to moderate mass imbalance [16, 83, 91–93]. For larger mass imbalance, new phenomena are expected to arise [31, 90, 94, 95]. Light fermionic ^{6}Li and heavy bosonic ^{133}Cs yields the largest mass imbalance among stable alkali atoms. This combination offers rich interaction properties that are well characterized [68, 96–99], and there exist interspecies Feshbach resonances at magnetic fields where both the Cs Bose-Einstein condensate (BEC) and Li Fermi gas are stable. This makes Li-Cs an excellent platform to investigate many-body physics of Bose-Femi mixtures.

Here, we explore two novel regimes of dual-degenerate Bose-Fermi mixtures accessed by this combination of atomic species by using the tunable interactions afforded by an interspecies Feshbach resonance. First, we find that for small attractive interactions, degenerate fermions are found fully trapped and confined by the Cs BEC. Second, at large attractive scattering lengths, we find the mixture is stable in the mean-field collapse regime [49].

4.2 Reaching Degeneracy

Our experimental procedure to prepare a quantum degenerate Bose-Fermi mixture follows. After initial laser cooling and optical trapping as described in Ref. [34], we obtain samples

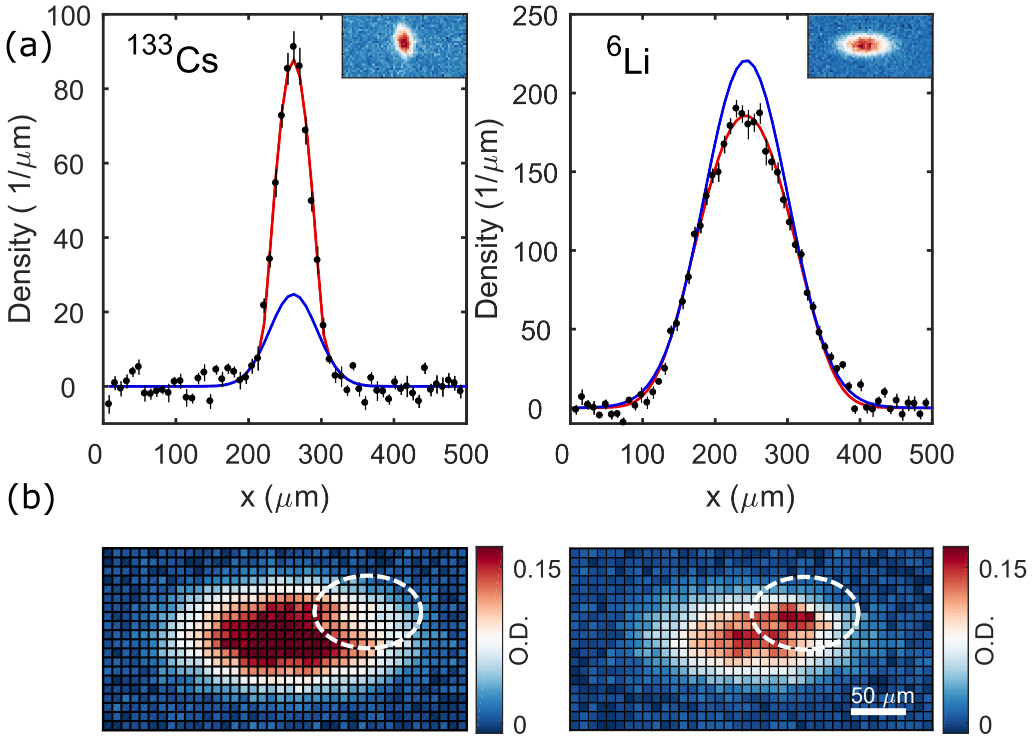

Figure 4.1: Simultaneous quantum degeneracy of ^{6}Li and ^{133}Cs. (a) Left panel: A bimodal distribution of a Cs BEC is visible after a 30 ms TOF expansion. The blue curve indicates the thermal fraction while the red curve shows a fit to the thermal and condensate fraction. Right panel: For Li, a Gaussian fit to the high momentum tail of the atoms after a 1.5 ms TOF overestimates the density at the center (blue curve). The full distribution is fit well using a polylogarithm function (red curve) with $T/T_F = 0.2(1)$ [38]. For repulsive interactions with $a_{BF} = 1000a_0$ (left panel (b)), the Li density is suppressed at the location of the Cs BEC after a 1.5 ms TOF. Conversely, the Li density in the same location is enhanced for attractive interactions with $a_{BF} = -580\ a_0$ (right panel (b)).

of 2×10^6 Li atoms in a deep translatable optical dipole trap, and 2×10^6 Cs atoms in a separate optical trap. At this point, we have a nearly equal spin mixture of Li atoms in the F=1/2 hyperfine manifold, referred to here as Li_a and Li_b, and Cs atoms spin-polarized into the $|F, m_F\rangle = |3, 3\rangle$ state, where F is the total angular momentum quantum number and m_F is the magnetic quantum number. We then ramp the magnetic field to 894.3 G. This corresponds to a scattering length for Cs of $a_{BB} = 290\ a_0$ and $a_{\mathrm{Li}_a-\mathrm{Li}_b} = -8\ 330\ a_0$ for Li, where a_0 is the Bohr radius. This yields efficient evaporative cooling for Cs and the spin mixture of Li. Both species are evaporatively cooled over 10 s to approximately 300 nK. We then remove Li_b with a resonant light pulse leaving only the absolute ground state of Li and Cs in the optical dipole trap.

These two species exhibit an interspecies Feshbach resonance at 892.64 G [68, 97, 99] that tunes the interaction between Li and Cs. Across the width of this resonance, the Cs-Cs scattering length varies slowly from $a_{BB} = 220 \sim 280\ a_0$. In this range, good evaporative cooling efficiency for Cs promises the ability to sympathetically cool Li_a atoms for suitable Li-Cs scattering length. To begin sympathetic cooling, we ramp the magnetic field to 891 G ($a_{BF} = 20\ a_0$) and sequentially load both species into a dual-color optical dipole trap comprised of 785 and 1064 nm light [34]. This trap allows the cancellation of the relative gravitational sag for Li and Cs and ensures good overlap between the species at low temperatures [34]. To prepare a mixture with attractive or repulsive interspecies interactions, once the samples are mixed we ramp the magnetic field over 10 ms to either 891.9 or 893.8 G, yielding an interspecies scattering length $a_{BF} = 120$ or $-180\ a_0$, respectively. We then perform evaporative cooling for 1.5 s to obtain degenerate samples.

Detection of quantum degeneracy is performed by analyzing time-of-flight (TOF) absorption images of both species. For Cs, after evaporation we obtain a BEC of 10^4 atoms with low thermal fraction at a temperature $T_{Cs} = 20$ nK, as shown in Fig. 4.1(a) left panel. For thermometry of Li, we first adiabatically ramp the interspecies scattering length over 25 ms to a small value ($|a_{BF}| < 30\ a_0$) so the Cs BEC does not influence the Li cloud. We then release the atoms and image the Li after 1.5 ms expansion, as shown in the right panel of Fig 4.1(a). We determine the Fermi temperature $T_F = 480(50)$ nK from the known trapping frequencies of $\omega_F = 2\pi \times (36, 430, 430)$ Hz, and $T/T_F = 0.2(1)$ from fitting the absorption images using a polylogarithm function [38]. From these fits, we observe that sympathetic cooling works well for attractive and repulsive interspecies interactions and both species reach deep quantum degeneracy on either side of resonance.

4.3 Trapping a Fermi gas with a BEC

In the presence of strong Li-Cs interaction, the density distribution of Li is distorted. Example images are shown in Fig. 4.1(b). Here, we shift the position of the Cs BEC to the edge of the Li cloud to gain visual clarity of the effect. For repulsive interactions (Fig 4.1(b) left panel), Li is repelled from the BEC. Conversely, for attractive interactions (Fig 4.1(b) right panel), Li atoms are attracted to the Cs BEC.

Per mean field theory, the potential experienced by one atomic species due to interspecies interactions is given by $2\pi\hbar^2 a_{BF}\left(\frac{1}{m_B} + \frac{1}{m_F}\right)n(\vec{r})$, where $m_{F(B)}$ is the mass of the fermion (boson), $\hbar$ is the reduced Planck's constant, and $n(\vec{r})$ is the density distribution of the other species. In our case, the density of the Cs BEC is over one order of magnitude larger than the Li degenerate Fermi gas, so the potential experienced by the Li is significantly greater. Given the typical density of a Cs BEC of $n_B = 5 \times 10^{13}\text{cm}^{-3}$, for $a_{BF} = -500\ a_0$ the trap depth in temperature units felt by Li is 450 nK. This large depth suggests that Li can be loaded into the Cs BEC even in the absence of another confining potential.

To investigate this possibility experimentally, we perform a Stern-Gerlach sequence to separate the Li atoms trapped by the Cs BEC from those that are not, as depicted in Fig. 4.2a. We first prepare a degenerate Bose-Fermi mixture in a single beam trap by performing our usual sequence and slowly ramping the intensity of the 785 nm beam to

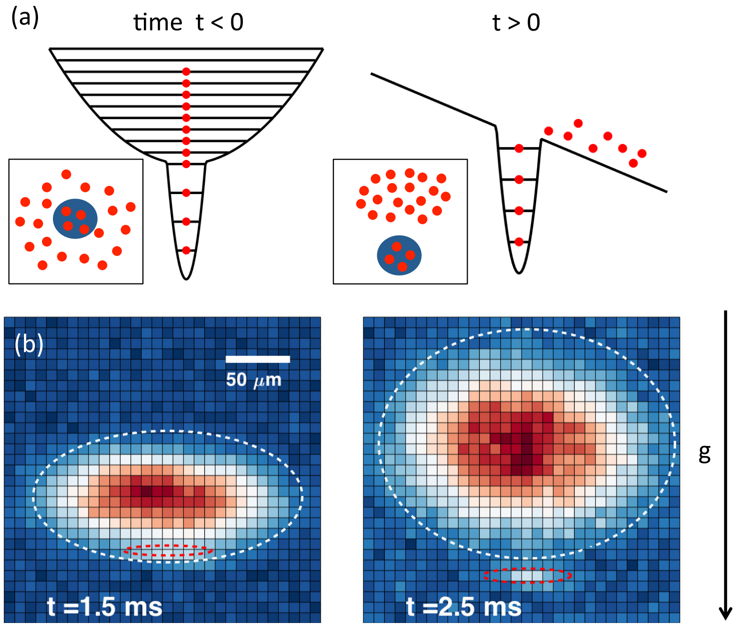

Figure 4.2: Stern-Gerlach separation of Li atoms trapped in a Cs BEC. Shown schematically in (a), strong attractive interspecies interactions confine a fraction of Li atoms (red dots) within the Cs BEC (blue circle). At $t = 0$ we remove the optical trap and apply a magnetic field gradient to separate those trapped from the rest of the sample. Example images of Li after a short TOF are shown in (b). Dashed red circles indicate the position and size of the BEC at the imaging time and the white dashed line indicates the Fermi radius.

zero. In this simplified configuration, the overlap of the two species is controlled by the magnetic field gradient, and we obtain trap frequencies of $\omega_B = 2\pi \times (6.5, 130, 160)$ Hz for Cs and $\omega_F = 2\pi \times (36, 400, 400)$ Hz for Li. Next, we ramp the magnetic field gradient to 4 G/cm providing a force against gravity and simultaneously increase the interaction strength to -650a_0 over 30 ms. This deepens the potential so a reasonable number of Li are trapped and shifts the Li up such that the Cs BEC sits on the lower edge of the Li cloud. We then extinguish the optical trap while leaving the magnetic field and gradient on. The magnetic field gradient is sufficient to over-levitate Li, but not the Cs atoms. Therefore, Li atoms trapped by Cs BEC fall downwards.

Results of this experiment are shown in the absorption images of Li after a varying TOF, see Fig. 4.2 (b). In each image, the white dashed curve shows the maximum extent of the cloud from the calculated Fermi radius and the red dashed curve shows the position and spatial extent of the Cs BEC. After a TOF, Li atoms trapped in the Cs BEC spatially separate from the rest of the sample. These Li atoms are contained in the volume of the Cs BEC and follow its trajectory over the entire TOF. Once spatially separated, Li atoms trapped in the Cs BEC can be counted. By following the previously described Stern-Gerlach procedure at different magnetic field values we measure the number of Li atoms trapped by the Cs BEC as a function of a_{BF} as shown in Fig. 4.3.

Owing to the Pauli exclusion principle, there is a limited number of Li atoms $N < N_{max}$ that can be trapped within the Cs BEC. Assuming the density of the BEC is not perturbed by Li atoms, the maximum number N_{max} can be found analytically. Within the mean-field and Thomas-Fermi approximations, the density distribution of the BEC is an inverted parabola, yielding a harmonic trap for Li with trap depth $U_0 = \frac{1}{2}(\frac{m_B}{m_F} + 1)\frac{|a_{BF}|}{a_{BB}}\mu$ and trapping frequency $\omega_{trap} = [\frac{1}{2}\frac{m_B}{m_F}(\frac{m_B}{m_F} + 1)\frac{|a_{BF}|}{a_{BB}}]^{1/2}\omega_B$, where ω_B is the trapping frequency for Cs and μ is its chemical potential. Notably the trap frequency for Li ω_F is 16 times larger than the trap frequency for Cs due to mass imbalance alone. Therefore, the dynamics

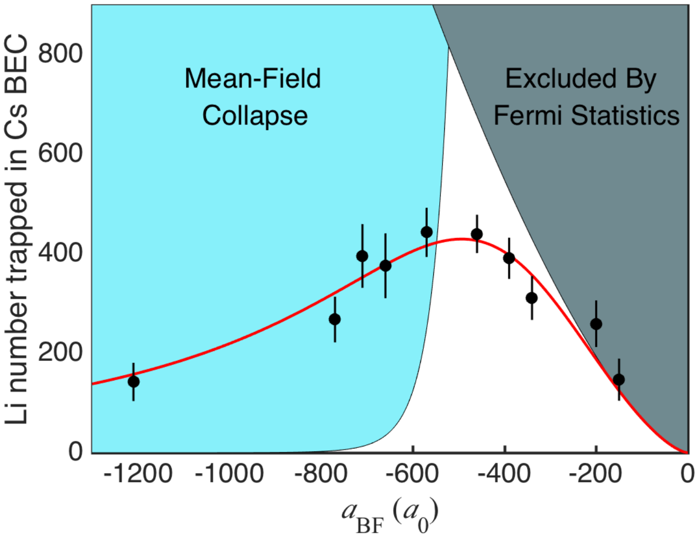

Figure 4.3: Number of Li atoms trapped in Cs BEC. As a function of the interspecies scattering length a_{BF} at the end of the magnetic field ramp, we measure the number of Li atoms trapped in the Cs BEC after a 1.5 ms Stern-Gerlach separation (black dots). Within the approximation described in the text, the grey shaded region represents the the region excluded by Fermi statistics and the blue shaded area indicates the region where mean-field collapse is expected. The red curve shows a fit based on a rate equation model describing the steady-state number of atoms trapped by the Cs BEC (see text).

of Li in the Cs BEC are much faster than the condensate itself.

By setting the Fermi energy equal to the trap depth, one finds that for $a_{BF} < 0$ the maximum number of Li trapped by the Cs BEC is

$$N_{max} = \frac{1}{12\sqrt{2}}\left[\left(1+\frac{m_F}{m_B}\right)\frac{|a_{BF}|}{a_{BB}}\right]^{3/2}\left(\frac{\mu}{\hbar\omega_B}\right)^3. \tag{4.1}$$

This limit is indicated by the grey shaded region in Fig. 4.3 and is consistent with our measurement for $|a_{BF}| < 400\ a_0$. For these weak interactions, since the number of Li trapped is close to the maximum, the Li remains deeply quantum degenerate.

4.4 Mean-Field Collapse?

For a large negative scattering length, mean-field calculations predict another limit on the number of Li atoms that can be trapped by the Cs BEC. When the Li density exceeds a critical value n_{crit}, theory predicts a collapse of the mixture due to the loss of mechanical stability. For a homogenous gas, the critical density is [49]

$$n_{crit} = \frac{4\pi}{3} \frac{m_B^3 m_F^3}{(m_B + m_F)^6} \frac{a_{BB}^3}{a_{BF}^6}. \tag{4.2}$$

The condition for collapse in a trapped gas is found following the numerical procedure described in Ref. [49]. We find that the system collapses when the peak density of the fermions exceeds the critical density given in Eq. 4.2. This limit sets the lower boundary of the shaded blue region in Fig. 4.3. Shown in Fig. 4.3 as well as observed in other experiments including a longer hold time, for large negative scattering lengths a_{BF} we find significantly more Li atoms trapped in the Cs BEC than permitted by mean-field theory.

One possible explanation for the lack of mean-field collapse is beyond mean-field terms similar to the Lee-Huang-Yang term for bosons [100]. Observed in dipolar quantum gases [101], this effect leads to a short-range repulsion and stabilizes a collapsing BEC with dipolar interactions, and likely a Bose-Bose mixture with strong interspecies attraction [44]. The scenario to stabilize an attractive Bose-Fermi mixture with beyond mean-field effects [102] requires further theoretical investigation.

In our system, another possible explanation for the lack of mean-field collapse is a dynamical process including three-body loss and Fermi statistics. The association of higher particle number with collisional loss seems counterintuitive, but the strong density dependence of three-body collisions is key to removing atoms preferentially from the high-density region and preventing mean-field collapse.

To explore this possibility, we suggest the following model. Since the dynamical timescale for Li is much shorter than for Cs, we describe the density of Li atoms trapped in the Cs BEC as

$$\frac{dn}{dt} = Aa_{BF}^2 n_F n_B f - Ba_{BF}^4 n_B^2 n, \tag{4.3}$$

where A and B are constants, n_B is the density of the Cs BEC, n is the density of Li confined in the BEC, and n_F is the density of unconfined Li. The first term accounts for elastic collisions that populate available states in the BEC potential with probability $f \approx 1 - N/N_{max}$ given by Fermi statistics. The second term represents three-body loss due to Li-Cs-Cs collisions [103].

Due to the small number of Li atoms trapped in the Cs BEC and the large separation in dynamical timescales between the two species, we assume that the BEC density profile and Cs number are not disturbed in the time the Li density profile reaches steady-state. Averaging Eq. (4.3) over the extent of the Cs BEC, we obtain $d\bar{n}/dt = A' a_{BF}^2 \bar{n}_B \bar{n}_F f - B' a_{BF}^4 \bar{n}_B^2 \bar{n}$, where $\bar{x}$ is the averaged value of x, and A' and B' are constants incorporating geometric factors from averaging.

In steady-state $d\bar{n}/dt = 0$, we obtain $N = N_{max}/(1+Ca_{BF}^2 N_{max})$, where C is a constant. Combining this expression with Eq. (4.1), we fit our data in Fig. 4.3 with C as the only fitting parameter. The result yields good agreement. In the case of no collisional loss $B' = 0$, the fit function reproduces the limit where a deeply degenerate Fermi gas of N_{max} Li atoms is supported by the BEC.

In this picture, for large negative scattering length, Li atoms are quickly lost through recombination. Since this process is the highest at the center of the BEC, the loss of Li atoms prevents the runaway density build up at the trap center. Similar loss of Cs atoms occurs predominately at the trap center. However, the loss of Cs is slowed by the limited rate at which its volume is replenished with fermions from the surrounding Fermi gas.

In Fig. 4.4, we show the evolution dynamics of a Cs BEC immersed in the Li degenerate Fermi gas. Here, we first create a degenerate mixture in the single beam dipole trap. After

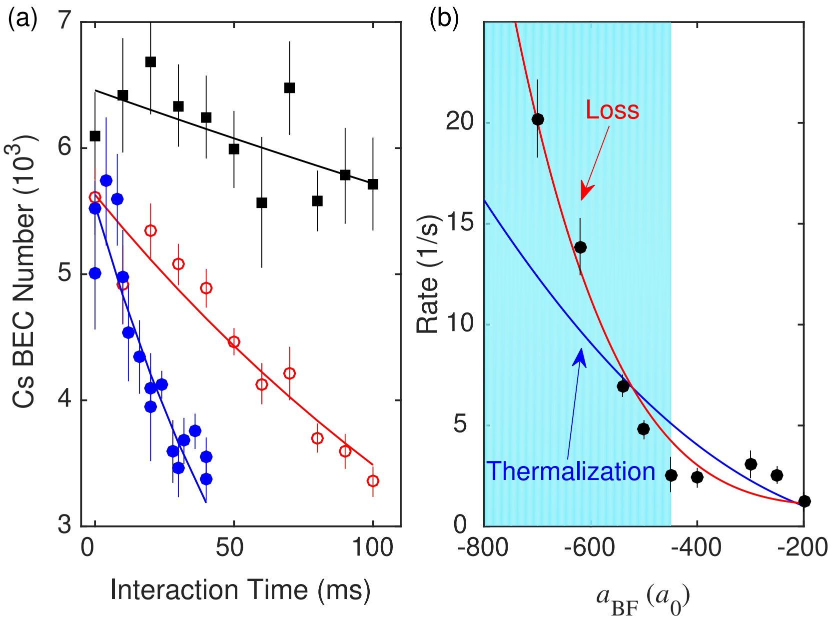

Figure 4.4: Loss dynamics of Cs BEC immersed in Li degenerate Fermi gas. (a) Atom number in Cs BEC for a_{BF} = -200 (black), -500 (red), and -620 a_0 (blue). The data is well described by smooth exponential loss (solid lines). The $1/e$ loss rates extracted from these fits shown in panel (b) are well fit by the expected a_{BF}^4 scaling including a constant offset in the loss rate to account for measured Cs-Cs-Cs recombination (red line). An estimation of the thermalization rate (see text) is indicated by the solid blue curve. The loss rate exceeds the thermalization rate at $a_{BF} = -520a_0$, above which the system no longer reaches thermal equilibrium.

quickly ramping the magnetic field to a desired value, we measure the number of Cs atoms in the condensate after a TOF. The atom number in the BEC smoothly decays with a loss rate proportional to a_{BF}^4 as expected [104]. No dramatic drop in atom number associated with collapse is observed.

Mean-field calculations assume that the system thermalizes quickly enough to reach equilibrium. However, thermalization is known to be slow for systems with large mass imbalance. Unlike atoms must undergo $\xi = 3(m_B + m_F)^2/(4m_B m_F)$ collisions to thermalize [105]. An estimation of the collision rate between degenerate Bose and Fermi gases is in general complicated, and we employ a model for thermal gases that offers an upper bound on the collision rate given by $\gamma = 4\pi a_{BF}^2 \bar{v} \int d^3r n'_F(\vec{r}) n_B(\vec{r})$, where $n'_F(\vec{r})$ is the density of fermions available for collisions and the averaged relative velocity of Li and Cs atoms is given by $\bar{v} \approx \sqrt{2E_F/m_F}$

in our experiment. Combining the above results with the fermion density's slow variation across the BEC, we obtain the thermalization rate $\Gamma = \frac{N_F'+N_B}{N_F' N_B}\frac{\gamma}{\xi}$ [106] as

$$\Gamma \approx 3.74 \frac{m_B m_F^2}{(m_B+m_F)^2} \frac{(N_B+N_F')}{N_F'^{1/3}} \frac{a_{BF}^2 \bar{\omega}_F^2}{\hbar}, \tag{4.4}$$

where $\bar{\omega}_F$ is the geometric mean of the trap frequencies of the fermions, N_B is the number of bosons and N_F' is the the number of fermions participating in collisions. Using $N_F' \approx g(E_F)k_B T = 3N_F(T/T_F)$ where $g(\epsilon)$ is the single particle density of states we obtain the thermalization rate, shown in Fig 4.4(b).

At large scattering lengths $|a_{BF}| > 520a_0$, the loss rate exceeds the thermalization rate, suggesting the mixture will deviate from thermal equilibrium. Notably, the dominance of inelastic loss is more likely to occur in a Li-Cs system due to its strong mass imbalance. In comparison to the ^{40}K-^{87}Rb mixture in Refs. [16, 83] where mean-field collapse was reported, our thermalization rate is two times lower (from Eq. (4.4)), while the three-body collision rate increases by a factor of two [104] for the same trap frequency and atom numbers. Consequently, our system with large attractive Li-Cs interactions likely reaches a dynamical equilibrium where fast loss allows the mixture to survive for much longer than the mean-field expectation.

In conclusion, we report the first quantum degenerate mixture of Li and Cs and use this system to probe novel regimes of Bose-Fermi mixtures. For weak attractive interactions, a degenerate Fermi gas with few hundred Li atoms is confined within the BEC. This represents an intriguing quantum object well-suited for future study. For strong attractive interactions, we observe that the system is stable against mean-field collapse. We present one possible model to explain this observation based on the relative timescales of loss and thermalization. Other possible explanations involving beyond mean-field effects are under investigation. The lack of the mean-field collapse in our system allows us to explore a region of the Bose-Fermi mixture that was previously thought inaccessible.

CHAPTER 5

FERMION-MEDIATED INTERACTIONS BETWEEN BOSONS

After establishing degeneracy in our mixtures, we sought to look for signs of fermion mediated interactions which had been a long term goal of our experiment. They arise as outlined in Section 2.5, and have been long-predicted in the literature. However, their direct confirmation had never been reported. This chapter describes our measurement of these interactions, and is reproduced from the following publication:

Brian DeSalvo*, **Krutik Patel***, Geyue Cai, and Cheng Chin. Observation of fermion-mediated interactions between bosonic atoms. Nature, 568:61–64, 2019. *These authors contributed equally.

Abstract: In high energy and condensed matter physics, particle exchange plays an essential role in the understanding of long-range interactions and correlations. For example, the exchange of massive bosons leads to the Yukawa potential [107, 108]. Phonon exchange between electrons gives rise to Cooper pairing in superconductors [109]. When a Bose-Einstein condensate (BEC) of cesium atoms is embedded in a degenerate Fermi gas of lithium atoms, we show that interspecies interactions can give rise to an effective trapping potential, damping, and attractive boson-boson interactions mediated by fermions. The latter, related to the Ruderman-Kittel-Kasuya-Yosida (RKKY) mechanism [110], results from a coherent three-body scattering process. Such mediated interactions are expected to form novel magnetic phases [87] and supersolids [111]. We show that for suitable conditions, the mediated interactions can convert a stable BEC into a train of “Bose-Fermi solitons” [59, 61]. The predicted long-range nature of the mediated interactions opens up the possibility of correlating distant atoms and preparing new quantum phases.

5.1 Introduction

Interactions between cold neutral atoms are typically well-approximated by contact interactions and are characterized by a single parameter, the scattering length a. Recent experiments utilizing highly magnetic atoms [112], Rydberg atoms [113], and ground-state polar molecules [76], have stimulated great interest to probe novel quantum many-body states with long-range interactions. Examples include quantum droplets [101, 114] and lattice spin phases [115–117].

Another class of many-body systems that exhibit long-range interactions are quantum mixtures in which particle interactions are mediated by interspecies scattering. Here, we consider the case of interactions between bosons mediated by a degenerate Fermi gas. In the regime that the dynamics of the fermions are much faster than those of the bosons, an effective description for the bosons applies. In this case, the mediated interactions are a spinless analog [87, 118] of RKKY interactions [110],

$$U(R) \propto -g_{BF}^2 \frac{\sin R - R\cos R}{R^4}, \tag{5.1}$$

where $R = 2k_F R_B$, k_F is the Fermi wavevector, R_B is the separation between bosons, $g_{BF} = 2\pi\hbar^2 a_{BF}(\frac{1}{m_B} + \frac{1}{m_F})$ is the interspecies interaction strength, a_{BF} is the interspecies scattering length, $m_{B(F)}$ is the boson (fermion) mass, and $\hbar$ is the reduced Planck's constant. The interaction is attractive at short distance regardless of the sign of g_{BF}, and is oscillatory at long-range with the length scale of π/k_F, which corresponds to 1 μm in our experiment.

In this work, we demonstrate the effect of boson-boson interactions mediated by fermions in a degenerate Fermi gas. By using a mixture of fermionic ^{6}Li and bosonic ^{133}Cs, our system offers the tunability needed to observe the effect of such interactions, ultimately leading to the formation of a Bose-Fermi soliton train. In our system, the combination of light fermions and heavy bosons with their associated large Fermi energy $E_F = \frac{\hbar^2 k_F^2}{2m_F}$ and small BEC chemical

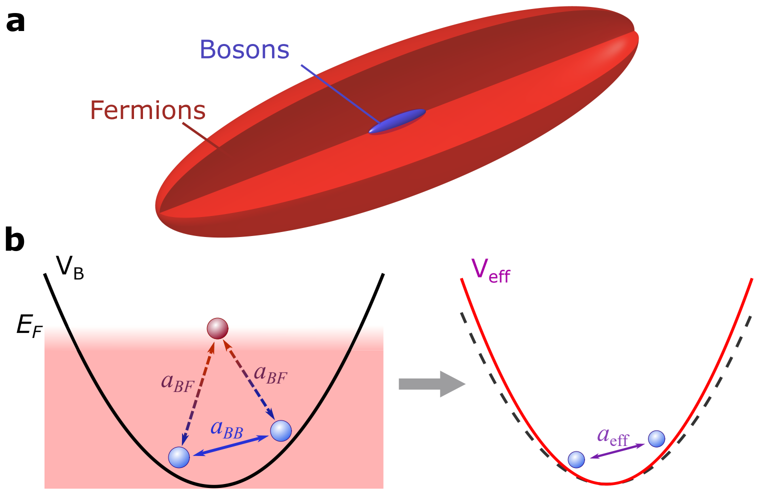

Figure 5.1: Mediated interactions between bosonic atoms by exchanging fermionic atoms in a Fermi sea. **a** A Bose-Einstein condensate of heavy atoms (blue) is fully immersed in a degenerate Fermi gas of light atoms (red). **b** Two bosons (blue balls) can interact with one another directly with scattering length a_{BB} or via secondary interactions with fermions (red ball) near the Fermi surface with energy E_F. By eliminating the fermionic degrees of freedom, the bosons can be described by an effective trapping potential $V_{\rm eff}$ and with modified interactions characterized by an effective scattering length $a_{\rm eff}$ (see text).

potential μ_B ensures a large separation of the relevant timescales ($\hbar/E_F \approx 15\ \mu s$ for fermions and $\hbar/\mu_B \approx 500\ \mu s$ for bosons). Furthermore, the large mass imbalance and difference in quantum statistics allows us to prepare a BEC that is fully immersed in the degenerate Fermi gas, as shown schematically in Fig. 5.1a. For zero interspecies interactions, the density of the fermions within the BEC is nearly constant. For weak interactions, one may eliminate the fermionic degrees of freedom and obtain an effective energy density functional of the bosonic field $\Psi_B(r)$, given by [119–121]

$$E = \frac{\hbar^2}{2m_B}|\nabla\psi_B(r)|^2 + V_{\rm eff}(r)|\psi_B(r)|^2 + \frac{g_{\rm eff}}{2}|\psi_B(r)|^4, \tag{5.2}$$

where $V_{\rm eff}(r) = \sum_i \frac{1}{2} m_B \omega_{{\rm eff},i}^2 r_i^2$ is the effective potential and $r_i = x, y, z$. The effective harmonic trapping frequencies $\omega_{{\rm eff},i}$ and the effective interaction strength $g_{\rm eff} = 4\pi\hbar^2 a_{\rm eff}/m_B$

satisfy the relations [119, 120]

$$\omega_{\mathrm{eff},i}^2 = \omega_{B,i}^2 - \frac{3}{2}\frac{n_F}{E_F}\frac{m_F}{m_B} g_{BF}\omega_{F,i}^2 \tag{5.3}$$

$$g_{\mathrm{eff}} = g_{BB} - \xi\frac{3}{2}\frac{n_F}{E_F} g_{BF}^2, \tag{5.4}$$

where $n_F = k_F^3/6\pi^2$ is the density of the fermions, $\omega_{B(F),i}$ denote the bare harmonic trapping frequencies of the bosons (fermions), and $g_{BB} = 4\pi\hbar^2 a_{BB}/m_B$ is the boson-boson interaction strength for scattering length a_{BB}. We note that owing to the large mass imbalance and large Fermi energy in our system, Eq. (5.3) is well approximated by a linear dependence of ω_{eff} on a_{BF} for all scattering lengths probed in our experiment.

The dimensionless constant ξ in Eq. (5.4) characterizes the strength of the fermion-mediated interaction. A calculation which takes a mean-field approach for the bosons and a hydrodynamic approach for the fermions predicts $\xi = 1$ for the mixture in the ground state [119]. The same result is also obtained based on a path integral formulation which traces out the fermionic degrees of freedom [120], as well as a diagrammatic calculation of the zero-temperature equation of state [121]. An alternative approach based on scattering of two-bosons embedded in a zero-temperature degenerate Fermi gas predicts $\xi = \pi^3 \approx 31$ [87]. We note that this last prediction includes the assumption that the interparticle separation between bosons is much larger than between fermions.

From Eqs. (5.2-5.4), it is apparent that the presence of the Li degenerate Fermi gas is expected to alter the dynamics of the Cs BEC in two important ways. The BEC will experience both a modified harmonic trapping force as well as a modified scattering length a_{eff}. The former effect can be understood in the mean-field picture. As the degenerate Fermi gas is also trapped in a harmonic potential, the spatially dependent density yields a mean-field potential on the BEC. For attractive (repulsive) interactions, the BEC experiences a stronger (weaker) harmonic confinement.

The mediated interaction, described by the second term of Eq. (5.4), is a genuine three-body scattering effect with an energy $E \propto -g_{BF}^2 n_B^2 n_F$, where n_B is the density of the bosons. A microscopic picture giving rise to these mediated interactions is sketched in Fig. 5.1b. They arise when two bosons exchange a fermion near the Fermi surface via the usual two-body s-wave scattering (dashed lines). We note here that the mediated interactions are always attractive regardless of the sign of g_{BF}. This fact can be understood as a result of second-order perturbation theory that the interspecies coupling lowers the energy of the condensate [87]. An intuitive picture allows this be understood in the mean-field description as follows: For repulsive interspecies interactions, fermions are repelled from the BEC, and thus the BEC feels an additional attraction towards its center where the fermion density is the lowest. On the other hand, for attractive interspecies interactions, fermions are attracted to the center of the BEC, and as a result the BEC also experiences an additional attraction towards its center where the fermion density is the highest.

To observe the effective trapping frequency as well as the mediated interactions, we perform measurements at different scattering lengths a_{BB} and a_{BF} near intra- and interspecies Feshbach resonances [67, 68] (see Methods). In our system, following the procedure outlined in Refs. [97, 122], we prepare quantum degenerate mixtures of 2×10^4 Li and 3×10^4 Cs atoms in their absolute ground state at magnetic field $B \approx 900$ G. Both species are radially trapped in a single laser beam and weakly confined magnetically in the $x-$direction.

5.2 Dipole Oscillation Measurements

To measure the effective harmonic trapping frequency, we excite dipole oscillations of the Cs BEC along the weakly trapped axis [30, 123, 124]. In the absence of Li, we observe long-lived oscillations with a decay time of ≈ 30 s (see Fig. 5.2a). This low background damping rate allows us to precisely determine the trapping frequency of the Cs (see Methods).

In the presence of Li, we observe small shifts in the oscillation frequency ω_{eff} and enhanced

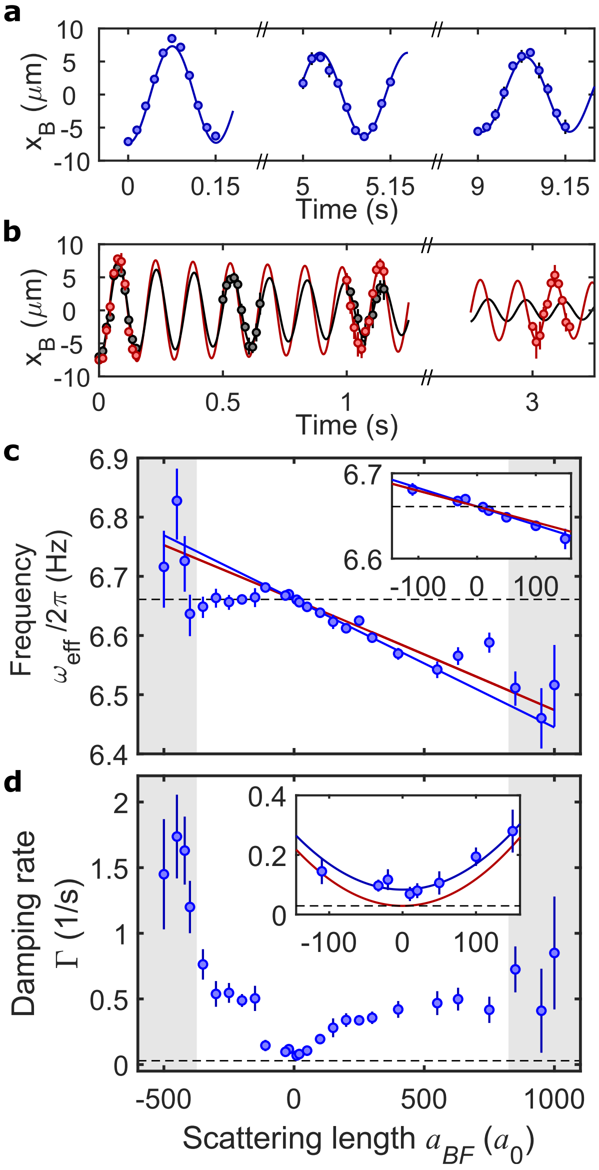

Figure 5.2: Dipole oscillations of a Cs BEC immersed in a Li degenerate Fermi gas. **a** Without Li present, we observe long-lived dipole oscillations along the weakly confined $x-$axis. The data is well described by damped harmonic oscillation with a very low damping rate $\Gamma < 1/30\ s$ (blue line). **b** When the BEC is embedded in the Fermi gas, a shift in the oscillation frequency as well as an increase of the damping rate are observed. Example traces are shown for $a_{BF} = 100\ a_0$ (red) and $a_{BF} = 630\ a_0$ (black). **c** Oscillation frequency and **d** damping rate of the BEC. For small $|a_{BF}|$,, the data are well fit by linear and quadratic curves (blue lines) and are consistent with the predictions (red lines), see Eq. (5.3,5.4) and Methods. Shaded areas show the magnetic field ranges where rapid three-body loss causes significant heating of the BEC into a normal gas. Frequency and damping rate of a bare Cs BEC (dashed lines) serve as references for comparison.

damping rates Γ as a_{BF} deviates from zero (see Fig. 5.2b). In the range of $-100\ a_0 < a_{BF} < 500\ a_0$, we observe a linear dependence of the frequency of the oscillation on the scattering length a_{BF} (see Fig. 5.2c). A fit to the data in this range shows a negligible shift $<\ 0.1\%$ at $a_{BF} = 0$ and a slope of $-\ 0.22(2)$ mHz/a_0, in fair agreement with the prediction of -0.18 mHz/a_0 from Eq. (5.3) . Outside this range, a non-linear behavior develops and the frequency shifts first reduce toward the bare Cs frequency. In this region of moderate $|a_{BF}|$, the dynamics are complicated by the crossover from collisionless to hydrodynamic motion [125] as well as modifications of the density distributions. For very large $|a_{BF}|$, the mixture is strongly heated due to three-body recombination loss that preferentially removes atoms from the BEC compared to the thermal component. In this region (see shaded area in Figs. 5.2c and d), we observe that the BEC is heated to a normal gas and the data display even larger shifts. Such non-linear behavior at large a_{BF} shows the breakdown of the mean-field theory and demands further theoretical investigation.

The damping of dipole oscillations shows interesting behavior as well. For small scattering lengths, collisions between the BEC and the Fermi gas are scarce, yielding a weak friction that damps the oscillation. The damping rate is expected to be proportional to the collisional cross-section $\propto a_{BF}^2$ [51, 126]. In the range of $-100\ a_0 < a_{BF} < 100\ a_0$, our data can be compared with the prediction $\Gamma = \kappa a_{BF}^2$ (see inset of Fig. 5.2d and Methods). A fit to the data in this range yields a curvature of $\kappa = 8.5(2.1) \times 10^{-6}/s \cdot a_0^2$, which excellently agrees with the prediction of $\kappa = 9 \times 10^{-6}/s \cdot a_0^2$. At large scattering lengths, the damping rate appears to saturate and then increases again when the sample is heated to a normal gas. While a more complete model is needed to describe the motion of a BEC strongly interacting with a degenerate Fermi gas, we note that for small scattering lengths ($|a_{BF}| < 100\ a_0$), the mean-field theory offers very good quantitative agreement.

5.3 Effective Attraction Induced by Fermions

To measure the mediated interactions, we first characterize the bare scattering length of the Cs atoms based on the equilibrium Thomas-Fermi radius $R_{TF} \propto \frac{1}{\omega_x}(N_0 a_{BB})^{1/5}$ in the weakly confined axis, where N_0 is the number of atoms in the BEC. In the relevant range of magnetic field the scattering length is approximately linear with a zero crossing at $B = 880.29(8)$ G, as shown in Fig. 5.3a. Our result is in good agreement with the calculation in Ref. [67].

Armed with the calibrated scattering length, we next determine the effective scattering length of the BEC embedded in the degenerate Fermi gas. Since the mediated interactions are weak, we perform the measurement in the range of $|a_{BB}| < |a_{BF}|$ to enhance the effect. We measure the change in the scattering length by directly comparing the BEC radius R_{TF} with and without the degenerate Fermi gas present near the zero crossing $a_{BB} = 0$ (see Methods). We find that the size of the BEC is systematically smaller when Li is present, which is consistent with attractive mediated interactions (see Fig. 5.6). From our relative measurements, the effective scattering length a_{eff} displays a negative and constant offset from the bare Cs scattering length throughout the measured range (see Fig. 5.3b). The fitted offset is -4.4(3)(1.5) a_0, where the first and second uncertainties are statistical and systematic, respectively. Together with the known constant $a_{BF} = -60\,a_0$ [68], the measured offset yields a value of $\xi = 1.7(6)$ in Eq. (5.4), in fair agreement with the calculations in Refs. [119–121]. In our experiment, we deviate from the impurity scattering limit considered in Ref. [87], and we believe that our disagreement with that prediction implies that a many-body treatment is required.

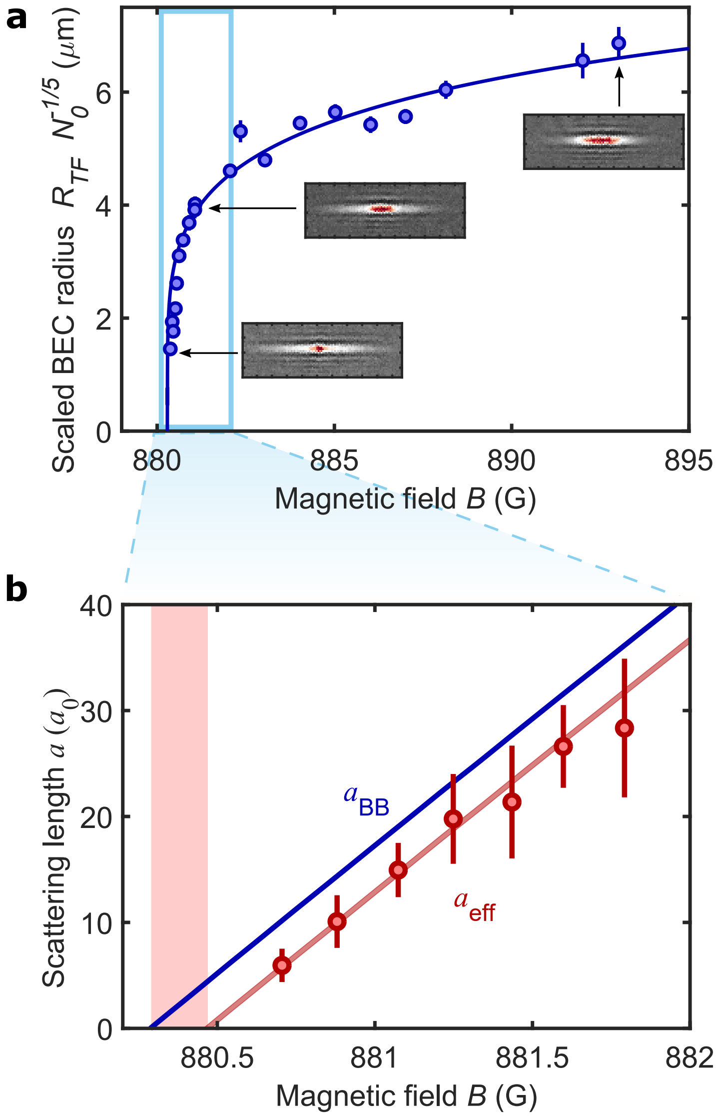

Figure 5.3: Bare and effective Cs-Cs scattering length. **a** We measure the *in situ* Thomas-Fermi radius R_{TF} of a Cs BEC in the weakly confined direction. Without the Fermi gas in the trap (blue circles), we find good agreement with theory when scaled appropriately to the number of atoms in the BEC N_0 (blue line). Characteristic images from the measurement are shown as insets. **b** At small a_{BB}, we perform a relative measurement of R_{TF} with and without Li present to extract the effective scattering length a_{eff} (red circles). Our result is consistent with a small negative offset from a_{BB} (blue line) indicating attractive mediated interactions. A fit to the data (red line) yields fair agreement with theory (see text).

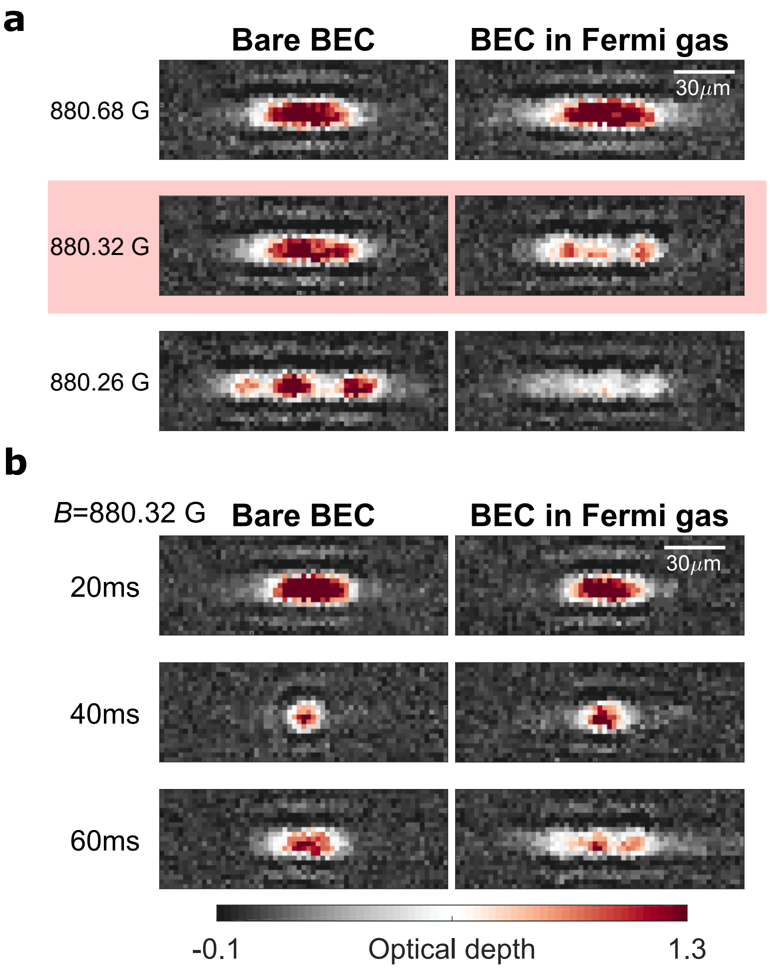

Figure 5.4: Formation of Bose-Fermi solitons. **a** *In situ* images of a Cs BEC 75 ms after a quench from $B = 885.5$ G ($a_{BB} = 120\ a_0$) to lower fields indicated on the left. For positive a_{eff}, there is no qualitative difference when the Li degenerate Fermi gas is added to the system. When a_{eff} becomes negative, the BEC collapses into a train of solitons with Li present, but remains stable without Li as shown for $B = 880.32$ G in the shaded red panels. For $a_{BB} < 0$, the BEC collapses with and without Li present. **b** Time sequence of the induced collapse at $B = 880.32$ G. Without Li present, the BEC undergoes breathing oscillations. With Li, the BEC first shrinks to a small size and afterwards breaks up into a train of solitons.

5.4 Bose-Fermi Solitons

These mediated interactions look minute, but can have a profound effect on the ground state of the Cs atoms. Labeled as the red shaded area in Fig. 5.3b, in particular, when a_{BB} is small and positive, the mediated interactions can cause a_{eff} to become negative. As an harmonically trapped BEC with attractive interactions can experience dynamic instability and collapse [39], one expects that in this regime, the mediated interactions can render the BEC unstable as well. In our highly elongated trap, the BEC enters the quasi-1D regime for scattering lengths $a_{BB} < 4\ a_0$, and Bose-Fermi soliton trains are predicted to form in this regime with sufficiently strong fermion-mediated attraction between bosons [59, 61]. In our slow ramp experiments, however, we observe very large shot-to-shot fluctuations of the shape and size of the cloud in this region, indicating the onset of the instability.

To probe the fermion-mediated instability, we perform a dynamic experiment by suddenly jumping the scattering length from a large positive value to values near the zero crossing of a_{BB} (see Fig. 5.4 and Methods). *In situ* images taken 75 ms after the quench show a qualitative difference for a bare Cs BEC and for a BEC embedded in the degenerate Fermi gas. In the absence of Li, we observe the typical formation of a soliton train for a final magnetic field below B ≈ 880.26 G, where $a_{BB} < 0$.

In the presence of Li, we observe a collapse below B ≈ 880.34 G, where $a_{BB} > 0$. This observation is consistent with the results shown in Fig. 5.3 that at this field the effective scattering length is negative $a_{\text{eff}} < 0$ and thus the stability of the BEC has been compromised. The observed soliton train is likely comprised of correlated bosonic and fermionic density waves [59, 61]. However, we could not see a clear density modulation of the Fermi gas due to limited signal-to-noise of our measurement.

The induced collapse in this interesting regime is further supported by the time evolution of the BEC following a quench. After preparing the sample at $B = 885.5$ G where $a_{BB} = 120\ a_0$, we abruptly change the field to 880.32 G, where the effective scattering length is expected to be negative $a_{\text{eff}} < 0$. We then monitor the subsequent dynamics of the BEC. Without the Fermi gas $a_{BB} > 0$ the BEC undergoes breathing oscillations without qualitative changes in the structure of the cloud. With Li present, the BEC first contracts as if starting a breathing oscillation, however, upon expansion, the BEC is fractured into a train of of 3 to 4 solitons. This observation clearly indicates that the fermion-mediated interactions are able to destabilize a weakly-interacting BEC. In other words, the ground state of the bosons may be drastically altered by the fermion-mediated interactions.

While the fermion-mediated interactions amount to only an effective change of the scattering length by -4 a_0 in our experiment, the scaling of the mediated interaction $a_{BF}^2 n_B^2 n_F$ suggests stronger influence near an interspecies Feshbach resonance as well as in systems with high local density, for example, in an optical lattice [87]. This promises exciting future work exploring the long-range nature of such interactions to ultimately probe novel quantum phases beyond contact interactions.

Acknowledgements We thank M. Gajda for useful discussions and M. McDonald for a careful reading of the manuscript. This work was supported by NSF Grant No. PHY-1511696 and the University of Chicago Materials Research Science and Engineering Center, which is funded by the National Science Foundation under Grant No. DMR-1420709.

5.5 Supplementary Materials

Dipole Oscillation Experiments

For the frequency and damping measurements presented in Fig. 5.2, we begin our experiment by preparing a quantum degenerate mixture of 2×10^4 Li and 3×10^4 Cs at rest in a harmonic trap with trapping frequencies of $\omega_{B,i}/2\pi$ = (6.65, 100, 140) Hz for Cs and $\omega_{F,i}/2\pi$ = (34, 320, 320) Hz for Li. The sample is prepared near the interspecies Feshbach resonance at either $B = 892.3$ G or $B = 893.2$ G with $a_{BF} = 300\ a_0$ or $-300\ a_0$, respectively (see

Fig. 5.5). We then apply a magnetic field gradient of 26 mG/cm along the x-axis of our trap which slightly displaces the center of both clouds by about 5 μm. The magnetic field gradient is suddenly removed which starts a dipole oscillation of both species. Due to the small displacement, the relative velocity of the center of mass of Li and Cs remains small compared to the speed of sound of the Cs BEC.

After 200 ms, the Li oscillation damps to near zero at which time we rapidly jump the magnetic field to the final target value. After a variable hold time, we measure the center of mass position of the Cs BEC after a time-of-flight expansion. The center position as a function of hold time is fit to a damped sinusoidal wave to extract the damping rate and frequency.

Coupled Oscillator Model

To understand the damping rate of the oscillation measurements in the limit of small interspecies scattering length a_{BF}, we apply the coupled oscillator model described in Ref. [126]. In this model, the center of mass position x_B of the BEC is described by

$$\ddot{x}_B = -\omega^2 x_B - \frac{4}{3}\frac{m_F N_F}{(m_F + m_B)(N_F + N_0)}\Gamma_{\text{coll}}\dot{x}_B, \tag{5.5}$$

where N_F is the number of fermions and Γ_{coll} is the collision rate. The collision rate is given by

$$\Gamma_{\text{coll}} = \sigma v \left(\frac{1}{N_F} + \frac{1}{N_0}\right) \int n_B n_F d^3x, \tag{5.6}$$

where $n_{F(B)}$ is the density of the fermions (bosons), $\sigma = 4\pi a_{BF}^2$ is the collision cross section, and the relative velocity v is approximately given by the Fermi velocity, $v \approx v_F = \hbar k_F / m_F$. For a BEC immersed in a degenerate Fermi gas, the damping rate is approximately

$$\Gamma = \kappa a_{BF}^2, \tag{5.7}$$

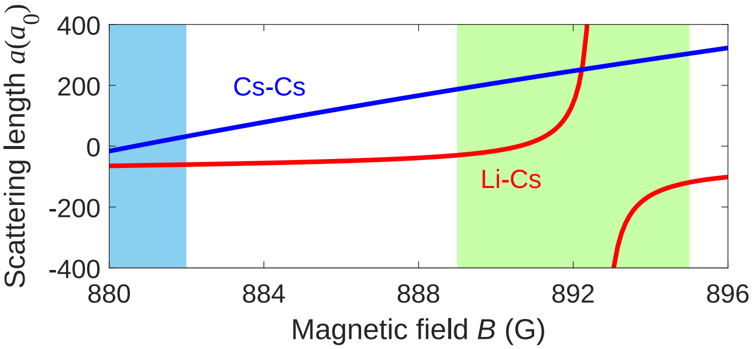

Figure 5.5: Cs-Cs scattering length a_{BB} (blue line) and Li-Cs scattering length a_{BF} (red line) over the magnetic field range studied in this work. The interspecies Feshbach resonance near $B = 892$ G is used for sample preparation and the effective trapping frequency measurements, indicated by the light green shaded area. The Cs-Cs zero crossing near $B = 880$ G is used for the effective scattering length measurements, indicated by the blue shaded area. In this region, the Li-Cs scattering length is nearly constant $a_{BF} = -60\ a_0$ [68].

where $\kappa = \frac{8\pi}{3}\frac{m_F}{m_F+m_B}\upsilon_F n_F$.

In situ Size Measurements

To measure the size of the Cs BEC we perform *in situ* absorption imaging. We first apply a 20 μs resonant microwave pulse to transfer some population from the $|F, m\rangle = |3, 3\rangle$ ground state to $|4, 4\rangle$, where F and m denote the total angular momentum and the magnetic quantum number, respectively. We then apply a 100 μs imaging pulse resonant with the $|4, 4\rangle \rightarrow |5, 5\rangle$ transition.

We use a short microwave pulse to keep the optical density low and minimize imaging artifacts, as well as to prevent the sample from spending too long in the $|4, 4\rangle$ state, where strong intraspecies repulsion [73] increases the cloud size.

Scattering Length Characterization

To characterize the bare scattering length of a pure Cs BEC, we evaporatively cool Cs at $B = 893.5$ G, and after forming a BEC we adiabatically ramp the magnetic field to a target

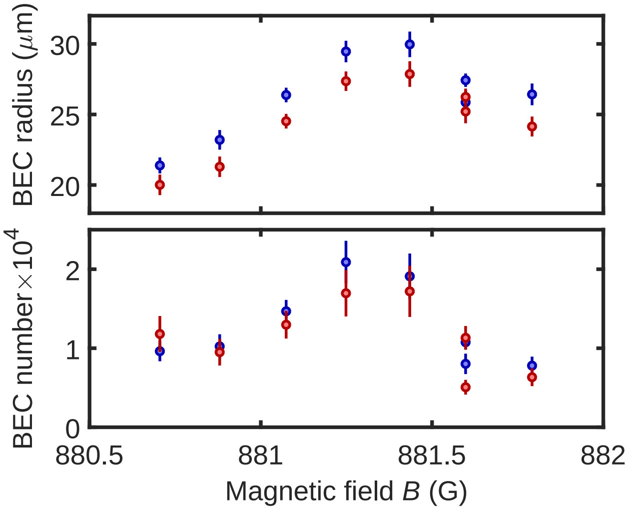

Figure 5.6: Raw data for the scattering length difference measurement. Top: Measured radius of the Cs BEC with (red circles) and without (blue circles) Li. Bottom: Measured BEC number with (red circles) and without (blue circles) Li. At every field, the size of the BEC with Li present is smaller than the corresponding measurement without Li. However, overall experimental drift makes absolute comparison difficult. Calibrating each measurement point-by-point as described in the text allows us to extract the difference in scattering length cleanly, as can be seen in Fig. 5.3b.

value over 1.4 s. Finally, we hold for 300 ms before taking an *in situ* absorption image. To extract the BEC width from the *in situ* image, we fit a line-cut through the center of the cloud to a bimodal density profile with a Thomas-Fermi distribution for the BEC and a Gaussian distribution for the thermal fraction.

Guided by the model presented in Ref. [67] for the value of the Cs scattering length, we fit our width measurements as a function of magnetic field assuming that the scattering length is approximately linear through the zero crossing. The data in Fig. 5.3a was obtained from two experimental runs, and to account for drift in our experiment we perform a joint fit of the two data sets with different atom number calibrations for each set. Additionally, we omit data taken at very small scattering lengths (below $B = 880.60$ G), where we find departures from the Thomas-Fermi approximation due to the limitations of our imaging resolution and possible effects of the quasi-1D geometry.

Scattering Length Difference Measurement

For the scattering length shift measurements presented in Fig. 5.3b, the mixture is first prepared at a magnetic field of $B = 892.1$ G and ramped over 50 ms to $B = 890.6$ G where $a_{BF} = 0$ (see Fig. 5.5). At this field, we either remove Li atoms with a 100 μs resonant light pulse or leave them in place. This procedure ensures the number of Cs atoms in the BEC is similar with or without Li present. The rest of the experiment is identical to the experiment described in the previous section.

The BEC number and raw width measurements associated with Fig. 5.3b are shown in Fig. 5.6. The observed BEC sizes are clearly smaller when Li is present for each magnetic field, which is due to the slightly decreased number and the negative contribution from the mediated interactions. The decrease in cloud size at larger fields is due to atom number variation.

Using the Thomas-Fermi approximation and the model in Ref. [67] with a zero-crossing chosen according to our experimental determination, the BEC number can be calibrated as [39]

$$N = \frac{a_{\text{ho}}}{15 a_{BB}} \left(\frac{m_B \omega_x^2 R_x^2}{\hbar \bar{\omega}} \right)^{5/2}, \tag{5.8}$$

where $a_{\text{ho}} = \sqrt{\frac{\hbar}{m\bar{\omega}}}$ is the mean harmonic oscillator length, $\omega_x/2\pi = 6.65$ Hz is the measured long-axis trap frequency, and R_{TF} is the long-axis Thomas-Fermi radius. The transverse trap frequencies are $\omega_y/2\pi = 130$ Hz and $\omega_z/2\pi = 150$ Hz, and $\bar{\omega} = (\omega_x \omega_y \omega_z)^{1/3}$ is the geometric mean of the trap frequencies.

We use the above calibration from *in situ* images in the absence of Li to in turn calibrate measurements of N_0 from time-of-flight images. This way, the combined measurements of time-of-flight and *in situ* imaging allow independent measurement of R_x and N_0 when Li is present. By performing these measurements with and without Li present, we can account for the change in size due to variation in N_0 and therefore accurately measure the change in the scattering length due to mediated interactions.

Soliton Experiments

For the experiments shown in Fig. 5.4, we begin the experiment by preparing our mixture at $B = 892.1$ G. Then, we ramp the field to $B = 890.6$ G ($a_{BF} = 0$) and either remove the Li atoms or leave them in place. Afterwards, we adiabatically ramp the field over 1.4 s to $B = 885.5$ G where the Cs-Cs scattering length $a_{BB} = 120\ a_0$. We then suddenly jump the magnetic field to a target value. The magnetic field settles in 5 ms, which is fast compared to the trap oscillation period $2\pi/\omega_x = 150$ ms.

For the images shown in Fig. 5.4a, we perform the experiment for the target fields indicated in each panel, then allow the atoms to evolve for 75 ms before *in situ* imaging the Cs BEC. For the images shown in Fig. 5.4b, we instead choose one target field and hold for the duration indicated in each panel before imaging the BEC.

CHAPTER 6

SOUND PROPAGATION IN A BOSE-FERMI MIXTURE

After we completed the experimental upgrades which were described in Chapter 3, we were interested in learning more from in-situ studies of the condensate with our improved imaging system. The measurement we made near the zero-crossing was slightly larger than the perturbative prediction, and we suspected higher order effects might play a role. They might have been detectable in the density profiles of the condensate near the zero crossing (see Appendix C.4). We were unable to resolve this experimentally, but motivated by similar questions we began to perform measurements near the Feshbach resonance using the DMD to probe the condensate. The resulting experiments, described in detail in this chapter, ended up being quite rich and interesting. This chapter is reproduced from a manuscript currently under submission. A preprint version can be found at:

Krutik Patel, Geyue Cai, Henry Ando, and Cheng Chin. Observation of sound propagaion in a strongly interacting Bose-Fermi mixture. arXiv 2205.14518, 2022.

Abstract: Particle-like excitations, or quasi-particles, emerging from interacting fermionic and bosonic quantum fields underlie many intriguing quantum phenomena in high energy and condensed matter systems. Computation of the properties of these excitations is frequently intractable in the strong interaction regime. Quantum degenerate Bose-Fermi mixtures offer promising prospects to elucidate the physics of such quasi-particles. In this work, we investigate phonon propagation in an atomic Bose-Einstein condensate immersed in a degenerate Fermi gas with interspecies scattering length a_{BF} tuned by a Feshbach resonance. We observe sound mode softening with moderate attractive interactions. For even greater attraction, surprisingly, stable sound propagation re-emerges and persists across the resonance. The stability of phonons with resonant interactions opens up opportunities to

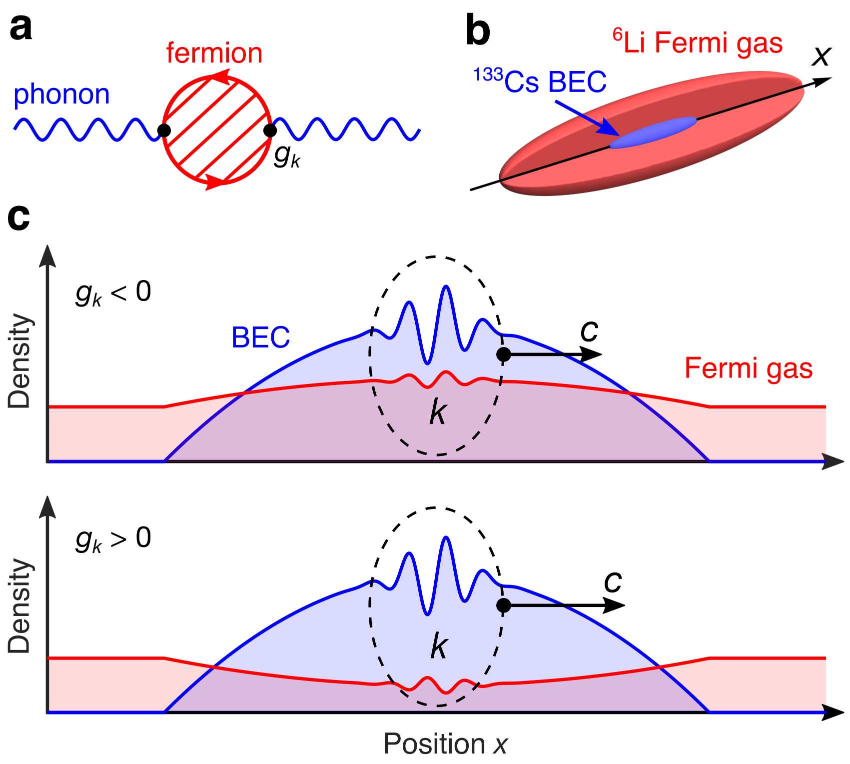

Figure 6.1: Bosonic quasi-particles (phonons) coupled to a fermionic quantum field. (a) Diagrammatic representation of phonons (blue) coupled to excitations of a fermionic field (red). The lowest order diagram contains a single loop and is second order in the phonon-fermion coupling g_k. Higher order corrections are indicated by the hatched area. (b) In our experiment, a cigar-shaped Bose-Einstein condensate (BEC) of cesium-133 is immersed in a much larger degenerate Fermi gas of lithium-6. (c) As a phonon with momentum k (black dashed ellipse) propagates, the coupling results in the density modulation of both species and the modification of the sound speed c.

investigate novel Bose-Fermi liquids and fermionic pairing in the strong interaction regime.

6.1 Introduction

Interactions between excitations of bosonic and fermionic quantum fields play an important role in understanding fundamental processes in high energy and condensed matter physics. In quantum electrodynamics, for example, the coupling between the photon and virtual electron-positron pairs polarizes the vacuum, which contributes to Lamb shifts [127] and the anomalous magnetic moments of the electron and the muon [128]. In condensed matter, interactions between phonons and electrons are central to Cooper pairing in conventional superconductors [129], as well as charge ordering and superconductivity in strongly correlated materials [130, 131].

Ultracold mixtures of atomic Bose and Fermi gases offer a complementary experimental platform for elucidating these quantum phenomena. Cold atoms are exceptionally flexible, allowing for the control of interactions between the atomic species using Feshbach resonances [42]. These capabilities have been used to study phase transitions in lattices [15, 16, 18], polarons [28, 132], and superfluid mixtures [30, 133]. Many exciting theoretical predictions for quantum simulation remain to be tested, e.g. Refs. [88, 134, 135].

In this work, we investigate sound propagation in a quantum degenerate Bose-Fermi mixture from the weak to the strong interaction regime. We optically excite density waves in the gases and measure their velocities and damping rates from *in situ* images of the Bose-Einstein condensate (BEC). We see significant changes in the speed of sound for interspecies attraction and negligible shifts for repulsion. This asymmetry indicates strong deviation from the perturbation prediction. Intriguingly, we find stable propagation of sound waves in mixtures with resonant interspecies interactions. This observation offers promising prospects to explore new quantum phases of Bose-Fermi mixtures in the strong interaction regime.

The Hamiltonian for the phonons coupled to a single-component Fermi gas is given by [53, 136]

$$H = \sum_k \epsilon_k^{\mathrm{F}} c_k^\dagger c_k + \sum_k \hbar\omega_k \alpha_k^\dagger \alpha_k + \sum_{k,q} g_k (\alpha_k + \alpha_{-k}^\dagger) c_q^\dagger c_{q-k}, \tag{6.1}$$

where ϵ_k^{F} is the dispersion of the fermions, $\hbar$ is the reduced Planck's constant, ω_k is the phonon dispersion, g_k is the phonon-fermion coupling constant, c_k and α_k refer to fermion and phonon annihilation operators respectively, and k and q are momenta (see Fig. 6.1a). In our degenerate Bose-Fermi mixture, the kinetic energy of a bare fermion is $\epsilon_k^{\mathrm{F}} = \hbar^2 k^2/2m_{\mathrm{F}}$, where m_{F} is the fermion mass. The bare phonons are low energy excitations of the BEC with the Bogoliubov dispersion [37] $\omega_k \approx c_0 k$, where the sound velocity $c_0 = \sqrt{g_{\rm BB} n_{\rm B}/m_{\rm B}}$ is determined by the boson-boson coupling constant $g_{\rm BB}$, condensate density $n_{\rm B}$, and boson mass $m_{\rm B}$. The phonon-fermion coupling constant is $g_k = g_{\rm BF}\sqrt{n_{\rm B}\hbar k^2/2m_{\rm B}\omega_k}$ [136, 137], where $g_{\rm BF} = 2\pi\hbar^2 a_{\rm BF}/m_r$ is the interspecies coupling constant, $a_{\rm BF}$ is the interspecies scattering length and m_r is the reduced mass of the two unlike atoms. The phonon-fermion coupling g_k can thus be tuned by controlling $a_{\rm BF}$ using an interspecies Feshbach resonance (see Fig. 6.1c).

Perturbation theory shows that the velocity of phonons is reduced when the BEC interacts weakly with the Fermi gas. This can be understood as a result of a fermion-mediated interaction between bosons analogous to the Ruderman-Kittel-Kasuya-Yosida mechanism [87, 110]. The mediated interaction has been observed in cold atom experiments [36, 138]. To leading order in $g_{\rm BF}$, the sound velocity is predicted to be [54]

$$c = c_0\sqrt{1 - \frac{3}{2}\frac{g_{\rm BF}^2}{g_{\rm BB}}\frac{n_{\rm F0}}{E_{\rm F0}}}, \tag{6.2}$$

where $n_{\rm F0}$ and $E_{\rm F0}$ are the density and Fermi energy of the Fermi gas in the absence of the condensate. This correction is quadratic in the coupling strength $g_{\rm BF}$, and corresponds to the one-loop diagram shown in Fig 6.1a. The sound speed is expected to be reduced regardless of the sign of the interspecies coupling strength $g_{\rm BF}$. The perturbation result is valid in the weak coupling regime $|g_{\rm BF} n_{\rm B}| \ll E_{\rm F0}$.

At stronger interactions, the density profile of each species can be significantly modified by the other species. This effect can be captured in a mean-field model. Under the Thomas-Fermi approximation for both species, the local mean-field chemical potential of the bosons depends on the fermion density as [137]

$$\mu_{\rm TF} = g_{\rm BB} n_{\rm B} + g_{\rm BF} n_{\rm F0}\left(1 - \frac{g_{\rm BF} n_{\rm B}}{E_{\rm F0}}\right)^{3/2}, \tag{6.3}$$

where the second term is set to zero when the mean-field interaction energy exceeds the Fermi energy, $g_{\mathrm{BF}} n_{\mathrm{B}} > E_{\mathrm{F0}}$. In our system, it is a good approximation that the light fermions (Li) follow the heavy bosons (Cs) adiabatically. This permits the evaluation of the mean-field sound speed $c = \sqrt{n_{\mathrm{B}}/m_{\mathrm{B}}\kappa}$ in terms of the effective compressibillity $\kappa = \partial n_{\mathrm{B}}/\partial \mu_{\mathrm{TF}}$ as

$$c = c_0 \sqrt{1 - \frac{3}{2} \frac{g_{\mathrm{BF}}^2}{g_{\mathrm{BB}}} \frac{n_{\mathrm{F0}}}{E_{\mathrm{F0}}} \sqrt{1 - \frac{g_{\mathrm{BF}} n_{\mathrm{B}}}{E_{\mathrm{F0}}}}}. \tag{6.4}$$

Compared to Eq. (6.2), the additional factor in Eq. (6.4) captures the density changes in the mixture caused by interspecies interactions.

6.2 Exciting Density Waves

Our experiments begin with mixtures of a pure BEC of 30,000 ^{133}Cs atoms and a degenerate Fermi gas of 8,000 ^{6}Li atoms, each prepared in their lowest internal state [35]. The mixture is trapped in a single beam optical dipole trap at wavelength 1064 nm with trap frequencies $\omega_{\mathrm{Cs}} = 2\pi \times (6.53, 100, 140)$ Hz and $\omega_{\mathrm{Li}} = 2\pi \times (36, 330, 330)$ Hz in the axial and two transverse directions. The bosons and fermions have a temperature of about 30 nK and chemical potentials of about $k_{\mathrm{B}} \times 30$ nK and $k_{\mathrm{B}} \times 300$ nK respectively, where k_{B} is the Boltzmann constant. In the dipole trap, the BEC is fully immersed in the degenerate Fermi gas (see Fig. 6.1b). We tune the interspecies scattering length near a narrow Feshbach resonance at magnetic field 892.65 G [68, 72, 137]. Across the resonance, the boson-boson interactions are moderately repulsive with a nearly constant scattering length $a_{\mathrm{BB}} = 270\ a_0$ [67], where a_0 is the Bohr radius. At these temperatures, the interactions between the single component Li atoms are negligible. In our experiment, the mixture is in the weak coupling regime when the interspecies scattering length is $|a_{\mathrm{BF}}| < 200 a_0$.

To study sound propagation in our system, we optically excite density waves in the mixture [139–141]. We introduce a narrow repulsive potential barrier of width $\delta = 4$ µm

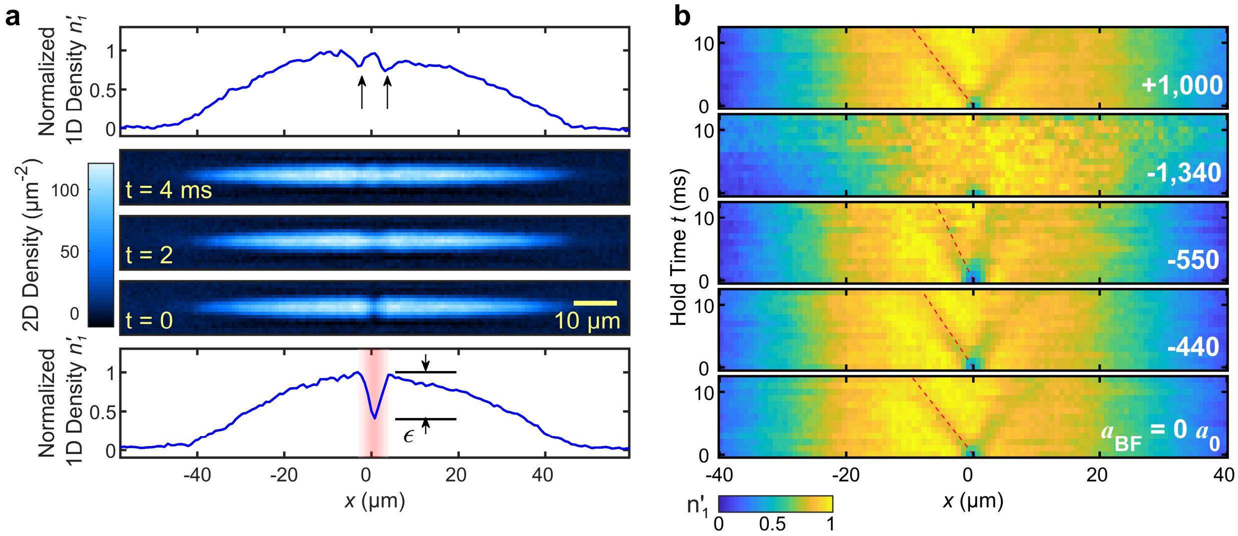

Figure 6.2: *In situ* imaging of the phonon propagation. (a) A local density depletion ϵ is created in the center of the cesium BEC by a projected laser beam (bottom panel, red shaded area). The optical potential is abruptly switched off at $t = 0$ and the density dip splits into density waves propagating in opposite directions (top panel, black arrows). Average column densities are shown for three values of the hold time $t = 0, 2, 4$ ms along with sample normalized one-dimensional (1D) densities n_1' for $t = 0$ ms and $t = 4$ ms. Data is shown for the Cs-Li Bose-Fermi mixture with interspecies scattering length $a_{\mathrm{BF}} = -335\, a_0$. (b) Normalized 1D densities n_1' show density wave dynamics for mixtures prepared at various interspecies scattering lengths. Red dashed lines are a guide to the eye.

by projecting blue-detuned light onto the center of the BEC, resulting in a density dip. At time $t = 0$ we suddenly turn off the repulsive barrier and record the dynamics of the density waves *in situ* [137]. We observe that the initial density depletion splits into two density waves that counter-propagate at the same speed along the axial direction (see Fig. 6.2a). From the images, we extract the velocity v and damping rate Γ of the density waves [137]. We repeat the experiment at different interspecies interaction strengths (see Fig. 6.2b).

The density wave velocity v in a bare elongated condensate is given by the sound speed c_0 through [137, 142]

$$v \approx \frac{c_0}{\sqrt{2}}\sqrt{1 - \frac{\epsilon}{2}}, \tag{6.5}$$

where ϵ is the initial density depletion due to the potential barrier (see Fig. 6.2a) and c_0 is the sound speed at the center of the BEC.

In the presence of fermions, we measure the dependence of the density wave velocity on the initial density depletion ϵ and find agreement with Eq. (6.5) [137]. Thus, we adopt Eq. (6.5) to link the density wave velocity to the sound speed. In the following experiments, the initial density depletion is set to $\epsilon = 0.5$.

6.3 Sound Speed Shift and Damping due to Interactions

We summarize the measured density wave velocities and damping rates in Figs. 6.3a and 6.3b. As we increase the interspecies attraction from zero, the density waves propagate slower and decay faster. The enhanced damping of the density waves is consistent with the perturbation calculation for a zero-temperature Bose-Fermi mixture [53, 137]. When the scattering length exceeds the critical value of $a_c = -790(10)\, a_0$ [137], we no longer observe stable propagation of sound. Our finding is consistent with the sound mode softening in the Bose-Fermi mixture with increasing attraction. Our measured critical value shows clear

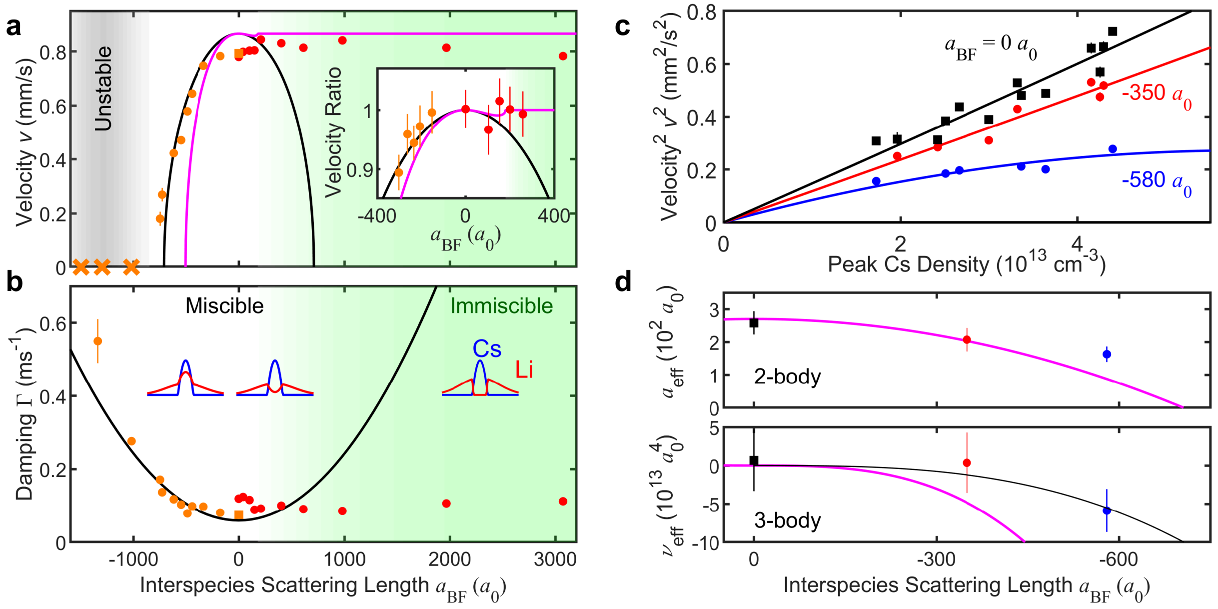

Figure 6.3: Sound wave dynamics in Bose-Fermi mixtures with tunable interspecies scattering length a_{BF}. (a) Orange data points indicate samples prepared on the attractive side of the Feshbach resonance $a_{\mathrm{BF}} < 0$. Measurement for a pure BEC is shown as the orange square. Red data points are prepared on the repulsive side with $a_{\mathrm{BF}} > 0$. The crosses indicate samples with no stable sound propagation. Inset shows the ratio of density wave velocities for samples prepared with and without the fermions. The ratios are obtained from the separation of density waves after 8 ms hold time. Calculations from perturbation (black line) and mean-field (magenta line) theory are shown for comparison. The green shaded area represents the phase separation region. The grey area indicates the region where no stable sound propagation is observed. (b) Damping rates of the density waves are compared with the perturbative prediction (black line) evaluated for momentum $k = 2\pi/(4\mu\mathrm{m})$ [137]. Insets: Cartoon representation of the Cs (blue) and Li (red) density profiles in different regimes. (c) Density wave velocity for BECs prepared without the Fermi gas (black squares) and with the Fermi gas at $a_{\mathrm{BF}} = -350\,a_0$ (red circles) and $a_{\mathrm{BF}} = -580\,a_0$ (blue circles). Lines are fits of the data to a model with both two- and three-body effective interactions between bosons (see text). (d) Colored circles are the effective scattering lengths and hypervolumes extracted from panel (c). The magenta lines are the mean-field predictions and the black line is a cubic fit to the data. The error bars in (a)-(c) are standard errors calculated from fits to averaged experimental density profiles. The error bars in (d) are standard errors calculated from fits to the data in panel (c).

deviations from the perturbation prediction $-710\,a_0$ and the mean field prediction $-510\,a_0$ for the collapse of the mixture [49].

For repulsive interspecies interactions, on the other hand, the density waves propagate with low damping and no significant change in velocity over the range we explore (see Figs. 6.3a and 6.3b). This is in stark contrast to our observations for attraction. The clear asymmetry with respect to the sign of the interaction goes beyond the perturbation prediction, see Eq. (6.2), which only depends on the square of the scattering length a_{BF}^2.

The asymmetry can be understood from the mean-field picture. For attractive interactions, fermions are pulled into the BEC, and the higher fermion density further reduces the sound velocity. On the other hand, for repulsion, fermions are expelled from the BEC, reducing their effect on the sound propagation. For strong enough repulsion, the bosons and fermions are expected to phase separate [49–51]. The observed nearly constant sound velocity for strong repulsion is consistent with the picture that most fermions are expelled from the condensate. For our system, the mean field model predicts phase separation near the scattering length $a_{\mathrm{BF}} \approx 180\,a_0$.

This asymmetry comes fundamentally from effective few-body interactions in the BEC that go beyond the perturbation calculation [143, 144]. The change of the density overlap, described in the mean-field picture, is a consequence of the few-body interactions. The three-body interaction strength can be experimentally characterized by writing the chemical potential in orders of the boson density

$$\mu = g_2 n_{\mathrm{B}} + g_3 n_{\mathrm{B}}^2 + ..., \tag{6.6}$$

where $g_2 = 4\pi\hbar^2 a_{\mathrm{eff}}/m_{\mathrm{B}}$ and $g_3 \equiv \hbar^2 \nu_{\mathrm{eff}}/m_{\mathrm{B}}$ are effective two- and three-body coupling constants between bosons, a_{eff} is the effective scattering length, and ν_{eff} is the effective scattering hypervolume. From the effective chemical potential μ we obtain the sound speed as $c \approx \sqrt{(g_2 n_{\mathrm{B}} + 2g_3 n_{\mathrm{B}}^2)/m_{\mathrm{B}}}$.

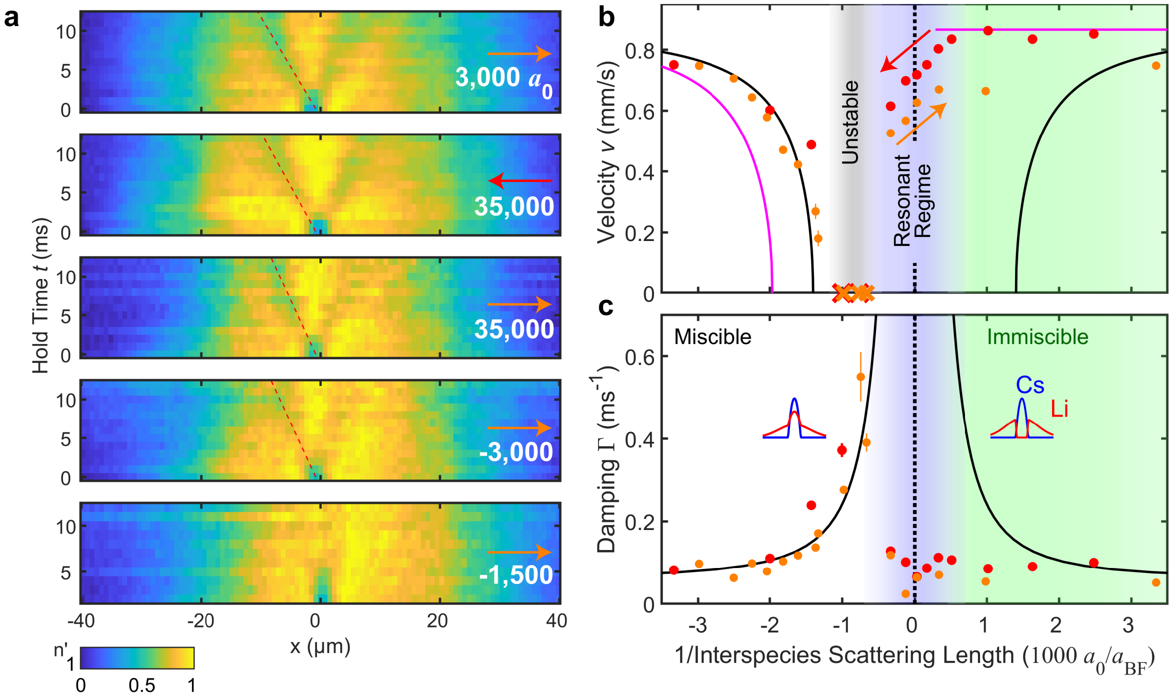

Figure 6.4: Sound propagation across the Feshbach resonance. (a) Normalized 1D densities illustrating the revival of sound propagation at strong interactions. The arrows on each data set indicate whether the system is ramped towards the resonance starting from the attractive side (orange arrow) or repulsive side (red arrow). (b) Density wave velocity of the Li-Cs mixture across the Feshbach resonance. Data taken from samples prepared on the attractive (repulsive) side are orange (red) in color. The arrows indicate the direction of the scattering length ramp. The blue and green regions indicate the resonant and phase separation regimes respectively. The vertical black dotted line indicates the position of the Feshbach resonance. (c) Damping from the same data set. The black and magenta lines are the same perturbation and mean field predictions as shown in Fig. 6.3. All shown error bars are standard errors calculated from fits to averaged experimental images.

To determine the effective two- and three-body interaction strengths, we measure the density wave velocity at various boson densities and scattering lengths. The results are shown in Fig. 6.3c. From fits to the density wave velocities and Eqs. (6.5) and (6.6), we extract the effective scattering length a_{eff} and effective scattering hypervolume ν_{eff} (see Fig. 6.3d).

As the interspecies attraction increases, we observe a reduction of the effective scattering length, consistent with Ref. [36], and an emerging scattering hypervolume. Mean-field theory predicts $\nu_{\mathrm{eff}} = \lambda a_{\mathrm{BF}}^3$ with $\lambda \approx 159 k_{\mathrm{F}}^{-1}$ set by the Fermi momentum and mass ratio [137]. Fitting the data, we determine $\lambda = 35(8) k_{\mathrm{F}}^{-1}$, see Fig. 6.3d. This value shows clear deviation from the mean field prediction. Notably, the three-body interaction $g_3 n_{\mathrm{B}}^2 \propto a_{\mathrm{BF}}^3$ is the leading order process that breaks the symmetry between positive and negative scattering length.

6.4 Sound Mode Survival at Feshbach Resonance

By ramping our magnetic field across the Feshbach resonance, we explore the sound propagation in the strong interaction regime, where the scattering length exceeds all length scales in the system. Surprisingly, we observe stable sound propagation with low damping for all scattering lengths $|a_{\mathrm{BF}}| > 3,000\, a_0$ (see Fig. 6.4) regardless of which side of the resonance the samples are initially prepared on [137]. We label this range the resonant regime. An example of the sound propagation with $a_{\mathrm{BF}} = 35,000\, a_0$ is shown in Fig. 6.4a. An interesting scenario occurs when we approach the resonance from the attractive side: the sound propagation first becomes unstable beyond the critical value a_{c}, and then recovers its stability at $a_{\mathrm{BF}} = -3,000\, a_0$ as the system enters the resonant regime.

The stable sound propagation we observe across the interspecies Feshbach resonance goes beyond the mean-field picture and offers promising prospects for future discoveries in the strong-coupling regime. At strong interactions, mean-field corrections are predicted to support a novel quantum liquid phase for scattering lengths $a_{BF} < -750\,a_0$ [145]. An Efimov resonance observed at the scattering length $a_{\rm BF} = -3,330\,a_0$ [72] could also provide three-body interactions that stabilize sound propagation in the resonant regime [144]. Finally, at strong coupling, p-wave fermionic superfluidity is conjectured when fermions are paired through the exchange of bosonic excitations [88, 136, 146], which we estimate would occur in our system in the range $a_{\rm BF} = -2,000\,a_0$ to $-10,000\,a_0$. The stable phonon propagation we observe near the Feshbach resonance offers promising prospects to explore these intriguing physics with strongly interacting Bose-Fermi mixtures.

In conclusion, we have performed *in situ* measurements of sound propagation in a Bose-Einstein condensate immersed in a degenerate Fermi gas near an interspecies Feshbach resonance. At interspecies attraction, we observe a reduction in the BEC sound speed consistent with a perturbation prediction arising from fermion-mediated interactions. At interspecies repulsion, we observe only negligible shifts in the sound speed, consistent with phase-separation of the components. Our measurements suggest that effective elastic three-body interactions between the bosons induced by the fermions play a role in the system. Finally, at resonant interactions, we observe that the sound mode of the BEC survives, permitting future studies of strongly interacting fermions and phonons.

6.5 Supplementary Materials

A. Experimental set-up and procedures

We perform experiments with both Cs and Li atoms in their absolute internal ground state loaded into a single beam optical dipole trap at a wavelength of 1064 nm. For Cs, this is the state $|F = 3, m_F = 3\rangle$, where F is the total angular momentum quantum number and m_F is its projection along the magnetic field direction. A more detailed discussion of the system preparation can be found in Ref. [35]. From our measurements of trap frequencies and beam parameters, we estimate a possible displacement between the vertical centers of each cloud of about 8 microns due to gravity. However, the mean-field potential felt by the Li due to the Cs has a trapping effect on the attractive side of resonance that improves the overlap of the two species.

In Fig. 6.5 we show the Cs-Cs and the Li-Cs scattering length as a function of magnetic field in the range where we perform the experiments. The models for the scattering length are from Refs. [67, 98, 147] and have been adjusted based on experimental measurements [36, 72].

To perform an experiment at a target interspecies scattering length a_{BF}, we first prepare the mixture at either $a_{\mathrm{BF}} = -180\, a_0$ on the attractive side or $a_{\mathrm{BF}} = 120\, a_0$ on repulsive side of resonance [35]. Then, we ramp the magnetic field to the target value in two steps. For samples initially prepared on the attractive side, shown as orange circles in Figs. 6.3, 6.4, 6.8, and 6.9, we first ramp to $a_{\mathrm{BF}} = -150\, a_0$ in 110 ms (see Fig. 6.5), then hold for 15 ms, then ramp to our target value starting at $t = -5$ ms to allow the magnetic field to settle before we turn our optical barrier off at $t = 0$. For samples prepared on the repulsive side (red circles in Figs. 6.3, 6.4, 6.8, and 6.9), we ramp first to $a_{\mathrm{BF}} = 0\, a_0$, then ramp to the target value, following the same timing procedure. For each data point, we determine the magnetic field using microwave spectroscopy of the $|3, 3\rangle \leftrightarrow |4, 4\rangle$ transition in the ground state manifold of Cs.

The boson-boson scattering length a_{BB} slightly varies over the range of magnetic fields that are studied in this work (see Fig. 6.5). This contributes an overall variation in the background bare boson sound speed value c_0, which is not included in the presented theoretical predictions and would be interpreted as a sound speed shift in the experimental data. The sound speed change due to intraspecies scattering length variation is most significant at small $|a_{\mathrm{BF}}|$, where a_{BF} varies more slowly with magnetic field. This effect is negligible for the majority of our data, but is likely responsible for the small drop in observed sound

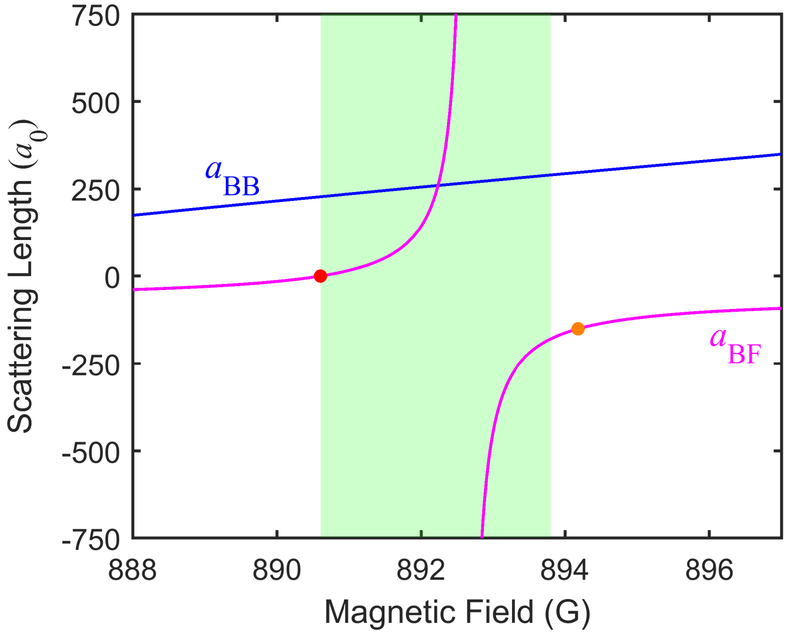

Figure 6.5: Interaction strength between atoms. The scattering length between the Cs atoms a_{BB} is shown in blue and the Li-Cs scattering length a_{BF} is shown in magenta near the interspecies Feshbach resonance. The Cs-Cs scattering length is from the model in Ref. [67] adjusted by measurements made in Ref. [36]. The Li-Cs scattering length is from the model of Ref. [147] adjusted by measurements in Ref. [72]. The red and orange circles indicate the initial magnetic field before the ramp to each target interspecies scattering length for data prepared on the repulsive and attractive side of the resonance, respectively. The shaded green area indicates the region of scattering lengths probed in this work.

speed and increase in damping at small positive values of a_{BF} in Figs. 6.3a and 6.3b.

To make the measurements shown in Figs. 6.3c and 6.3d, we linearly ramp the trap depth down to a target value then back up to its original value over 400 ms. The number of Cs atoms that escape the trap depends on the target value, allowing control over the density. We confirm that this procedure does not result in appreciable heating of the bosons or loss of the fermions.

B. In situ imaging and DMD potential projection

To obtain sufficient signal for absorption imaging of Cs, we first transfer some population from $|3,3\rangle$ to $|4,4\rangle$, where we can take advantage of the cycling transition on the D2 line from $|4,4\rangle \leftrightarrow |5',5'\rangle$. We perform this state transfer using light resonant with the $|3,3\rangle \leftrightarrow |3',3'\rangle$ transition. We image the atoms by exposing them to 2 µs of pumping light and 10 µs of imaging light with an overlapping leading edge. Our imaging is performed at an intensity $I/I_{\mathrm{sat}} \approx 6$, where I_{sat} is the saturation intensity of the cycling transition.

We perform imaging using a custom microscope objective from Special Optics with numerical aperture NA=0.6. The microscope is designed for diffraction limited performance at the D2 line of both Cs (852 nm) and Li (671 nm). The image is then captured on a CCD camera (Andor iKon M 934), see Fig. 3.7. To project the repulsive barrier onto the atoms, we reflect 635 nm light off a DMD (Texas Instruments DLP3000) and send it through the microscope using a dichroic mirror. With our imaging system, we resolve features down to 0.78(2) µm for 852 nm imaging light, which is sufficient to resolve the 4 µm wide density waves as they travel.

C. Determination of density wave velocity and damping

We extract velocities v of the density waves from images in two steps. For a given hold time t, we first integrate the images along the tight direction then normalize by the measured peak value to obtain n_1' (see Fig. 6.6a). Then, we perform a bimodal fit of the density distribution according to the fit function

$$n_{\mathrm{fit}}(x) = n_0 \left[1 - \left(\frac{x^2}{R_x^2}\right)\right]^2 + n_{\mathrm{th}} e^{\frac{-x^2}{2\sigma^2}} + C,$$

where n_0, R_x, n_{th}, σ and C are fit parameters capturing the peak 1D density of the condensate, the condensate Thomas-Fermi radius, the thermal fraction 1D peak density, and an

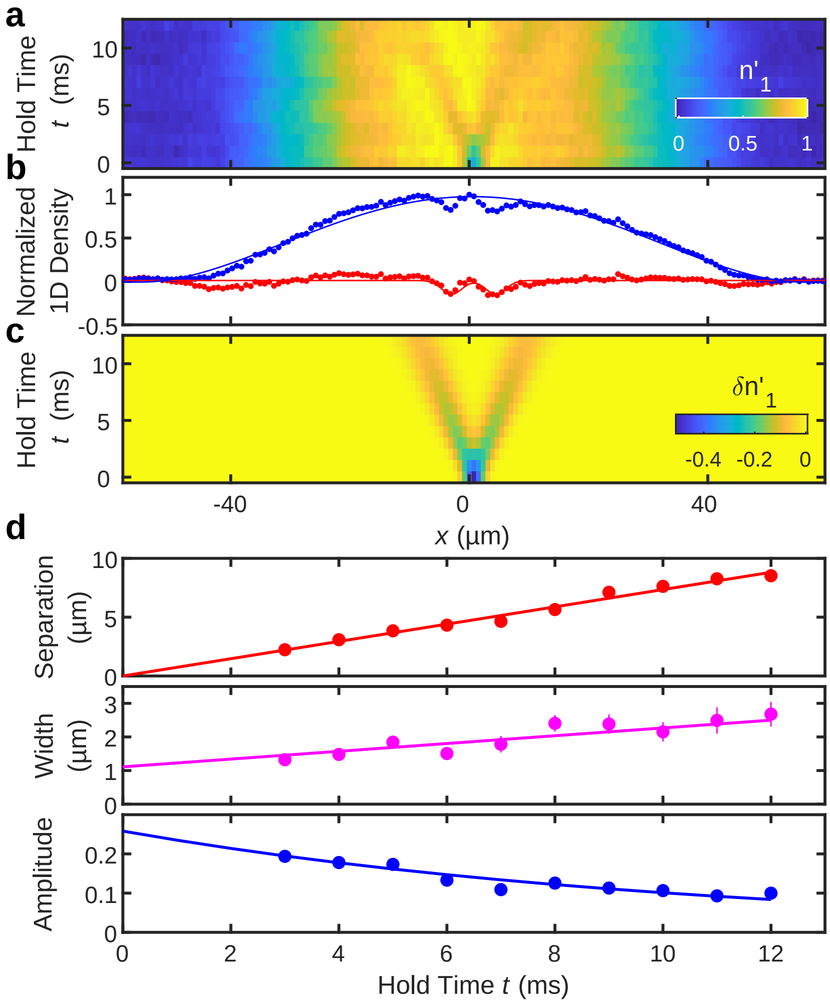

Figure 6.6: Data analysis procedure for the extraction of sound speed and damping from the experimental data. Sample analysis is shown for interspecies scattering length $a_{\mathrm{BF}} = -335\, a_0$. (a) Dynamics of normalized 1D profiles n'_1. (b) Sample profiles for $t = 5$ ms. The measured 1D density n'_1 (blue circles) is fit to a bimodal fit function (blue line, see text). The fit is subtracted off to produce the density wave profile $\delta n'_1$ (red circles). The red line is obtained from the full 2D fit shown in (c). (d) Amplitudes, widths and separations of the density waves versus time extracted from $\delta n'_1$ compared for 2D fits (lines) and independent 1D Gaussian fits (circles). The lines are the separation vt, the width $\sigma_0 + bt$ and the amplitude $Ae^{-\Gamma t}$ from the 2D fit (see text).

offset that accounts for possible detection noise. We subtract the fit from the data to obtain the density profile of the density waves $\delta n_1' = n_1' - n_{\text{fit}}$ (see Fig. 6.6b).

We then perform a 2D fit to the evolution of the density wave profiles $\delta n_1'$ using the function

$$\delta n_{\text{fit}}(x,t) = Ae^{-\Gamma t}\left[e^{\frac{-(x-x_0+vt)^2}{2(\sigma_0+bt)^2}} + e^{\frac{-(x-x_0-vt)^2}{2(\sigma_0+bt)^2}}\right] + C,$$

where A, Γ, x_0, v, σ_0, b and C are fit parameters representing the initial amplitude, the decay rate, the position of the initial depletion, the density wave velocity, the initial depletion width, the rate at which the depletion widens over time, and an offset that accounts for possible detection noise (see Fig. 6.6c).

The fit function δn_{fit} assumes constant velocity motion of the depletions, an exponential decay of their amplitude, and a linear increase in their width. These constraints are chosen based off the observed behavior of the depletions when the density wave profile $\delta n_1'$ for each hold time is fit independently by a pair of Gaussian functions. The extracted amplitudes, widths, and separations of the waves from 2D fits and independent 1D fits are compared in Fig. 6.6d, for hold times after the peaks have separated enough to yield reliable results for both methods.

While both methods yield compatible results for the extracted velocities, we find that the full 2D fits are more robust against noise in the data. Additionally, performing the 2D fits allows us to extract information from early times before the two peaks have become separated, permitting measurement of the damping rate Γ without additional assumptions.

The background subtraction process is imperfect, due to large length scale variation of the BEC density profile. This corresponds to some uncertainty in which parts of the density profile are the density wave and which parts are the background. We attribute an uncertainty of 5% to this systematic, which is estimated by comparing extracted velocities for different viable background subtractions. This is the largest estimated systematic uncertainty in our analysis.

D. Dependence of density wave dynamics on depletion

In our elongated geometry, density waves propagating along the long axis of the condensate can be described as waves in the 1D density n_1 that travel with a velocity v_0 [142], given by

$$v_0^2 = \frac{\bar{n}_{\mathrm{B}} g_{\mathrm{BB}}}{m_{\mathrm{B}}} = c_0^2 \frac{\bar{n}_{\mathrm{B}}}{n_{\mathrm{B}}},$$

where $\bar{n}_{\mathrm{B}} = n_1/A$ is the mean 3D density over the transverse cross-section A and n_{B} is the 3D density evaluated along the symmetry axis. For harmonic transverse confinement, the Thomas-Fermi approximation gives $\bar{n}_{\mathrm{B}} = n_{\mathrm{B}}/2$ and thus $v_0 = c_0/\sqrt{2}$.

For a density wave with significant density depletion δn_1, the propagation speed is reduced due to the lower mean density. Assuming the cross-section A is constant during the propagation, the density wave velocity v is given by

$$v \approx \frac{c_0}{\sqrt{2}} \sqrt{1 - \frac{\delta n_1}{n_1}} \equiv \frac{c_0}{\sqrt{2}} \sqrt{1 - \frac{\epsilon}{2}},$$

where $\epsilon \equiv 2\delta n_1/n_1$ is the fractional depletion of the 1D density induced by the optical barrier. The factor of 2 accounts for the splitting of the initial density depletion into two equal amplitude density waves propagating in opposite directions.

We compare the measured density wave velocities v to this prediction by varying the optical power in the potential barrier, see Fig. 6.7a. The depletion ϵ is extracted from a single Gaussian fit to the initial perturbation density profile $\delta n_1'$ at hold time $t = 0$. In the absence of fermions, we find fair agreement with Eq. (6.5). A linear fit to the squared velocity $v^2 = \nu_0^2 + m\epsilon$ gives $\nu_0 = 0.91(2)$ mm/s, and thus $c_0 = 1.28(3)$ mm/s. This value is consistent within 10% of our estimate. From the fit, we determine the slope to be $m = -0.5(1)\nu_0^2$ consistent with the prediction $-0.5\,\nu_0^2$.

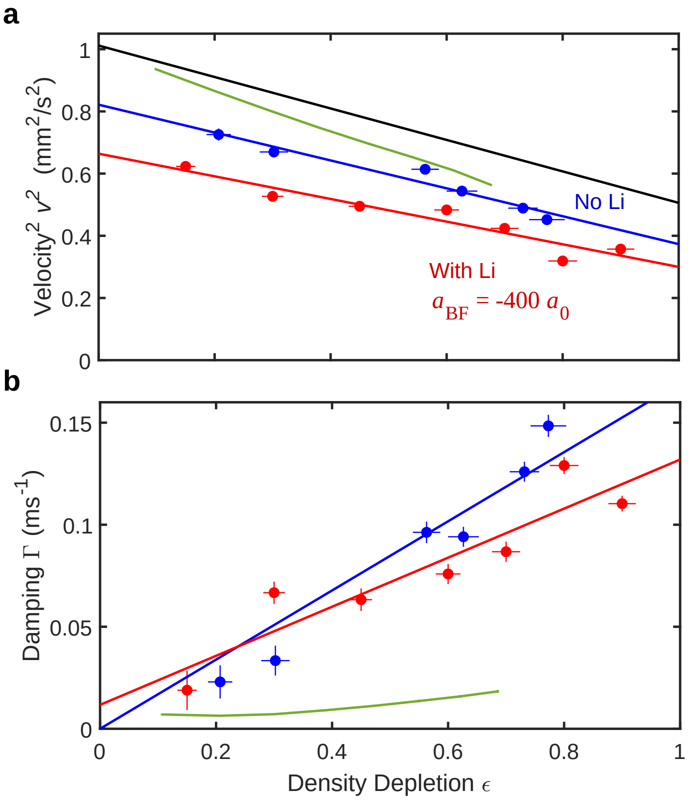

Figure 6.7: Effect of initial depletion on density wave velocity and damping. (a) The measured density wave velocity is shown for samples with no fermions present (blue circles) and in the presence of fermions with $a_{\rm BF} = -400\,a_0$ (red circles). In both cases, the dependence of the squared sound velocity is well captured by a linear fit (blue and red lines). The black line is the analytical result Eq. (6.5) and the green line is from the hydrodynamic simulations (see Section G), both evaluated in the absence of fermions. (b) Measured damping for the same data sets shown in the same colors. The blue and red lines are linear fits to the data. The green line is from the hydrodynamic simulation without fermions. All error bars are standard errors calculated from fits to the experimental images.

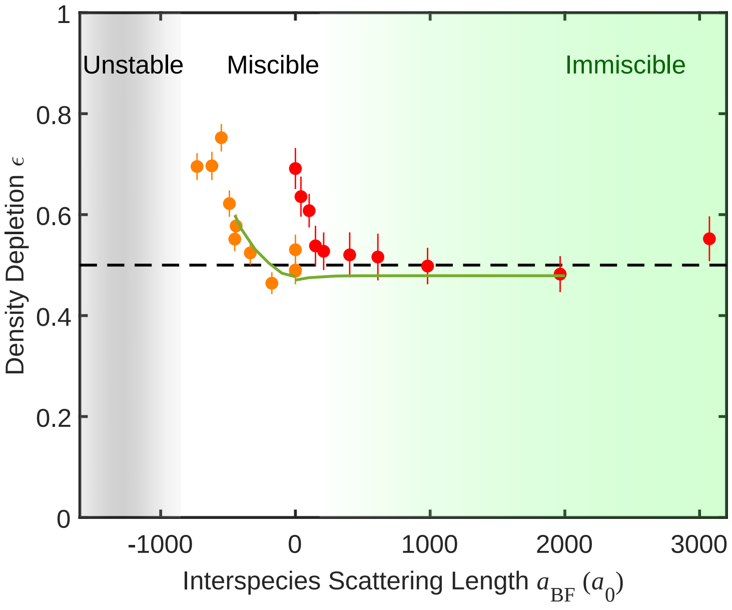

Figure 6.8: Change in initial depletion due to interspecies interactions. Orange and red circles are data from the attractive and repulsive side, respectively. The green solid line is simulated from the hydrodynamic model (see Section G). The black dashed line indicates the initial experimentally set depletion $\epsilon = 0.5$ for interspecies scattering length $a_{\mathrm{BF}} = -150\,a_0$. The region shaded in grey indicates where we observe unstable sound propagation, and the region in green indicates phase separation of the components. Error bars are standard errors calculated from fits to averaged density profiles.

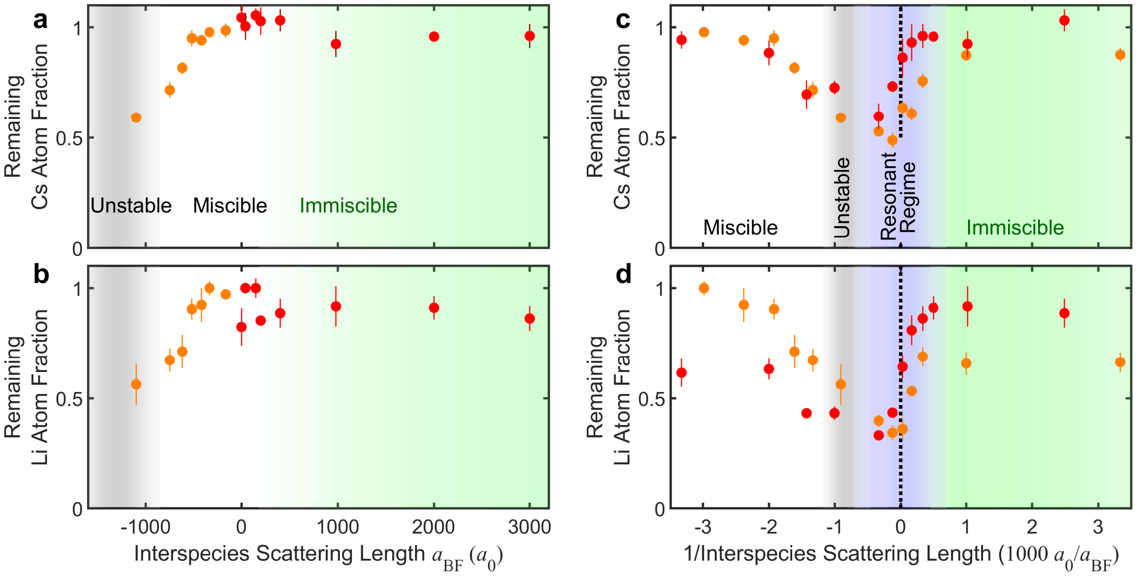

Figure 6.9: Loss of Cs and Li atoms across the Feshbach resonance. Experimental data showing the fraction of Cs atoms (panel (a) and (c)) and Li atoms (panel (b) and (d)) remaining after a hold time of $t = 6$ ms. The orange and red circles indicate experiments performed by preparing on the attractive and repulsive side of the Feshbach resonance, respectively. The Cs atom data is taken after a 4 ms time of flight, and the Li data is taken *in situ*. The region shaded in grey indicates the region where no stable sound propagation is observed. The region shaded in green indicates the phase separated region. The region indicated in blue indicates the resonant regime. The dotted line in panels (c) and (d) indicate the position of the Feshbach resonance. Error bars are the standard error.

The same experiment in the presence of fermions at scattering length $a_{\mathrm{BF}} = -400\,a_0$ with similar particle number yields an overall reduction of the density wave velocity. Using the same fit function, we obtain $\nu_0 = 0.81(2)$ mm/s and the slope $m = -0.5(1)\nu_0^2$, consistent with Eq. (6.5).

The initial depletion ϵ also has a significant effect on the damping rate, as shown in Fig. 6.7b. This effect is much weaker in our simulation, which suggests that it does not come from the nonlinearity present in that model. To characterize the damping quantitatively, we perform a linear fit to each data set while constraining the y-intercept to be positive. This gives a slope 0.17(2) ms^{-1} without Li and 0.12(2) ms^{-1} with Li at scattering length $a_{\mathrm{BF}} = -400a_0$.

For the data in the main text figures, we prepare our gas with an initial density depletion of $\epsilon = 0.5 \pm .05$ (see Fig. 6.2) near the initial sympathetic cooling field, prior to our magnetic field ramp at time $t = -5$ ms. However, due to the change in interspecies interactions during the ramp, the level of depletion when the optical barrier is switched off can vary as a function of the target interspecies scattering length. This variation for the data in Figs. 6.3a and 6.3b is shown in Fig. 6.8.

The increase in the depletion ϵ at negative a_{BF} is likely due to interspecies interactions, but the increase at small positive a_{BF} is likely due to the reduction of the intra species scattering length a_{BB} for those data points (see Fig. 6.5). Comparing the results in Fig. 6.7 to those in Fig. 6.8 suggests that this depletion dependence can contribute about 10% additional reduction in the depletion velocity v and an additional 0.05 ms^{-1} to the damping rate near the unstable region where the change in density depletion is greatest.

In Figs. 3b and 4b we compare the experimental data to a perturbation prediction [53]

$$\Gamma = \mathrm{Im}[\omega] = kc_0 \frac{\sqrt{\pi}(1+w)^2}{4w^2} \frac{a_{\mathrm{BF}}^2}{a_{\mathrm{BB}}^2} \sqrt{n_{\mathrm{B}} a_{\mathrm{BB}}^3},$$

where $w = \frac{m_{\mathrm{B}}}{m_{\mathrm{F}}}$ is the mass ratio between the species. To provide comparison to the data, we evaluate the perturbation prediction for a phonon momentum $k = \frac{2\pi}{\delta}$, where δ is the width of the density waves. Our measurements do not distinguish the origin of the damping, but we note that the maximum contribution from the measured depletion dependence is about 0.15 ms^{-1}, which is smaller than the largest measured values shown in Figs. 6.3 and 6.4.

E. Atom loss

The atom loss rate due to three-body recombination can change both due to changes in the three-body loss rate coefficient and the overlap of the two species. The high atomic densities in the *in situ* images lead to complications in the direct determination of the atom number.

We therefore perform a complimentary experiment where we control the interspecies interactions identically as for the data in the main text, but do not excite sound waves using the optical barrier. We count the atom number after a hold time of $t = 6$ ms, imaging the Cs atoms after a 4 ms time of flight expansion and the Li atoms *in situ*. The results are presented in Fig. 6.9. The peak of the loss in each case appears close to the pole of the Feshbach resonance, rather than in the region highlighted in grey where we do not see stable sound propagation.

We note that the measured velocities at resonance are slightly lower for samples prepared on the negative side compared to the positive side (see Fig. 6.4). We attribute this to the stronger particle loss on the attractive side of the resonance.

F. Phonon-fermion coupling

In this section, we briefly summarize a portion of the discussion of Ref. [53] to obtain the phonon-fermion coupling in the Bose-Fermi mixture. We start from the Hamiltonian for the uniform mixture in the Bogoliubov approximation

$$H = \sum_k \epsilon_k^{\mathrm{F}} c_k^\dagger c_k + E_{\mathrm{B}} + \sum_k \hbar\omega_k \alpha_k^\dagger \alpha_k + g_{\mathrm{BF}} \int d\vec{r}\; n_{\mathrm{B}} n_{\mathrm{F}},$$

where $\epsilon_k^{\mathrm{F}} = \frac{\hbar^2 k^2}{2m_{\mathrm{F}}}$ is the kinetic energy of a fermion, E_{B} is the ground state energy of the bosons, n_{F} is the average fermion density, n_{B} is the average boson density, and $\hbar\omega_k = \sqrt{\left(\epsilon_k^{\mathrm{B}}\right)^2 + 2g_{\mathrm{BB}} n_{\mathrm{B}} \epsilon_k^{\mathrm{B}}}$ is the Bogliubov dispersion, where $\epsilon_k^{\mathrm{B}} = \frac{\hbar^2 k^2}{2m_{\mathrm{B}}}$ is the kinetic energy of a boson. The first term is the total kinetic energy of the Fermi gas, the next two terms are the energy of the Bose gas, and the last is the total interaction energy between the two components.

The annihilation and creation operators α_k and $\alpha_k^\dagger$ for the phonons are related to the corresponding operators for the bosonic atoms a_k and $a_k^\dagger$ through the Bogoliubov transformation

$$a_k = u_k \alpha_k + v_k \alpha_{-k}^\dagger$$

$$a_k^\dagger = u_k \alpha_k^\dagger + v_k \alpha_{-k},$$

with coefficients defined by

$$u_k^2 = \frac{1}{2}\left(\frac{\epsilon_k^{\mathrm{B}} + g_{\mathrm{BB}} n_{\mathrm{B}}}{\hbar\omega_k} + 1\right)$$

$$v_k^2 = \frac{1}{2}\left(\frac{\epsilon_k^{\mathrm{B}} + g_{\mathrm{BB}} n_{\mathrm{B}}}{\hbar\omega_k} - 1\right).$$

The interaction term is rewritten by defining density fluctuation operators at momentum k

$$\rho_k^{\mathrm{B}} = \frac{1}{\sqrt{V}} \int d\vec{r}\, e^{i\vec{k}\cdot\vec{r}} [n_{\mathrm{B}}(\vec{r}) - n_{\mathrm{B}}] = \frac{1}{\sqrt{V}} \sum_q a_q^\dagger a_{q+k}$$

$$\rho_k^{\mathrm{F}} = \frac{1}{\sqrt{V}} \int d\vec{r}\, e^{i\vec{k}\cdot\vec{r}} [n_{\mathrm{F}}(\vec{r}) - n_{\mathrm{F}}] = \frac{1}{\sqrt{V}} \sum_q c_q^\dagger c_{q+k}.$$

where $n_{\mathrm{B}}(\vec{r})$ and $n_{\mathrm{F}}(\vec{r})$ are the local boson and fermion densities, respectively. The ground state energy of the bosons is $E_\mathrm{B} = g_\mathrm{BB} n_\mathrm{B} N_\mathrm{B}/2$, where N_B is boson number. The interaction term is now:

$$g_\mathrm{BF} \int d^3 r n_\mathrm{B} n_\mathrm{F} = g_\mathrm{BF} N_\mathrm{B} n_\mathrm{F} + g_\mathrm{BF} \sum_k \rho_k^\mathrm{B} \rho_{-k}^\mathrm{F}.$$

Using the Bogoliubov approximation, the boson density fluctuation operator is given by

$$\rho_k^\mathrm{B} \approx \sqrt{n_\mathrm{B} \hbar k^2 / 2 m_\mathrm{B} \omega_k} (\alpha_k + \alpha_{-k}^\dagger).$$

Substituting this into the interaction term, we arrive at the Hamiltonian in the form

$$\begin{aligned} H =& E_0 + \sum_k \epsilon_k^\mathrm{F} c_k^\dagger c_k + \sum_k \hbar \omega_k \alpha_k^\dagger \alpha_k \\ &+ g_\mathrm{BF} \sqrt{n_\mathrm{B}} \sum_{k,q} \sqrt{\hbar k^2 / 2 m_\mathrm{B} \omega_k} (\alpha_k + \alpha_{-k}^\dagger) c_q^\dagger c_{q-k}, \end{aligned}$$

which is Eq. (6.1) referred to in the main text with the explicit form of the coupling g_k and overall energy offset $E_0 = E_\mathrm{B} + g_\mathrm{BF} N_\mathrm{B} n_\mathrm{F0}$ included.

G. Coupled hydrodynamic model and numerical simulation

A coupled hydrodynamic model that corresponds to a typical Gross-Pitaevskii equation for bosons and a hydrodynamic treatment for fermions can be used to approximate the long wavelength dynamics of the system. This type of treatment has been studied in detail theoretically [145, 148]. The system is described by a pair of equations:

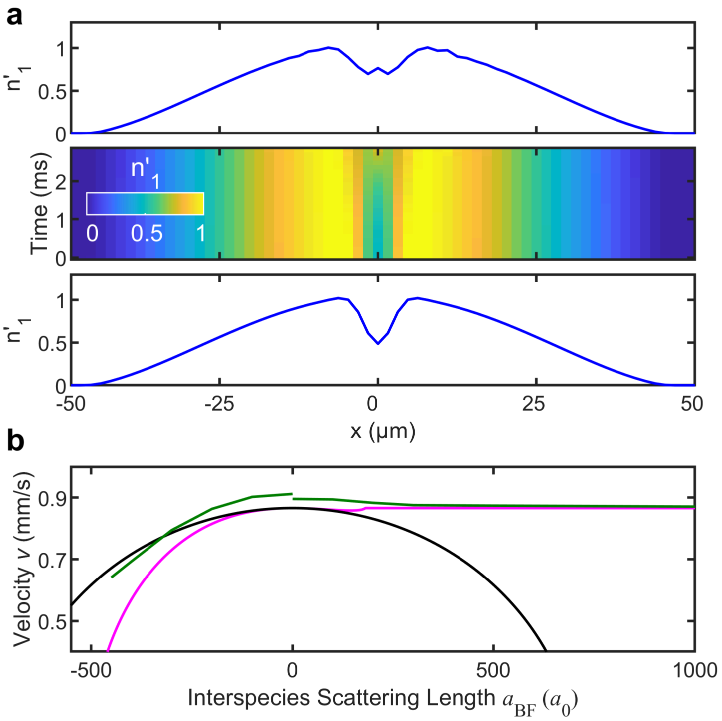

Figure 6.10: Coupled hydrodynamic simulations and comparison of all models. (a) Sample normalized 1D density profiles n_1' generated from the coupled hydrodynamic simulations for $a_{\mathrm{BF}} = -300a_0$. The lower and upper profiles are for $t = 0$ ms and $t = 2.8$ ms respectively. (b) Density wave velocities fit from 3D simulations of the experimental dynamics using the coupled hydrodynamic model are shown as the green line. The discontinuity at $a_{\mathrm{BF}} = 0$ is due to different preparation of the sample for $a_{\mathrm{BF}} > 0$ and $a_{\mathrm{BF}} < 0$ in the numerical simulation (see text). The result is compared with the perturbation (black line) , see Eq. (6.2), and mean-field prediction (magenta line), see Eq. (6.7).

$$
\begin{aligned}
i\hbar\frac{\partial\psi_{\rm B}}{\partial t} &= \Big(-\frac{\hbar^2}{2m_{\rm B}}\nabla^2 + g_{\rm BB}|\psi_{\rm B}|^2 + g_{\rm BF}|\psi_{\rm F}|^2\Big)\psi_{\rm B} \\
i\hbar\frac{\partial\psi_{\rm F}}{\partial t} &= \Big(-\frac{\hbar^2}{2m_{\rm F}}\nabla^2 + \frac{\hbar^2\xi'}{2m_{\rm F}}\frac{\nabla^2|\psi_{\rm F}|}{|\psi_{\rm F}|} + \frac{5}{3}\kappa_{\rm F}|\psi_{\rm F}|^{4/3} \\
&\quad + g_{\rm BF}|\psi_{\rm B}|^2\Big)\psi_{\rm F},
\end{aligned}
$$

where $\psi_{\rm B}$ is the condensate wavefunction, $\xi' = 8/9$ is a factor arising from the Von Weiszacker gradient correction [149], $\kappa_{\rm F} = (3/10)(6\pi^2)^{2/3}\frac{\hbar^2}{m_{\rm F}}$ and $\psi_{\rm F} = \sqrt{n_{\rm F}}e^{i\phi}$ is the fermion pseudo-wavefunction where the local velocity of fermions is $-\frac{\hbar}{m}\nabla\phi$. We evaluate the model using the split operator method [150]. In Fig. 6.10a, we show an example of 1D densities n_1' vs hold time t numerically calculated using this model. The dynamics are similar to those seen in the experiment (see Fig. 6.2).

We perform two sets of numerical simulations which capture the different experimental procedures on the negative and positive side of resonance. For these simulations, the intraspecies scattering length is held fixed at $a_{\rm BB} = 270a_0$, but the dynamics of the interspecies scattering length $a_{\rm BF}$ during the experimental magnetic field ramp are included. The evolution of the system is simulated for the duration of the 5 ms magnetic field ramp then 2.8 ms of evolution after the optical quench. A fit is performed to the simulated density wave dynamics to obtain the density wave velocity. There is an estimated systematic error of 5% in the obtained density wave velocity that arises from the choice of simulation duration. The discontinuity at $a_{\rm BF} = 0$ is due to small changes in the boson density resulting from the different initial values of the scattering length $a_{\rm BF}$ at $t = -5$ ms (see Section A).

In Fig. 6.10b we compare the predicted sound velocities from the hydrodynamic simulations to Eq. (6.2) and (6.4) discussed in the main text. We see fair agreement between our analytical models and the hydrodynamic simulations. We note that for our system parameters, our simulations suggest that there is no stable ground state for $a_{\rm BF} < -450\,a_0$, which

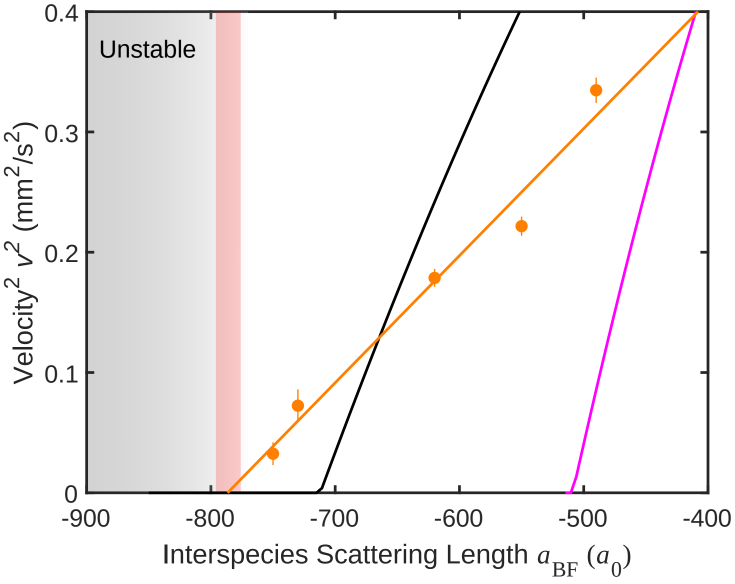

Figure 6.11: Density wave velocity near instability transition. The measured density wave velocities on the attractive side near the instability transition (orange circles) are fit to $v = \alpha\sqrt{a_{\rm BF} - a_{\rm c}}$ (orange line) to determine the critical scattering length. The red shaded area represents the standard error from the fit. For comparision, the perturbation (black line) and mean-field (magenta line) predictions are also shown. The grey area indicates the region where no stable sound propagation is observed.

we identify with instability towards collapse.

H. Thomas-Fermi approximation

In this section, we provide a more detailed explanation Eq. (6.3) and (6.4) in the main text. We use a Thomas-Fermi approximation for both species, which allows us to ignore all of the spatial gradient terms in the hydrodynamic model. We write the chemical potential of each species

$$\mu = g_{\rm BB} n_{\rm B} + V_{\rm B} + g_{\rm BF} n_{\rm F}$$

$$E_{\rm F} = \frac{\hbar^2}{2m_{\rm F}}(6\pi^2 n_{\rm F})^{2/3} + g_{\rm BF} n_{\rm B} + V_{\rm F},$$

where $V_{\rm B}$ and $V_{\rm F}$ are the external potentials felt by the bosons and fermions, respectively. If the number of fermions pulled into or pushed out of the BEC by the interspecies interaction is small compared to the total fermion number, the fermion chemical potential E_{F} is close to its bare value E_{F0}, so $E_{\mathrm{F}} \approx E_{\mathrm{F0}}$, where $E_{\mathrm{F0}} = \frac{\hbar^2}{2m_{\mathrm{F}}}(6\pi^2 n_{\mathrm{F0}})^{2/3}$. This approximation is justified in our experiment because only about 1% of the fermions are overlapped with the BEC for our system parameters.

We consider the local chemical potential of the bosons, and define $\mu_{\mathrm{TF}} = \mu - V_B$. Combining the expressions for the bosonic and fermionic chemical potentials yields

$$\mu_{\mathrm{TF}} = g_{\mathrm{BB}} n_{\mathrm{B}} + g_{\mathrm{BF}} n_{\mathrm{F0}} \left(1 - \frac{g_{\mathrm{BF}} n_{\mathrm{B}}}{E_{\mathrm{F0}}}\right)^{3/2},$$

when $g_{\mathrm{BF}} n_{\mathrm{B}}/E_{\mathrm{F0}} < 1$, as in Eq. (6.3) in the main text. This expression provides the relationship between the local boson density n_{B} and the local fermion density in the absence of the condensate n_{F0} [151].

To provide the mean-field prediction for the effective two- and three-body coupling constants g_2 and g_3 in Fig. 6.3d, we expand the chemical potential μ_{TF} to second order in n_{B}, which gives

$$\mu_{\mathrm{TF}} \approx g_2 n_{\mathrm{B}} + g_3 n_{\mathrm{B}}^2 + ...,$$

where $g_2 = g_{\mathrm{BB}} - \frac{3g_{\mathrm{BF}}^2 n_{\mathrm{F0}}}{2E_{\mathrm{F0}}}$ and $g_3 = \frac{3g_{\mathrm{BF}}^3 n_{\mathrm{F0}}}{8E_{\mathrm{F0}}^2}$. These coupling constants can be expressed as an effective two-body scattering length $a_{\mathrm{eff}} = a_{\mathrm{BB}} - \frac{m_{\mathrm{B}} m_{\mathrm{F}}}{m_r^2} \frac{k_{\mathrm{F}}}{2\pi} a_{\mathrm{BF}}^2$ and an effective scattering hypervolume $\nu_{\mathrm{eff}} = 2\pi \frac{m_{\mathrm{B}} m_{\mathrm{F}}^2}{m_r^3} k_F^{-1} a_{\mathrm{BF}}^3$.

We evaluate the density wave velocity from the compressibility and Eq. (6.5) of the main text. We obtain the final expression for the density wave velocity along the symmetry axis of an elongated Bose-Fermi mixture as

$$v = \frac{c_0}{\sqrt{2}} \sqrt{1 - \frac{\epsilon}{2}} \sqrt{1 - \frac{3}{2} \frac{g_{\mathrm{BF}}^2}{g_{\mathrm{BB}}} \frac{n_{\mathrm{F0}}}{E_{\mathrm{F0}}} \sqrt{1 - \frac{g_{\mathrm{BF}} n_{\mathrm{B}}}{E_{\mathrm{F0}}}}}. \tag{6.7}$$

This expression is used to generate the mean-field predictions (magenta lines) in Figs. 6.3,6.4, 6.10, and 6.11. To do so, we approximate the fermion density n_{F0} and the boson density n_{B} as the bare peak densities of each species. We use the peak densities because the densities do not change significantly over the axial distance that the density waves propagate. We additionally make the assumption that the peak boson density is unchanged as we change the interspecies scattering length.

In the above derivation, we assume that there is no significant radial motion of the condensate. In our experiment, we do not see clear signs of such dynamics. Furthermore, the sound speed evaluated from 3D hydrodynamic simulations (see Fig. 6.10) is in fair agreement with this simplified mean-field model.

I. Determination of the critical scattering length

As the interspecies attraction increases, both perturbation theory, see Eq. (6.2), and mean-field theory, see Eq. (6.7), predict the softening of the sound mode as $v \propto \sqrt{a_{\mathrm{BF}} - a_{\mathrm{c}}}$, where a_{c} is the critical scattering length. This dependence well captures the behavior of the data near the transition to the region of unstable sound propagation (see Fig. 6.11). We perform a fit to the 5 lowest density wave velocitiy measurements using the fit function $v = \alpha\sqrt{a_{\mathrm{BF}} - a_{\mathrm{c}}}$, where α and a_{c} are fit parameters representing the velocity scale and the critical scattering length. The fit yields the critical scattering length $a_{\mathrm{c}} = -790(10)\, a_0$ and the coefficent $\alpha = 32(1)$ µm/s $\times\, a_0^{-1/2}$.

CHAPTER 7

OUTLOOK

7.1 Long-ranged interactions between bosons

While our work published in Ref. [36] demonstrates the existence of fermion mediated interactions, it does not explicitly demonstrate their functional form or long-ranged nature. Some ideas for how this may be done are outlined below.

1. The most experimentally satisfying method would be to create two BEC's separated by a controllable distance, for example using the DMD array, and attempting to couple the two gases through the mediated interactions. However, the effect of their coupling must be impossible to explain through contact interactions. One way to do this is to kick one of the condensates and look for a coupling of its motion into the other well. Or, alternatively, one could try to look for a relative shift in the frequency of the in-phase and out-of-phase modes for the motion in the wells, since only the out-of-phase mode would be sensitive to the coupling. This experiment is similar in spirit to that proposed in Ref. [118] for fermion mixtures. Preliminary simulations suggest that for realistic conditions in our experiment, the shift would be less than a percent and therefore difficult to resolve.

2. It is also possible to obtain evidence of the long ranged interaction by performing Bragg spectroscopy. Contact interactions are delta functions in real space, meaning that they are uniform in momentum space. Therefore, long ranged interactions have a momentum cut off set by their range. Signs of this fall off can be seen in Fig. 2.8, where the modified dispersion approaches the bare dispersions at high momentum. By performing Bragg spectroscopy on the mixture and verifying that the mediated interaction vanishes at high momentum in a manner which is inconsistent with contact interactions, it can be shown that they are long ranged. Based off preliminary calculations,

our DMD projection resolution is not sufficient to resolve this effect when estimates of broadening are included for the condensate alone [152]. However, by modifying the trapping geometry or adding in additional beams to make a shorter wavelength lattice on the atoms this may be resolvable in the future.

3. Alternatively, one can seek to explicitly look for Friedel oscillations themselves in the density distribution of the gases. As discussed in Ref. [153], these Friedel oscillations are very difficult to see in a Fermi gas in general. However, it may be possible to resolve them using the condensate as a sort of amplifier for these low contrast features, due to its low energy scale and coherence. Even resolving them in response to, for example, an optical barrier would be a very interesting result. With the right choice of geometry it may be possible to resolve those caused by a tightly trapped condensate.

7.2 Three-body Physics at Degeneracy

Previous work in Chicago and Heidelburg has studied Efimov resonances in Li-Cs experimentally in ultracold, yet still thermal gases. However, there is a fascinating connection between Efimov physics and the many-body problem of polarons. When the bosons are degenerate, Ref. [154] suggests that the spectrum of the Bose polaron can be modified by Efimov physics, and that this may be observable through spectroscopy. The mass imbalance in the Li-Cs system is predicted to be favorable for the observation of these three-body correlations.

When the fermions are degenerate, the Fermi sea plays a role in the three-body physics. The RKKY interaction potential is the weakly interacting, long distance limit of a more complicated interaction between 2 bosons and a single fermion in the Fermi sea [155]. At strong interactions, the potential can be significantly modified [144, 155, 156]. Additionally, there is an interesting interplay between the length scales of the scattering length a and the inverse Fermi momentum $1/k_F$ that influences whether an Efimov like bound state is possible, and how the induced interactions behave [156]. Specifically, if the size of the Efimov trimers is large compared to the interfermion spacing, the Fermi sea shifts the Efimov resonances to weaker interaction strength. If instead the reverse is true, the trimers are suppressed. The relevant dimensionless parameter is $k_F a$, which in our system reaches unity at $\sim 7000a_0$. Furthermore, in the vicinity of an Efimov resonance, the induced interactions can be made resonant [144]. We have access to both a narrow and broad Feshbach resonance depending on whether we use Cs-$|a\rangle$ or Cs-$|b\rangle$, respectively, in the regime that we can create condensates. This may provide further avenue for study of these topics.

7.3 Bose-Fermi Liquids

Since the discovery of Bose-Bose liquid droplets [44, 45], theoretical work led by M. Gajda's group [145] has suggested that beyond mean field corrections are capable of supporting Bose-Fermi droplets as well. The leading order beyond mean field correction, analogous to the LHY correction for bosons, may also produce the required repulsion at large densities to stabilize a droplet phase. In particular, including additional interaction terms beyond mean field yields the energy:

$$E_{\mathrm{BMF}}/V = \frac{3}{5}E_F n_F + g_{BB}n_B^2/2 + g_{BF}n_B n_F + C_{LHY}n_b^{5/2} + C_{BF}n_B n_F^{4/3}A(w,\alpha) \tag{7.1}$$

where the coefficient $C_{LHY} = \frac{64}{15(\sqrt{\pi})}g_{BB}a_{BB}^{3/2}$, the coefficient $C_{BF} = (6\pi^2)^{2/3}\hbar^2 a_{BF}^2/2m_F$, and the dimensionless parameters $w = m_B/m_F$ and $\alpha = 2wg_{BB}n_B E_F$ enter through the integral $A(w,\alpha)$ given by:

$$\begin{gathered} A(w,\alpha) = \frac{2(1+w)}{3w}\left(\frac{6}{\pi}\right)^{2/3}\int_0^\infty dk\int_{-1}^{+1}d\Omega \\ \left[1 - \frac{3(k^2(1+w)}{\sqrt{k^2+\alpha}}\int_0^1 dq\, q^2\frac{1-\Theta(1-\sqrt{q^2+k^2+2kq\Omega}}{\sqrt{k^2+\alpha}+wk+2qw\Omega}\right] \end{gathered} \tag{7.2}$$

where Θ is the Heaviside step function. By evaluating the pressure, one can find that the region of mechanical instability in the Li-Cs system occurs when the ratio $a_{BF}/a_{BB} = -700a_0$ for $a_{BB} = 250a_0$.

The major challenge in reaching this droplet phase in Li-Cs is that they are predicted to stabilize at very large particle boson densities of about 10^{20} m^{-3} based on the above calculation, which would lead to very short lifetimes due to the scaling of Cs-Cs-$|a\rangle$ 3-body loss $\sim n_b^2 n_f a_{BF}^4$ of about 1 ms. However, it may be possible to detect the onset of this droplet phase, either through a dynamic measurement such as the sound measurement described in Chapter 5 or through some other non equilibrium probe. Such liquids would be a fascinating novel quantum phase that have never been created in experiment.

7.4 Boson-Mediated Interactions Between Fermions and Fermion Pairing

We have studied fermion mediated interactions in this thesis, but these Bose-Fermi mixtures also support boson mediated interactions more directly analogous to BCS pairing in materials. Much theoretical work has been done studying the feasibility of observing boson mediated pairing in Bose-Fermi mixtures [88, 146, 157, 158], although accurate calculations do not currently exist in the literature for the Li-Cs system. The simplest estimate in the static limit (using Eq. (2.33)) for the critical temperature for p-wave pairing [88] suggests that $a_{BF} \approx -2000a_0$ could be sufficient to observe pairing at our current temperature, but this neglects retardation effects. Our mass-imbalance is unfavorable for the critical temperature, but it may still be possible near the Feshbach resonance pole at higher values of $|a_{\mathrm{BF}}|$. The superfluidity would be limited to the region where the two gases overlap, which in our system represents only a small volume of the Fermi gas. However, with our new high resolution microscopy, it may be possible to identify local pairing and/or superfluidity in that region of the gas.

7.5 BEC-BCS Superfluid Mixtures

In recent years, several groups have demonstrated for the first time mixtures of BCS and BEC superfluids in quantum gases. This requires a mixture of spin states in the fermions to create the BCS component, and a boson to create the BEC. In our system, the scattering length between Li $|a\rangle$ and $|b\rangle$ is about -8000 a_0 where we create our mixtures, suggesting that we are in the appropriate regime. The major concern is that mixing the gases creates additional loss channels: in additional to the typical Cs-Cs-$|a\rangle$ and Cs-Cs-Cs loss, there can additionally be Cs-Cs-$|b\rangle$ loss and Cs-$|a\rangle$-$|b\rangle$ loss. Therefore, work must be done to check whether the evaporation process can be optimized to create mixtures in this phase. The predicted pairing temperature is given by [37]

$$T_{\text{BCS}} \approx 0.28 T_F e^{\frac{\pi}{2k_F a_{FF}}}$$

where T_F is the Fermi temperature, k_F is the Fermi momentum, and a_{FF} is the fermion-fermion scattering length. For our system parameters this gives $T_{\text{BCS}} \approx 25$ nK, which is not far from our working temperature. This pairing temperature can be affected by the interspecies interactions as well, and demonstration of a shift in the pairing temperature due to interactions with the condensate [86, 158] which would also be very interesting to observe experimentally. Due to the variety and tunability of the various scattering lengths between components near 900 G (see Fig. 3.4) there may be a rich system to explore with three components [159–162].

APPENDIX A

CHANGES TO CONTROL COMPUTER

The old control computer that powered the NI cards died, and around the same time so did some PCI cards with it. Presumably the two are related, but we may never know. It was replaced with a computer with many PCI slots from Electronic Voice Services (EVS), which is now running a slightly different set of NI cards from the previous record. The labview code has been ported over to a much newer LabView version and OS. In order to do this, the section which generated the array of values to load onto the PCI cards needed to be re-written. This was previously written in IDL using a now unsupported third-party LabView script. With the help of Joey He, this functionality was replaced with native LabView VI's and only requires the base software.

As of 05/09/2021, the following NI cards are present, and have the following names in the control computer software:

1. PCI-6733 : "AOutFastA"
2. PCI-6723 : "AOutSlowA"
3. PCI-6723 : "AOutSlowB"
4. PCIe-6536 : "DOutA"
5. PCIe-6536 : "DOutB"

where the PCI cards are analog and the PCIe cards are digital. The 6733 has better voltage resolution, but only 9 channels compared to the 6723 which has 32. The signals which rely the most on the higher resolution are currently reserved on the 6733, and the rest are on the sufficiently accurate 6723's. As of this thesis, there are about 20 open low resolution channels for future control, and still some additonal unused PCI slots. Please note that any

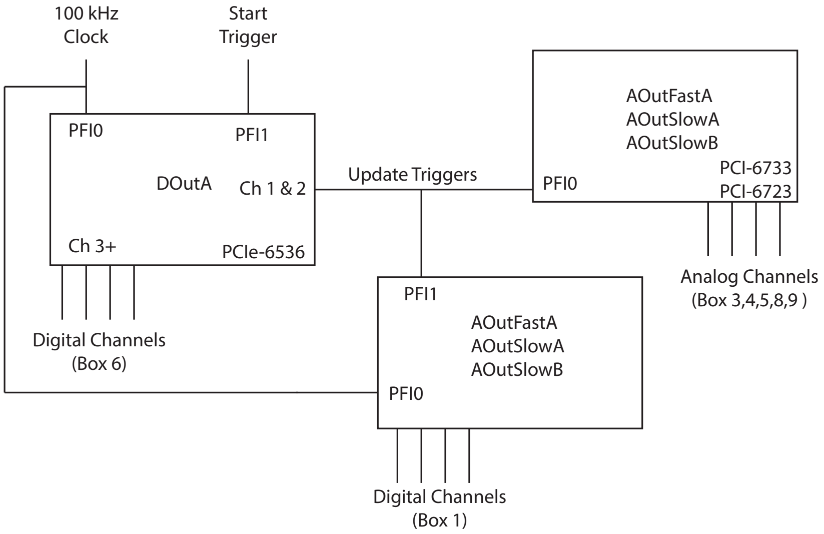

Figure A.1: Schematic of the computer control hardware.

experimental sequences loaded from before this time will not work, and if they are to be loaded should be carefully checked to not send any inadvisable commands to the Bitter coils which could damage them or the control electronics.

There is, additionally, at the time of this thesis a working spare experimental computer from EVS in middle lab with one PCI-6733 and one PCI-6536 that can be used in the event of another crash, or for general testing purposes. There is a test version of the Li-Cs experimental code which has all of the functionality of the real control system currently up and running. The overall signal flow is that there is a 100 kHz clock to the digital card (in the real experiment this is synced to the 60 Hz line voltage) which is set to trigger each voltage update in the analog card. The LabView code builds the array of voltages which need to be contained in the onboard card memory, but only updates based off changes in the voltages which are signified by a digital pulse. This allows for longer and denser experimental sequences, because the onboard memory is a significant limitation in our experimental control. It is hard to avoid, since we have 20 μs timing resolution but 30 s long experiments. See Fig. A.1 for a schematic.

APPENDIX B

CHANGING THE OVEN

Our Li flux dropped basically to zero during September of 2017. Through process of elimination, we decided that this was likely because our atomic source ran out of material, since the previous oven change had been several years before. Replacing the ovens is no small task, because it requires breaking vacuum, which is always a risky and time consuming process in an experiment under UHV. It must be done as quickly and carefully as possible to minimize contamination. In this appendix, we will discuss our method for replacing the oven and the oven design.

We first constructed the replacement oven, which was based on the previous design. The only major difference is that we removed a spacer piece of metal that may have been used to keep the Cs oven far away from the Li oven so that it wouldn't get too hot. We instead now only actively heat the Li oven, and let conduction through the vacuum components provide the heat to the Cs oven. Professor Philippe Guyot-Sionnest loaded the oven with source material inside of his nitrogen glove box, which is necessary since both Cs and Li are reactive in air. Unfortunately, in nitrogen the Li still formed a black surface layer, however this did not seem to cause problems for our flux once heated. After it was loaded, we tightened it fully and leak-checked it to verify our seals were good.

In an attempt to reduce overall contamination, we made a simple "glovebox" in which to perform the oven replacement. We laser cut circular plastic rings with mounting holes and attatched them to plastic sheeting. Latex gloves were clamped into the circular plastic rings, which allows the insertion of hands into the gloves. The edges of the plastic sheeting were then taped to the vacuum chamber at the base of the ovens, in order to contain inert gas and shield a small area from the room air.

Using the spare vacuum connection which we typically reserve for baking out the ion pump, we connected to a gas cylinder of Argon. We also closed the gate valve which blocks

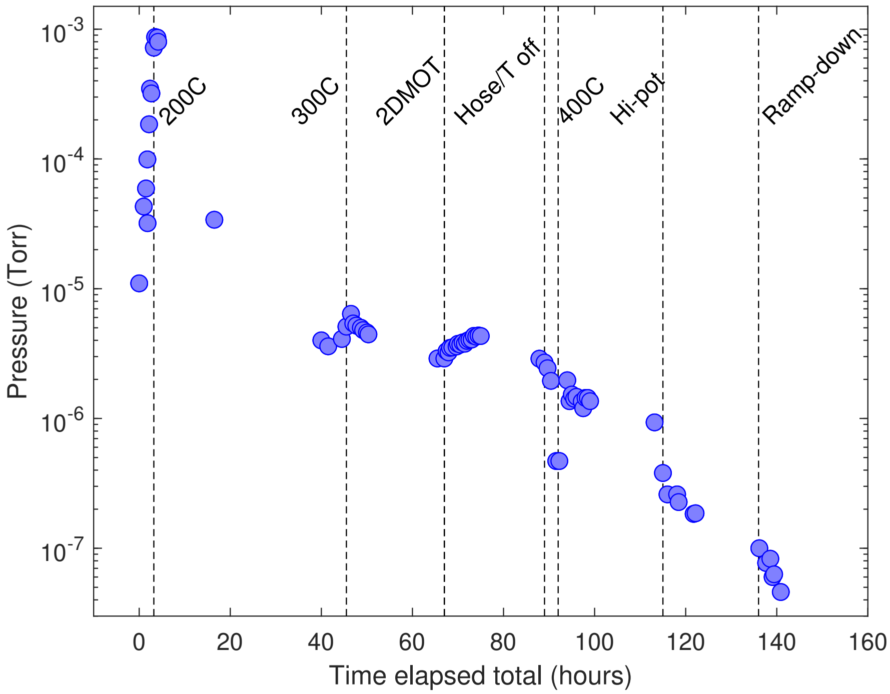

Figure B.1: First bake log after replacing the ovens. Pressure is measured at the typical cold cathode gauge on the oven side of the experiment. Over about 6 days, we brought the pressure down to the 100's of microtorr and then deemed it clean enough to open the main gate valve. Since we heated up the entire back end of the oven, we did a round of hi-potting to help clean out the ion pump as well.

off the scientific chamber. The gate valve is capable of holding against ambient air pressure.

In this configuration, opening the gas cylinder allows argon to flow through the pressure gauge, the 2D MOT chamber, the oven side ion pump, and the ovens. When we remove the ovens from the experiment, argon will flow out through the edges of our glovebox while preventing contaminating air from filling the chamber.

Once the ovens were on, we performed an initial bake-out of the surrounding vacuum system over several days. The result of that bake is shown in Fig. B.1.

The new oven is made out of the following parts:

- 1 Custom Tee from Lesker
- Elbow: MDC P/N 40300

Figure B.2: Picture of the unwrapped ovens.

- Custom blank MDC P/N 140000-2000 (0.5” thick)
- Cup (Lesker HN-SPL333)
- 6x 8-32 1.25” bolts
- 6x 8-32 05” bolts
- 6x 8-32 0.75” bolts
- 6x platenuts
- shortened hex-key
- 2 Ni Gaskets CF 1.33”
- 2 Cu Gaskets CF 1.33”

The nickel gaskets are for the seals on the Li tee, and they are chosen to better respond to the $\sim$ 350C temperature change that the oven experiences typically twice a day of operation.

It is worth noting that in the end, it turned out that we had not used up our Li source material, but it had instead rather collected in the cooler spots between the heater tape wrapping on the oven. Eventually, it had mostly plugged the available aperture for Cs, and we therefore lost most of our flux for both species.

In wrapping the replacement ovens, Geyue took great care to minimize the available locations that are not being heated well by the tape. If we find this problem to arise in the future, it may be worthwhile to try re-wrapping the ovens or otherwise redistributing the Li inside to buy time before the next oven replacement.

APPENDIX C

NUMERICAL SIMULATIONS

In this appendix, we will outline some of the various methods of numerical simulation that we have employed while studying this system. None of our major results rely on these types of numerics, but they are useful tools for us to plan experiments and for future graduate students working on the experiment.

C.1 TF Ground State Solutions by Iterating Chemical Potential

The most straightforward and computationally cheapest method to obtain reasonable ground state density profiles of the trapped mixture is iterating starting from the coupled Thomas-Fermi equations (see Chapter 2):

$$n_B(\vec{r}) = \frac{1}{g_{\mathrm{BB}}}\left(\mu_B - g_{\mathrm{BF}} n_F(\vec{r}) - V_B(\vec{r})\right)$$

$$n_F(\vec{r}) = \frac{(2m_F)^{3/2}}{6\pi^2\hbar^3}\left(\mu_F - g_{BF} n_B(\vec{r}) - V_F(\vec{r})\right)^{3/2}$$

where n_B andn_F are the boson and fermion densities, g_{BB} and g_{BF} are the coupling constants. μ_B and μ_F are the chemical potentials, and V_B and V_F are the external potentials. The chemical potentials are fixed by

$$N_B = \int n_B d\vec{r}$$

$$N_F = \int n_F d\vec{r}.$$

To be specific, one defines a grid of points to represent spatial coordinates, then beginning from an initial guess (typically we take the non-interacting ground state) evaluates both n_B and n_F, then calculates μ_B and μ_F, then re-inserts them into the coupled equations. This process is repeated until their change per iteration is below some specified tolerance which will determine the accuracy of the simulation. If the system is in a regime which is mechanically unstable, the simulation will not converge and instead the densities will blow up.

This type of numerical solution contains no kinetic energy contribution for either species, and does not permit modelling of dynamics. However, it is still quite useful and can give reasonable predictions for densities and collapse, especially if a_{BB} is reasonably large as is the case for Li-Cs at the $|a\rangle$-Cs Feshbach resonance. It does a rather poor job near the boson boson zero crossing where boson kinetic energy is important.

C.2 Coupled Hydrodynamic Equations

To more accurately model the ground state, and to find dynamics of the mixture, we typically utilize a coupled hydrodynamic model following Ref. [145]. In this type of treatment, the bosonic component is modeled using the Gross-Pitaevskii equation and the fermionic component is modelled in a hydrodynamic approximation. This hydrodynamic approximation is not necessarily well satisfed for non-interacting fermions in the mixture, but it provides the most straightforward method of simulation and can still yield useful results. There is a more sophisticated numerical method for handling the non-interacting fermions with the Boltzmann-Vlasov equation [151], which we have not yet compared to the outcome of our hydrodynamic model. The Boltzmann-Vlasov model is likely to more faithfully capture the fermion dynamics, but in the static limit we expect good agreement between the models. Furthermore, we note that the hydrodynamic approach does not contain dissipation, although this has been investigated in Ref. [163] in numerical simulations of individual fermion trajectories.

In the approach discussed here, the system is described by a pair of equations:

$$
\begin{aligned}
i\hbar\frac{\partial\psi_{\mathrm{B}}}{\partial t} &= \Big(-\frac{\hbar^2}{2m_{\mathrm{B}}}\nabla^2 + g_{\mathrm{BB}}|\psi_{\mathrm{B}}|^2 + g_{\mathrm{BF}}|\psi_{\mathrm{F}}|^2\Big)\psi_{\mathrm{B}} \\
i\hbar\frac{\partial\psi_{\mathrm{F}}}{\partial t} &= \Big(-\frac{\hbar^2}{2m_{\mathrm{F}}}\nabla^2 + \frac{\hbar^2\xi'}{2m_{\mathrm{F}}}\frac{\nabla^2|\psi_{\mathrm{F}}|}{|\psi_{\mathrm{F}}|} + \frac{5}{3}\kappa_{\mathrm{F}}|\psi_{\mathrm{F}}|^{4/3} \\
&\quad + g_{\mathrm{BF}}|\psi_{\mathrm{B}}|^2\Big)\psi_{\mathrm{F}},
\end{aligned}
\tag{C.1}
$$

where ψ_{B} is the condensate wavefunction, $\xi' = 8/9$ is a factor arising from the Von Weiszacker gradient correction [149], $\kappa_{\mathrm{F}} = (3/10)(6\pi^2)^{2/3}\frac{\hbar^2}{m_{\mathrm{F}}}$ and $\psi_{\mathrm{F}} = \sqrt{n_{\mathrm{F}}}e^{i\phi}$ is the fermion pseudo-wavefunction where the local velocity of fermions is $-\frac{\hbar}{m}\nabla\phi$. We evaluate the model using the split operator method [150].

To elaborate further, the split step operator is implemented by defining a spatial grid and a time step, then advancing the real space and kinetic energy terms of the Hamiltonian in separate steps. The advantage of this method is that instead of using discrete derivatives to evaluate the kinetic energy term, two FFTs (fast Fourier transforms) and a simple product are used instead. The time step is performed sequentially for each component of the mixture.

The spatial grid must be chosen to be large enough in size to include the expected dynamics without hitting the boundaries and the spacing should be chosen to comfortably include the relevant momenta. If not, numerical instabilities and artificial fringes can appear in the simulations. The time step δt should be chosen based off the energy scales of the simulation. As a diagnostic, the advancement per time step (for example $H\delta t$) can be output and kept to a suitably small level. Making δt larger helps computation cost but it can also introduce instabilities and fringes.

Generally speaking, the Li-Cs system is quite expensive to propagate because of the large difference in energy and length scales between the BEC and the DFG. Since the Fermi energy is an order of magnitude higher than the chemical potential, the time steps must be very fine in order to prevent instability in the Fermi gas. Additionally, the length scales of features in the BEC are frequently micron scale with our high resolution objective, but the Fermi gas is quite large which requires large spatial grids.

We perform our simulations using MATLAB's GPU support. Most of the computation time is the FFTs and IFFTs which can gain enormous speed up on good hardware (a whole order of magnitude.)

The ground state of the system can be found by performing the split-step operator in imaginary time, which turns the time dependence of each eigenstate into exponential decay rather than oscillation. If the system is iterated this way (and renormalized at some interval) then eventually all components of the solution other than the ground state will decay away, and a tolerance can be specified for convergence.

Frequently, we use this ground state as the initial state from which we perform time propagation, since this is most similar to the case of the experiment. However, it is possible to time propagate from any initial state as defined by the first time step using this type of simulation method.

Since the ground state for static potentials will not be evolving in time, there are no phase gradients. This permits simplification of the equations which speeds up the fermion computation.

For dynamics simulations, this simplification is inappropriate and the second term on the right hand side in the fermionic equation must be taken into account. This term cannot be evaluated as an FFT, so we instead must evaluate it in real space. Additionally, we must manually specify a numerical cutoff to stabilize the denominator and prevent numerical divergences. This operation reduces numerical stability and increases computation time, and typically only manifests as a small quantitative change in the density profiles.

In general, this hydrodynamic approach for the fermions is a very heavy-handed approximation. However, in the static regime, it is likely to produce accurate results for the BEC component. Since the energy scales are so seperated, the gradient terms are necessary to allow the fermions to respond to changes in the BEC density profile, but they are basically responding by following in their ground state determined by the real space terms. For this reason, the details of these kinetic energy terms are likely not very important in the regime of our experiment.

C.3 GPE Simulations With Effective Long-Ranged Interactions

As discussed in Section. 2.2, the interaction term in the Hamiltonian for the condensate atoms is approximated as a delta function. It originates from a mean-field interaction term of the form $(\int dr' U(r-r')|\psi(r')|^2)\psi(r) = g_{BB}|\psi(r)^2|\psi(r)$ for $U(r-r') = g_{BB}\delta(r-r')$. The RKKY interactions can be accounted for in a mean-field way by adding an additional component to $U(r-r')$ of the form V_{RKKY}, giving the effective GPE:

$$\left[-\frac{\hbar^2}{2m_B} + V_B(r) + \left(g_{\text{BB}}|\psi(r)|^2 + \int dr' V_{\text{RKKY}}(r-r')|\psi(r')|^2\right)\right]\psi(r) = \mu\psi(r), \quad \text{(C.2)}$$

where we have assumed that we are in the static limit with respect to the fermionic gas. In a simulation, this can be straightforwardly handled in momentum space, where we can add the static Lindhard function into each time step as we iterate using the split-step method. In the long-wavelength limit, this will naturally reduce to the effective scattering length limit. This type of simulation can be useful, because it is possible to perform identical numerics while including or excluding the explicit k dependence to look for effects that only arise due to the long ranged nature of the interaction.

These effects tend to be small for geometries that we have tested so far, but it is useful to establish this baseline for future assessments of experimental feasibility using our high resolution potential projection.

C.4 Numerical Studies Near the Boson-Boson Zero Crossing

During the early quarantine days of the pandemic, we performed a series of numerical investigations of the mixture near the boson-boson zero crossing at 880.3 G. We were curious about the role of kinetic energy in the collapse process, the possible formation of a solitonic ground state, and the modification of the density profile due to effective higher-body interactions induced in the condensate. The experimental studies that we attempted never yielded useful signal, but I have included some figures here that we created in case a future student is interested in re-visiting this topic.

We numerically studied the collapse paramters for our system near 880.3G where $a_{BB} \sim 0a_0$ and $a_{BF} = -64\, a_0$. To do so, we performed numerical simulations of the ground state in both the Thomas-Fermi approximation for both species and using the hydrodynamic approach, see Appendix C. As in the case of a bare BEC, the kinetic energy has a stabilizing effect which prevents the gas from collapsing precisely when the interaction energy vanishes. The critical conditions for collapse are compared to the Thomas-Fermi theory in Fig. C.1.

For stable systems, we extracted the size of the BEC using a Gaussian fit to compare the outcome to the perturbative prediction from the RKKY limit, see Fig. C.3. The simulated density profile has a sharp deviation from the prediction for a bare BEC with density-independent effective interactions. This point is more clearly seen in Fig. C.3, where at (inaccessibly) high particle numbers the profile is very clearly modified from either a Gaussian or TF parabolic profile.

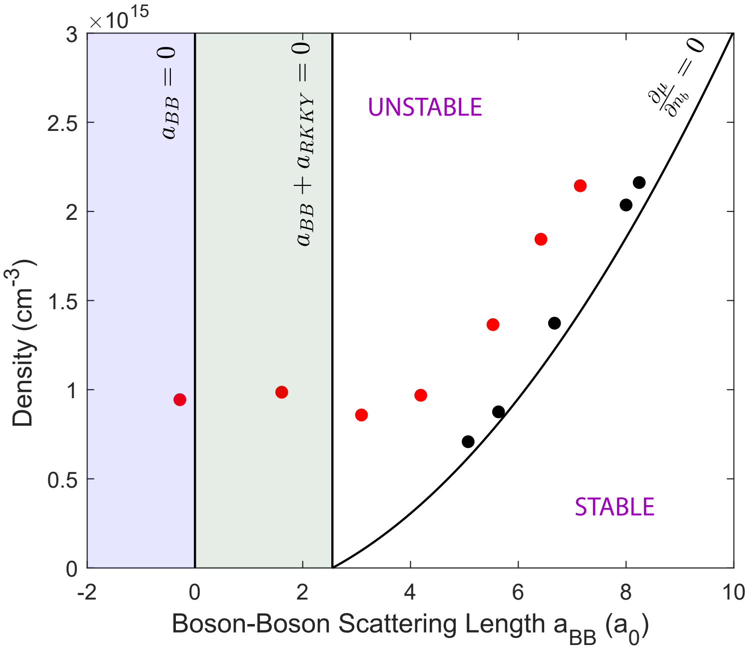

Figure C.1: Critical density for collapse of a Bose-Fermi mixture. The region above the red and black circles is unstable. The black points indicate the critical point of collapse for the mixture in neglecting the kinetic energy of both species completely. The red points show the critical density for collapse taking into account the full GPE for bosons and an effective GPE for fermions as indicated in the text. For all data the number of fermions is 2×10^4 and the boson-fermion scattering length is $a_{BF} = -64a_0$.

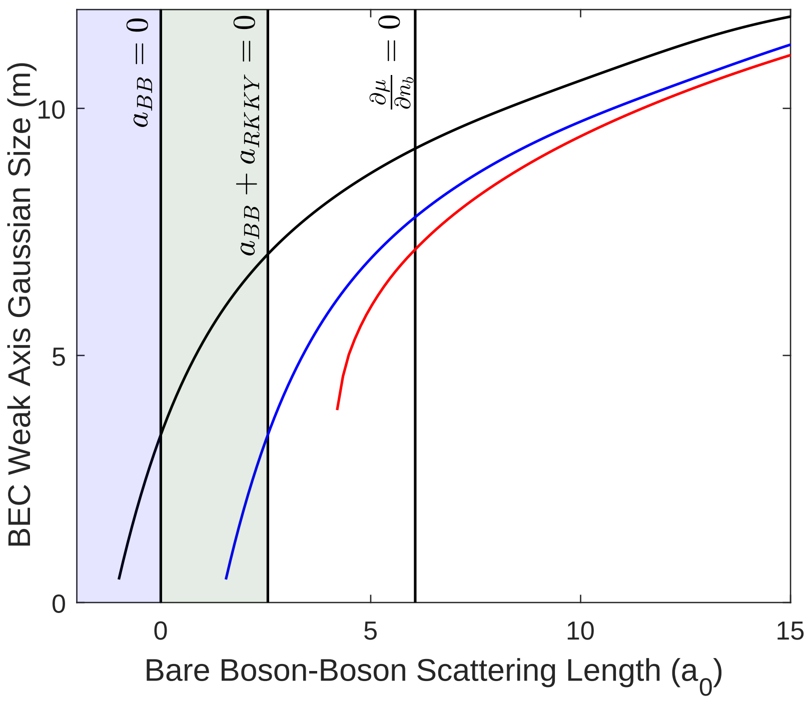

Figure C.2: Size of the bosonic component of the Li-Cs system near the Cs-Cs scattering length zero crossing at 880.3 G. Curves are simulated for 10^4 bosons and $2{\times}10^4$ fermions. The black, blue, and red curves indicate the predictions for bosons alone, the mixture including only the RKKY contribution, and the full simulation respectively. The curves are all obtained numerically through imaginary time propagation of the effective GPE's (see text).

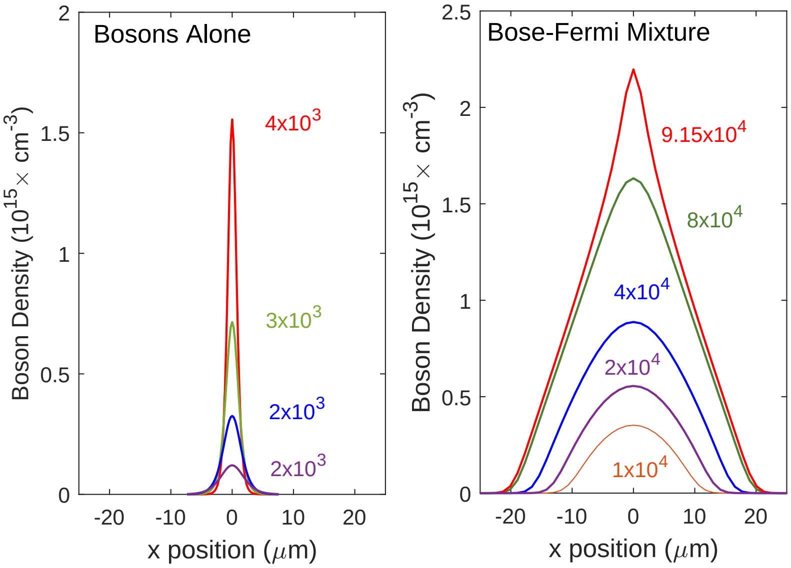

Figure C.3: Density profiles near collapse of the bosonic component. Comparison of the density profiles of bosons alone with $a_{BB} = -0.2a_0$ (left) and bosons immersed in a Fermi sea of 2×10^4 fermions with $a_{BB} = 7a_0$ and $a_{BF} - 64a_0$ (right) close to collapse. The central portion of the cloud in the mixture forms a high density structure similar to a bosonic soliton.

APPENDIX D

DMD TROUBLESHOOTING

This appendix discuss some trouble we were having with the control of our DMD, in the hopes that it may be useful to a future grad student if they run into some of the same problems.

An issue which we ran into some times with regards to our network configuration was that the default IP address of the DMD could cause problems, since it auto sets to 192.168.1.100. Using the LightCrafter software, you can reassign the IP address such that it has no conflicts.

The bigger problem that we had was that some aspect of the onboard memory failed, preventing the DMD from properly functioning. We will discuss some of the ways in which we troubleshot the board and the end solution. Unfortunately, the DLP3000 model DMD that we use in the lab does is no longer sold by Texas Instruments. We have one spare DMD which was broken that we were able to resurrect using these methods, but as far as we know it's the only other one we have access to. It should therefore only be used in case of emergency.

To talk to the DMD, you have to access it over RS232 from the UART terminal on the board. It uses a 2.5 mm stereo plug, which just looks like a smaller version of a standard headphone cable. You can solder one of these to the pins in a D-SUB connector to connect to the RS232 input available on most desktops, or use a USB-RS232 adapter for a laptop.

Connect to the board using some kind of telnet/ssh client. The free option of choice in our lab is PuTTy, but there are many available options. Set the correct session parameters as defined in the manual (Baud: 115200, Data bits: 8, stop bits: 1, Parity: none, Flow control: none) and you will get read-out from the board.

If the DMD is not performing correctly, the output can indicate to you where it is failing. For the board which is currently in the system, the output would hang or fail when attempting to boot from the on-board NAND.

The extent of our repair knowledge of the DMD is to interact with the firmware. You can download files from TI, then purchase a micro-sd card, format it to FAT-32, and either create a bootable sd card or a card which will flash the firmware onto the DMD. There is a switch on the DMD which can toggle between these two options. In the first case, the DMD loads from the SD card instead of its onboard memory, and in the other it allows the firmware to be overwritten, which may be able to return functionality to a broken device.

A significant irritation in this whole process is that many SD cards fail this process completely, for reasons that are completely unclear. There is a list of some compatible SD cards on the TI website. In our case, we went to the nearest Target and bought many different kinds, and were successful with only one of the models that we tried. It was a SanDisk Ultra Plus 128 GB microSDXC UHS-I Card. If all else fails, this card should work.

In the end, using this SD card, we found that re-flashing the firmware fixed one broken DMD in our lab. However, the one on our actual experiment has a hardware failure which we skirt by keeping the bootable SD card in the DMD and always booting from it using the toggle switch. So far, the DMD is functioning as intended in this configuration.

APPENDIX E

LIST OF PUBLICATIONS

Krutik Patel, Geyue Cai, Henry Ando, and Cheng Chin. Observation of sound propagaion in a strongly interacting Bose-Fermi mixture. arXiv 2205.14518, 2022.

Brian DeSalvo*, **Krutik Patel***, Geyue Cai, and Cheng Chin. Observation of fermion-mediated interactions between bosonic atoms. Nature, 568:61–64, 2019. *These authors contributed equally.

Brian DeSalvo, **Krutik Patel**, Jacob Johansen, and Cheng Chin. Observation of a degenerate fermi gas trapped by a bose-einstein condensate. Phys. Rev. Lett., 119:233401, 2017

Jacob Johansen, Brian DeSalvo, **Krutik Patel**, and Cheng Chin. Testing Universality of Efimov physics across broad and narrow Feshbach resonances. Nat. Phys., 13:731-735, 2017.

REFERENCES

[1] M. H. Anderson, J. R. Ensher, M. R. Matthews, C. E. Wieman, and E. A. Cornell. Observation of Bose-Einstein Condensation in a Dilute Atomic Vapor. *Science*, 269: 198–201, 1995.

[2] I. Bloch, J. Dalibard, and W. Zwerger. Many-Body Physics with Ultracold Gases. *Rev. Mod. Phys.*, 80:885, 2008.

[3] I. Bloch, J. Dalibard, and S. Nascimbène. Quantum simulations with ultracold quantum gases. *Nat. Phys.*, 8:267–276, 2012.

[4] M. Lewenstein, A. Sanpera, V. Ahufinger, B. Damski, A. Sen, and U. Sen. Ultracold atomic gases in optical lattices: Mimicking condensed matter physics and beyond. *Advances in Physics*, 56:243–379, 2007.

[5] B. DeMarco and D. Jin. Onset of Fermi Degeneracy in a Trapped Atomic Gas. *Science*, 285:1703–1706, 1999.

[6] S. Jochim, M. Bartenstein, A. Altmeyer, G. Hendi, S. Riedl, C. Chin, J. H. Denschlag, and R. Grimm. Bose-Einstein Condensation of Molecules. *Science*, 302:2101, 2003.

[7] C. A. Regal, M. Greiner, and D. S. Jin. Observation of Resonance Condensation of Fermionic Atom Pairs. *Phys. Rev. Lett.*, 92:4, 2004.

[8] M. W. Zwierlein, J. R. Abo-Shaeer, A. Schirotzek, C. H. Schunck, and W. Ketterle. Vortices and superfluidity in a strongly interacting Fermi gas. *Nature*, 435:1047–1051, 2005.

[9] L. Tarruell and L. Sanchez-Palencia. Quantum simulation of the Hubbard model with ultracold fermions in optical lattices. *Comptes Rendus Physique*, 19:365–393, 2018.

[10] F. Schreck, L. Khaykovich, K. L. Corwin, G. Ferrari, T. Bourdel, J. Cubizolles, and C. Salomon. Quasipure Bose-Einstein condensate immersed in a Fermi sea. *Phys. Rev. Lett.*, 87:804031–804034, 2001.

[11] A. G. Truscott, K. E. Strecker, W. I. McAlexander, G. B. Partridge, and R. G. Hulet. Observation of fermi pressure in a gas of trapped atoms. *Science*, 291:2570–2572, 2001.

[12] G. Roati, F. Riboli, G. Modugno, and M. Inguscio. Fermi-Bose Quantum Degenerate ^{40}K-^{87}Rb Mixture with Attractive Interaction. *Phys. Rev. Lett.*, 89:150403, 2002.

[13] Z. Hadzibabic, C. A. Stan, K. Dieckmann, S. Gupta, M. W. Zwierlein, A. Görlitz, and W. Ketterle. Two-Species Mixture of Quantum Degenerate Bose and Fermi Gases. *Phys. Rev. Lett.*, 88:4, 2002.

[14] R. Onofrio. Cooling and thermometry of atomic Fermi gases. *Phys. Usp.*, 59:1129–1153, 2016.

[15] K. Günter, T. Stöferle, H. Moritz, M. Köhl, and T. Esslinger. Bose-Fermi Mixtures in a Three-Dimensional Optical Lattice. *Phys. Rev. Lett.*, 96:180402, 2006.

[16] S. Ospelkaus, C. Ospelkaus, O. Wille, M. Succo, P. Ernst, K. Sengstock, and K. Bongs. Localization of Bosonic Atoms by Fermionic Impurities in a Three-Dimensional Optical Lattice. *Phys. Rev. Lett.*, 96:180403, 2006.

[17] T. Best, S. Will, U. Schneider, L. Hackermüller, D. Van Oosten, I. Bloch, and D. S. Lühmann. Role of interactions in ^{87}Rb-^{40}K Bose-Fermi mixtures in a 3D optical lattice. *Phys. Rev. Lett.*, 102:030408, 2009.

[18] S. Sugawa, K. Inaba, S. Taie, R. Yamazaki, M. Yamashita, and Y. Takahashi. Interaction and filling-induced quantum phases of dual Mott insulators of bosons and fermions. *Nat. Phys.*, 7:642–648, 2011.

[19] L. D. Carr, D. DeMille, R. V. Krems, and J. Ye. Cold and ultracold molecules: Science, technology and applications. *New J. Phys.*, 11:055049, 2009.

[20] J. L. Bohn, A. M. Rey, and J. Ye. Cold molecules: Progress in quantum engineering of chemistry and quantum matter. *Science*, 357:1002–1010, 2017.

[21] J. Deiglmayr, A. Grochola, M. Repp, K. Mörtlbauer, C. Glück, J. Lange, O. Dulieu, R. Wester, and M. Weidemüller. Formation of ultracold polar molecules in the rovibrational ground state. *Phys. Rev. Lett.*, 101:133004, 2008.

[22] M. G. Hu, M. J. Van De Graaff, D. Kedar, J. P. Corson, E. A. Cornell, and D. S. Jin. Bose Polarons in the Strongly Interacting Regime. *Phys. Rev. Lett.*, 117:055301, 2016.

[23] N. B. Jørgensen, L. Wacker, K. T. Skalmstang, M. M. Parish, J. Levinsen, R. S. Christensen, G. M. Bruun, and J. J. Arlt. Observation of Attractive and Repulsive Polarons in a Bose-Einstein Condensate. *Phys. Rev. Lett.*, 117:055302, 2016.

[24] C. Kohstall, M. Zaccanti, M. Jag, A. Trenkwalder, P. Massignan, G. M. Bruun, F. Schreck, and R. Grimm. Metastability and Coherence of Repulsive Polarons in a Strongly Interacting Fermi Mixture. *Nature*, 485:615–618, 2012.

[25] A. Schirotzek, C. H. Wu, A. Sommer, and M. W. Zwierlein. Observation of Fermi Polarons in a Tunable Fermi Liquid of Ultracold Atoms. *Phys. Rev. Lett.*, 102:230402, 2009.

[26] F. Scazza, G. Valtolina, P. Massignan, A. Recati, A. Amico, A. Burchianti, C. Fort, M. Inguscio, M. Zaccanti, and G. Roati. Repulsive Fermi Polarons in a Resonant Mixture of Ultracold ^{6}Li Atoms. *Phys. Rev. Lett.*, 118:083602, 2017.

[27] M. Cetina, M. Jag, R. S. Lous, J. T. M. Walraven, R. Grimm, R. S. Christensen, and G. M. Bruun. Decoherence of Impurities in a Fermi Sea of Ultracold Atoms. *Phys. Rev. Lett.*, 115:135302, 2015.

[28] I. Fritsche, C. Baroni, E. Dobler, E. Kirilov, B. Huang, R. Grimm, G. M. Bruun, and P. Massignan. Stability and breakdown of Fermi polarons in a strongly interacting Fermi-Bose mixture. *Phys. Rev. A*, 103:053314, 2021.

[29] I. Ferrier-Barbut, M. Delehaye, S. Laurent, A. Grierm, B. Rem, F. Chevy, and C. Salomon. A mixture of Bose and Fermi superfluids. *Science*, 345:1035, 2014.

[30] R. Roy, A. Green, R. Bowler, and S. Gupta. Two-Element Mixture of Bose and Fermi Superfluids . *Phys. Rev. Lett.*, 118:055301, 2017.

[31] X. C. Yao, H. Z. Chen, Y. P. Wu, X. P. Liu, X. Q. Wang, X. Jiang, Y. Deng, Y. A. Chen, and J. W. Pan. Observation of Coupled Vortex Lattices in a Mass-Imbalance Bose and Fermi Superfluid Mixture. *Phys. Rev. Lett.*, 117:145301, 2016.

[32] A. Imamoglu, D. D. Awschalom, G. Burkard, D. P. Divincenzo, D. Loss, M. Sherwin, and A. Small. Quantum information processing using quantum dot spins and cavity-QED. *Phys. Rev. Lett.*, 83:4204, 1999.

[33] V. D. Vaidya, Y. Guo, R. M. Kroeze, K. E. Ballantine, A. J. Kollár, J. Keeling, and B. L. Lev. Tunable-Range, Photon-Mediated Atomic Interactions in Multimode Cavity QED. *Physical Review X*, 8, 1 2018.

[34] J. Johansen. Feshbach and Efimov Resonances in a ^{6}Li - ^{133}Cs Atomic Mixture, PhD Thesis, University of Chicago. 2017.

[35] B. DeSalvo, K. Patel, J. Johansen, and C. Chin. Observation of a Degenerate Fermi Gas Trapped by a Bose-Einstein Condensate. *Phys. Rev. Lett.*, 119:233401, 2017.

[36] B. DeSalvo, K. Patel, G. Cai, and C. Chin. Observation of fermion-mediated interactions between bosonic atoms. *Nature*, 568:61–64, 2019.

[37] C. Pethick and H. Smith. *Bose-Einstein condensation in dilute gases.* Cambridge University Press, 2002.

[38] W. Ketterle and M. W. Zwierlein. Making, probing and understanding ultracold Fermi gases. *La Rivista del Nuovo Cimento*, 31:247–422, 2006.

[39] F. Dalfovo, S. Giorgini, L. P. Pitaevskii, and S. Stringari. Theory of Bose-Einstein condensation in trapped gases. *Rev. Mod. Phys.*, 71:463–512, 1999.

[40] W. Ketterle, D. S. Durfee, and D. M. Stamper-Kurn. Making, probing and understanding Bose-Einstein condensates. *Proceedings of the International School of Physics "Enrico Fermi"*, page 67, 1999.

[41] S. Giorgini, L. P. Pitaevskii, and S. Stringari. Theory of ultracold atomic Fermi gases. *Rev. Mod. Phys.*, 80:1215–1274, 2008.

[42] C. Chin, R. Grimm, P. Julienne, and E. Tiesinga. Feshbach resonances in ultracold gases. *Rev. Mod. Phys.*, 82:1225, 2010.

[43] L. Pitaevskii and S. Stringari. *Bose-Einstein Condensation and Superfluidity.* Oxford University Press, 2016.

[44] D. S. Petrov. Quantum Mechanical Stabilization of a Collapsing Bose-Bose Mixture. *Phys. Rev. Lett.*, 115, 2015.

[45] C. R. Cabrera, L. Tanzi, J. Sanz, B. Naylor, P. Thomas, P. Cheiney, and L. Tarruell. Quantum liquid droplets in a mixture of Bose-Einstein condensates. *Science*, 359: 301–304, 2018.

[46] B. DeMarco. Quantum Behavior of an Atomic Fermi Gas. PhD Thesis, University of Colorado at Boulder. 2001.

[47] H. Bruus and K. Flensburg. *Many-body quantum theory in condensed matter physics:an introduction.* Oxford University Press, 2004.

[48] B. Mihaila. Lindhard function of a d-dimensional Fermi gas. *arXiv 1111.5337*, 2011.

[49] K. Mølmer. Bose Condensates and Fermi Gases at Zero Temperature. *Phys. Rev. Lett.*, 80:1804, 1998.

[50] L. Viverit, C. J. Pethick, and H. Smith. Zero-temperature phase diagram of binary boson-fermion mixtures. *Phys. Rev. A*, 61:053605, 2000.

[51] R. S. Lous, I. Fritsche, M. Jag, F. Lehmann, E. Kirilov, B. Huang, and R. Grimm. Probing the Interface of a Phase-Separated State in a Repulsive Bose-Fermi Mixture. *Phys. Rev. Lett.*, 120:243403, 2018.

[52] B. Huang, I. Fritsche, R. S. Lous, C. Baroni, J. T. M. Walraven, E. Kirilov, and R. Grimm. Breathing mode of a Bose-Einstein condensate repulsively interacting with a fermionic reservoir. *Phys. Rev. A*, 99:041602(R), 2019.

[53] L. Viverit and S. Giorgini. Ground-state properties of a dilute Bose-Fermi mixture. *Phys. Rev. A*, 66:063604, 2002.

[54] S. K. Yip. Collective Modes in a dilute Bose-Fermi mixture. *Phys. Rev. A*, 64:023609, 2001.

[55] D. Santamore, S. Gaudido, and E. Timmermans. Zero Sound in a Mixture of a Single-Component Fermion Gas and a Bose-Einstein Condensate. *Phys. Rev. Lett.*, 93:250402, 2004.

[56] J. Denschlag, J. E. Simsarian, D. L. Feder, C. W. Clark, L. A. Collins, J. Cubizolles, L. Deng, E. W. Hagley, K. Helmerson, W. P. Reinhardt, S. L. Rolston, and W. D. Phillips. Generating Solitons by Phase Engineering of a Bose-Einstein Condensate. *Science*, 287:97–101, 2000.

[57] K. E. Strecker, G. B. Partridge, A. G. Truscott, and R. G. Hulet. Formation and propagation of matter-wave soliton trains. *Nature*, 417:150–153, 2002.

[58] J. H. V. Nguyen, D. Luo, and R. G. Hulet. Formation of matter-wave soliton trains by modulational instability. *Science*, 356:422–426, 2017.

[59] T. Karpiuk, M. Brewczyk, S. Ospelkaus-Schwarzer, K. Bongs, M. Gajda, and K. Rzążewski. Soliton trains in Bose-Fermi mixtures. *Phys. Rev. Lett.*, 93:100401, 2004.

[60] T. Karpiuk, M. Brewczyk, and K. Rzążewski. Bright solitons in Bose-Fermi mixtures. *Phys. Rev. A*, 73:053602, 2006.

[61] J. Santhanam, V. M. Kenkre, and V. V. Konotop. Solitons of Bose-Fermi mixtures in a strongly elongated trap. *Phys. Rev. A*, 73:013612, 2006.

[62] S. K. Adhikari. Fermionic bright soliton in a boson-fermion mixture. *Phys. Rev. A*, 72:053608, 2005.

[63] D. O. Sabulsky, C. V. Parker, N. D. Gemelke, and C. Chin. Efficient continuous-duty Bitter-type electromagnets for cold atom experiments. *Rev. Sci. Instrum.*, 84, 2013.

[64] D. A. Steck. Cesium d line data, available online at `http://steck.us/alkalidata` (revision 2.2.1). 2019.

[65] M. E. Gehm. Properties of ^{6}Li, available online at `https://jet.physics.ncsu.edu/techdocs/pdf/PropertiesOfLi_2016.pdf` . 2003.

[66] G. Zürn, T. Lompe, A. N. Wenz, S. Jochim, P. S. Julienne, and J. M. Hutson. Precise characterization of ^{6}Li Feshbach resonances using trap-sideband-resolved RF spectroscopy of weakly bound molecules. *Phys. Rev. Lett.*, 110, 2013.

[67] M. Berninger, A. Zenesini, B. Huang, W. Harm, H.-C. Nägerl, F. Ferlaino, R. Grimm, P. S. Julienne, and J. M. Hutson. Feshbach resonances, weakly bound molecular states, and coupled-channel potentials for cesium at high magnetic fields. *Phys. Rev. A*, 87: 032517, 2013.

[68] S. K. Tung, C. Parker, J. Johansen, C. Chin, Y. Wang, and P. S. Julienne. Ultracold mixtures of atomic ^{6}Li and ^{133}Cs with tunable interactions. *Phys. Rev. A*, 87: 010702(R), 2013.

[69] V. Vuletic´, V. C. Chin, A. J. Kerman, and S. Chu. Degenerate Raman Sideband Cooling of Trapped Cesium Atoms at Very High Atomic Densities. *Phys. Rev. Lett.*, 81:5768, 1998.

[70] A. Burchianti, G. Valtolina, J. A. Seman, E. Pace, M. D. Pas, M. Inguscio, M. Zaccanti, and G. Roati. Efficient all-optical production of large ^{6}Li quantum gases using D1 gray-molasses cooling. *Phys. Rev. A*, 90:043408, 2014.

[71] R. Grimm, M. Weidemüller, and Y. B. Ovchinnikov. Optical Dipole Traps for Neutral Atoms. *Advances in Atomic, Molecular and Optical Physics*, 42:95–170, 2000.

[72] J. Johansen, B. DeSalvo, K. Patel, and C. Chin. Testing universality of Efimov physics across broad and narrow Feshbach resonances. *Nat. Phys.*, 13:731–735, 2017.

[73] P. J. Leo, C. J. Williams, and P. S. Julienne. Collision Properties of Ultracold ^{133}Cs Atoms. *Phys. Rev. Lett.*, 85:2721, 2000.

[74] C.-L. Hung. In situ probing of two-dimensional quantum gases. PhD Thesis, University of Chicago. 2011.

[75] T. Takekoshi, L. Reichsöllner, A. Schindewolf, J. M. Hutson, C. R. Le Sueur, O. Dulieu, F. Ferlaino, R. Grimm, and H. C. Nägerl. Ultracold dense samples of dipolar RbCs molecules in the rovibrational and hyperfine ground state. *Phys. Rev. Lett.*, 113:205301, 2014.

[76] K.-K. Ni, S. Ospelkaus, M. H. G. de Miranda, A. Pe'er, B. Neyenhuis, J. J. Zirbel, S. Kotochigova, P. S. Julienne, D. S. Jin, and J. Ye. A High Phase-Space-Density Gas of Polar Molecules . *Science*, 322:231–235, 2008.

[77] M. S. Heo, T. T. Wang, C. A. Christensen, T. M. Rvachov, D. A. Cotta, J. H. Choi, Y. R. Lee, and W. Ketterle. Formation of ultracold fermionic NaLi Feshbach molecules. *Phys. Rev. A*, 86:021602(R), 2012.

[78] S. D. Kraft, P. Staanum, J. Lange, L. Vogel, R. Wester, and M. Weidemüller. Formation of ultracold LiCs molecules. *J. Phys. B*, 39:S993–S1000, 2006.

[79] R. Roy, R. Shrestha, A. Green, S. Gupta, M. Li, S. Kotochigova, A. Petrov, and C. H. Yuen. Photoassociative production of ultracold heteronuclear YbLi* molecules. *Phys. Rev. A*, 94:033413, 2016.

[80] J. W. Park, S. A. Will, and M. W. Zwierlein. Ultracold Dipolar Gas of Fermionic ^{23}Na^{40}K Molecules in Their Absolute Ground State. *Phys. Rev. Lett.*, 114:205302, 2015.

[81] A.-C. Voigt, M. Taglieber, T. Aoki, W. Wieser, T. Hänsch, and K. Dieckmann. Ultracold Heteronuclear Fermi-Fermi Molecules. *Phys. Rev. Lett.*, 102:020405, 2009.

[82] F. M. Marchetti, C. J. M. Mathy, and D. A. Huse. Phase separation and collapse in Bose-Fermi mixtures with a Feshbach resonance . *Phys. Rev. B*, 78:134517, 2008.

[83] M. Zaccanti, C. D'Errico, F. Ferlaino, G. Roati, M. Inguscio, and G. Modugno. Control of the interaction in a Fermi-Bose mixture. *Phys. Rev. A*, 74:041605(R), 2006.

[84] K. Sengupta, N. Dupuis, and P. Majumdar. Bose-Fermi mixtures in an optical lattice. *Phys. Rev. A*, 75:063625, 2007.

[85] M. Lewenstein, L. Santos, M. A. Baranov, and H. Fehrmann. Atomic Bose-Fermi Mixtures in an Optical Lattice. *Phys. Rev. Lett.*, 92:050401, 2007.

[86] M. J. Bijlsma, B. A. Heringa, and H. T. C. Stoof. Phonon exchange in dilute Fermi-Bose mixtures: Tailoring the Fermi-Fermi interaction. *Phys. Rev. A*, 61:53601, 2000.

[87] S. De and I. B. Spielman. Fermion-mediated long-range interactions between bosons stored in an optical lattice. *Appl. Phys. B*, 114:527–536, 2014.

[88] D. V. Efremov and L. Viverit. p-wave Cooper pairing of fermions in mixtures of dilute Fermi and Bose gases . *Phys. Rev. B*, 65:134519, 2002.

[89] E. Fratini and P. Pieri. Pairing and condensation in a resonant Bose-Fermi mixture . *Phys. Rev. A*, 81:051605, 2010.

[90] S. Gopalakrishnan, C. V. Parker, and E. Demler. Mobile magnetic impurities in a Fermi superfluid: A route to designer molecules. *Phys. Rev. Lett.*, 114:045301, 2015.

[91] M. Taglieber, A. C. Voigt, T. Aoki, T. W. Hänsch, and K. Dieckmann. Quantum Degenerate Two-Species Fermi-Fermi Mixture Coexisting with a Bose-Einstein Condensate. *Phys. Rev. Lett.*, 100, 2008.

[92] J. W. Park, C.-H. Wu, I. Santiago, T. G. Tiecke, S. Will, P. Ahmadi, and M. W. Zwierlein. Quantum degenerate Bose-Fermi mixture of chemically different atomic species with widely tunable interactions. *Phys. Rev. A*, 85:51602(R), 2012.

[93] V. D. Vaidya, J. Tiamsuphat, S. L. Rolston, and J. V. Porto. Degenerate Bose-Fermi mixtures of rubidium and ytterbium. *Phys. Rev. A*, 92:043604, 2015.

[94] E. Fratini and P. Pieri. Mass imbalance effect in resonant Bose-Fermi mixtures. *Phys. Rev. A*, 85:063618, 2012.

[95] A. Banerjee. Collective oscillations of a Bose-Fermi mixture: Effect of unequal masses of Bose and Fermi particles. *Phys. Rev. A*, 42:235301, 2009.

[96] S. K. Tung, K. Jimenez-Garcia, J. Johansen, C. V. Parker, and C. Chin. Geometric scaling of efimov states in a ^{6}Li-^{133}Cs mixture. *Phys. Rev. Lett.*, 113:240402, 2014.

[97] J. Johansen, B.J. DeSalvo, K. Patel, and C. Chin. Testing universality of Efimov physics across broad and narrow Feshbach resonances. *Nat. Phys.*, 13:731–735, 2017.

[98] J. Ulmanis, S. Häfner, R. Pires, E. D. Kuhnle, M. Weidemüller, and E. Tiemann. Universality of weakly bound dimers and Efimov trimers close to Li–Cs Feshbach resonances. *New J. Phys.*, 17:055009, 2015.

[99] M. Repp, R. Pires, J. Ulmanis, R. Heck, E. D. Kuhnle, M. Weidemüller, and E. Tiemann. Observation of interspecies ^{6}Li-^{133}Cs Feshbach resonances. *Phys. Rev. A*, 87: 010701, 2013.

[100] T. Lee, K. Huang, and C. Yang. Eigenvalues and Eigenfunctions of a Bose system of Hard Spheres and Its Low-Temperature Properties. *Physical Review*, 106:1135–1145, 1957.

[101] I. Ferrier-Barbut, H. Kadau, M. Schmitt, M. Wenzel, and T. Pfau. Observation of Quantum Droplets in a Strongly Dipolar Bose Gas. *Phys. Rev. Lett.*, 116:215301, 2016.

[102] A. Albus, S. A. Gardiner, F. Illuminati, and M. Wilkens. Quantum field theory of dilute homogeneous Bose-Fermi mixtures at zero temperature: General formalism and beyond mean-field corrections . *Phys. Rev. A*, 65:053607, 2002.

[103] E. Braaten and H. W. Hammer. Universality in few-body systems with large scattering length. *Physics Reports*, 428:259–390, 2006.

[104] J. P. D'Incao and B. D. Esry. Mass dependence of ultracold three-body collision rates. *Phys. Rev. A*, 73:030702(R), 2006.

[105] G. Delannoy, S. G. Murdoch, V. Boyer, V. Josse, P. Bouyer, and A. Aspect. Understanding the production of dual Bose-Einstein condensation with sympathetic cooling. *Phys. Rev. A*, 63:051602(R), 2001.

[106] A. Mosk, S. Kraft, M. Mudrich, K. Singer, W. Wohlleben, R. Grimm, and M. Weidemüller. Mixture of ultracold lithium and cesium atoms in an optical dipole trap. *Appl. Phys. B*, 73:791–799, 2001.

[107] H. Yukawa. On the Interaction of Elementary Particles. I. *Proceedings of the Physico-Mathematical Society of Japan. 3rd Series*, 17:48–57, 1935.

[108] H. Yukawa and S. Sakata. On the Interaction of Elementary Particles II. *Proceedings of the Physico-Mathematical Society of Japan. 3rd Series*, 19:1084–1093, 1937.

[109] M. Tinkham. *Introduction to superconductivity.* McGraw-Hill New York, 1975.

[110] M. A. Ruderman and C. Kittel. Indirect Exchange Coupling of Nuclear Magnetic Moments by Conduction Electrons. *Phys. Rev.*, 96:99–102, 1954.

[111] H. P. Büchler and G. Blatter. Supersolid versus Phase Separation in Atomic Bose-Fermi Mixtures. *Phys. Rev. Lett.*, 91:130404, 2003.

[112] M. Lu, N. Q. Burdick, S. H. Youn, and B. L. Lev. Strongly Dipolar Bose-Einstein Condensate of Dysprosium. *Phys. Rev. Lett.*, 107:190401, 2011.

[113] J. B. Balewski, A. T. Krupp, A. Gaj, D. Peter, H. P. Büchler, R. Löw, S. Hofferberth, and T. Pfau. Coupling a single electron to a Bose–Einstein condensate. *Nature*, 502: 664 – 667, 2013.

[114] L. Chomaz, S. Baier, D. Petter, M. J. Mark, F. Wächtler, L. Santos, and F. Ferlaino. Quantum-Fluctuation-Driven Crossover from a Dilute Bose-Einstein Condensate to a Macrodroplet in a Dipolar Quantum Fluid. *Phys. Rev. X*, 6:041039, 2016.

[115] K. R. A. Hazzard, B. Gadway, M. Foss-Feig, B. Yan, S. A. Moses, J. P. Covey, N. Y. Yao, M. D. Lukin, J. Ye, D. S. Jin, and A. M. Rey. Many-Body Dynamics of Dipolar Molecules in an Optical Lattice. *Phys. Rev. Lett.*, 113:195302, 2014.

[116] E. Guardado-Sanchez, P. T. Brown, D. Mitra, T. Devakul, D. A. Huse, P. Schauß, and W. S. Bakr. Probing the Quench Dynamics of Antiferromagnetic Correlations in a 2D Quantum Ising Spin System. *Phys. Rev. X*, 8:021069, 2018.

[117] J. Zeiher, R. van Bijnen, P. Schauß, S. Hild, J.-y. Choi, T. Pohl, I. Bloch, and C. Gross. Many-body interferometry of a Rydberg-dressed spin lattice. *Nat. Phys.*, 12:1095–9, 2016.

[118] D. Suchet, Z. Wu, F. Chevy, and G. M. Bruun. Long-range mediated interactions in a mixed-dimensional system. *Phys. Rev. A*, 95:043643, 2017.

[119] T. Tsurumi and M. Wadati. Dynamics of Magnetically Trapped Boson-Fermion Mixtures. *Journal of the Physical Society of Japan*, 69:97–103, 2000.

[120] S. T. Chui and V. N. Ryzhov. Collapse transition in mixtures of bosons and fermions. *Phys. Rev. A*, 69:043607, 2004.

[121] D. Santamore and E. Timmermans. Fermion-mediated interactions in a dilute Bose-Einstein condensate. *Phys. Rev. A*, 78:013619, 2008.

[122] B. J. DeSalvo, K. Patel, J. Johansen, and C. Chin. Observation of a Degenerate Fermi Gas Trapped by a Bose-Einstein Condensate. *Phys. Rev. Lett.*, 2017.

[123] F. Ferlaino, R. J. Brecha, P. Hannaford, F. Riboli, G. Roati, G. Modugno, and M. Inguscio. Dipolar oscillations in a quantum degenerate Fermi - Bose atomic mixture. *J. Opt. B: Quantum Semiclass. Opt.*, 5:S3, 2003.

[124] I. Ferrier-Barbut, M. Delehaye, S. Laurent, A. T. Grier, M. Pierce, B. S. Rem, F. Chevy, and C. Salomon. A mixture of Bose and Fermi superfluids. *Science*, 345:1035–1038, 2014.

[125] S. D. Gensemer and D. S. Jin. Transition from collisionless to hydrodynamic behavior in an ultracold fermi gas. *Phys. Rev. Lett.*, 87, 2001.

[126] G. Ferrari, M. Inguscio, W. Jastrzebski, G. Modugno, and G. Roati. Collisional Properties of Ultracold K-Rb Mixtures. *Phys. Rev. Lett.*, 89:053202, 2002.

[127] W. E. Lamb and R. C. Retherford. Fine Structure of the Hydrogen Atom by a Microwave Method . *Phys. Rev.*, 72:241, 1947.

[128] J. Schwinger. On Quantum-Electrodynamics and the Magnetic Moment of the Electron. *Phys. Rev.*, 73:416–417, 1948.

[129] J. Bardeen, L. N. Cooper, and J. R. Schrieffer. Microscopic Theory of Superconductivity. *Phys. Rev.*, 106:162–164, 1957.

[130] G. Giustino. Electron-phonon interactions from first principles . *Rev. Mod. Phys.*, 89, 2017.

[131] B. Keimer, S. A. Kivelson, M. R. Norman, S. Uchida, and J. Zaanen. From quantum matter to high-temperature superconductivity in copper oxides. *Nature*, 518:179–186, 2015.

[132] Z. Yan, Y. Ni, C. Robens, and M. W. Zwierlen. Bose polarons near quantum criticality. *Science*, 368:190–104, 2020.

[133] M. Delehaye, S. Laurent, I. Ferrier-Barbut, S. Jin, F. Chevy, and C. Salomon. Critical Velocity and Dissipation of an Ultracold Bose-Fermi Counterflow. *Phys. Rev. Lett.*, 115:265303, 2015.

[134] E. Pazy and A. Vardi. Holstein model and Peierls instability in one-dimensional boson-fermion lattice gases. *Phys. Rev. A*, 72:033609, 2005.

[135] D. Banerjee, M. Dalmonte, M. Müller, E. Rico, P. Stebler, U.-J. Wiese, and P. Zoller. Atomic Quantum Simulation of Dynamical Gauge Fields Coupled to Fermionic Matter: From String Breaking to Evolution after a Quench . *Phys. Rev. Lett.*, 109:175302, 2012.

[136] T. Enss and W. Zwerger. Superfluidity near phase separation in Bose-Fermi mixtures. *Eur. Phys. J. B*, 68:383–389, 2009.

[137] See Section 6.5.

[138] H. Edri, B. Raz, N. Matzliah, N. Davidson, and R. Ozeri. Observation of Spin-Spin Fermion-Mediated Interactions between Ultracold Bosons. *Phys. Rev. Lett.*, 124: 163401, 2020.

[139] R. Meppelink, S.B.Koller, and P. van der Straten. Sound propagation in a Bose-Einstein condensate at finite temperatures. *Phys. Rev. A*, 80:043605, 2009.

[140] M. R. Andrews, D. M. Kurn, H.-J. Miesner, D. S. Durfee, C. G. Townsend, S. Inouye, and W. Ketterle. Propagation of Sound in a Bose-Einstein Condensate. *Phys. Rev. Lett.*, 79:553, 1997.

[141] J. Joseph, B. Clancy, L. Luo, J. Kinast, A. Turlapov, and J. E. Thomas. Measurement of Sound Velocity in a Fermi Gas near a Feshbach Resonance. *Phys. Rev. Lett.*, 98: 170401, 2007.

[142] G. Kavoulakis and C. J. Pethick. Quasi-one-dimensional character of sound propagation in elongated Bose-Einstein condensed clouds. *Phys. Rev. A*, 58:1563, 1998.

[143] A. Belemuk, V. Rhyzov, and S.-T. Chui. Stable and unstable regimes in Bose-Fermi mixtures with attraction between components. *Phys. Rev. A*, 76:013609, 2007.

[144] T. Enss, B. Tran, M. Rautenberg, M. Gerken, E. Lippi, M. Drescher, B. Zhu, M. Weidemüller, and M. Salmhofer. Scattering of two heavy Fermi polarons: Resonances and quasibound states. *Phys. Rev. A*, 102, 2020.

[145] D. Rakshit, T. Karpiuk, M. Brewcyzk, and M. Gajda. Quantum Bose-Fermi droplets. *SciPost Phys.*, 6:079, 2019.

[146] J. Kinnunen, Z. Wu, and G. M. Bruun. Induced p-Wave Pairing in Bose-Fermi Mixtures. *Phys. Rev. Lett.*, 121:253402, 2018.

[147] S. Tung, C. Parker, J. Johansen, C. Chin, Y. Wang, and P. S. Julienne. Ultracold mixtures of atomic ^{6}Li and ^{133}Cs with tunable interactions. *Phys. Rev. A*, 87:010702(R), 2013.

[148] T. Karpiuk, M. Gajda, and M. Brewczyk. Bistability of Bose–Fermi mixtures. *New J. Phys*, 22:103025, 2020.

[149] D. A. Kirznits. Quantum corrections to the Thomas-Fermi equation. *Sov. Phys. JETP*, 5:64, 1957.

[150] K. Gawryluk, T. Karpiuk, M. Gajda, K. Rzążewski, and M. Brewczyk. Unified way for computing dynamics of Bose–Einstein condensates and degenerate Fermi gases . *Int. J. Comput. Math.*, 95:11:2143–2161, 2018.

[151] B. Huang. Bose-Einstein condensate immersed in a Fermi sea: Theory of static and dynamic behavior across phase separation. *Phys. Rev. A*, 101:063618, 2020.

[152] J. Stenger, S. Inouye, A. P. Chikkatur, D. M. Stamper-Kurn, D. E. Pritchard, and W. Ketterle. Bragg Spectroscopy of a Bose-Einstein Condensate. *Phys. Rev. Lett.*, 82, 1999.

[153] K. Riechers, K. Hueck, N. Luick, T. Lompe, and H. Moritz. Detecting Friedel oscillations in ultracold Fermi gases. *Eur. Phys. J. D*, 71, 2017.

[154] M. Sun, H. Zhai, and X. Cui. Visualizing the Efimov Correlation in Bose Polarons. *Physical Review Letters*, 119, 7 2017.

[155] Y. Nishida. Casimir interaction among heavy fermions in the BCS-BEC crossover . *Phys. Rev. A*, 79:013629, 2009.

[156] M. Sun and X. Cui. Efimov physics in the presence of a Fermi sea. *Phys. Rev. A*, 99, 2019.

[157] K. Suzuki, T. Miyakawa, and T. Suzuki. p-wave superfluid and phase separation in atomic Bose-Fermi mixtures. *Phys. Rev. A*, 77:043629, 2008.

[158] H. Heiselberg, C. J. Pethick, H. Smith, and L. Viverit. Influence of Induced Interactions on the Superfluid Transition in Dilute Fermi Gases. *Phys. Rev. Lett.*, 85:2418, 2000.

[159] L. Salasnich and F. Toigo. Fermi-Bose mixture across a Feshbach resonance. *Phys. Rev. A*, 75:013623, 2007.

[160] K. Maeda, G. Baym, and T. Hatsuda. Simulating dense QCD matter with ultracold atomic boson-fermion mixtures. *Phys. Rev. Lett.*, 103, 2009.

[161] T. Ozawa, A. Recati, M. Delehaye, F. Chevy, and S. Stringari. Chandrasekhar-Clogston limit and critical polarization in a Fermi-Bose superfluid mixture. *Phys. Rev. A*, 90:043608, 2014.

[162] B. Ramachandhran, S. G. Bhongale, and H. Pu. Finite-temperature study of Bose-Fermi superfluid mixtures. *Phys. Rev. A*, 83:033607, 2011.

[163] K. Y. Jee and E. Mueller. Drag in Bose-Fermi Mixtuers. *Phys. Rev. A*, 103:033307, 2021.